Study of the properties of the $D_{sJ}(2317)$ and $D_{sJ}(2460)$ mesons at *BABAR*

Thesis submitted in accordance with the requirements of the University of Liverpool for the degree of Doctor in Philosophy

by

Ian Stephen Bingham

October 2009

UNIVERSITY OF
LIVERPOOL

Abstract

An investigation into $B \to D_{sJ}^{+} D^{(*)}$ decays and a study of the properties of the $D_{sJ}^{+}(2317)$ and $D_{sJ}^{+}(2460)$ mesons are presented. The analysis uses a data sample with integrated luminosity of 390.82 fb^{-1}, corresponding to 382.9 million $B\overline{B}$ pairs, produced in the *BABAR* detector at the PEP-II asymmetric B factory.

The dataset is used to measure branching fractions for the $B \to D_{sJ}^{+} D^{(*)}$ decays. To determine the spin of the $D_{sJ}^{+}(2317)$ and $D_{sJ}^{+}(2460)$ mesons, an angular analysis is performed for each of the three decays:

- $D_{sJ}^{+}(2317) \to D_{s}^{+}\pi^{0}$
- $D_{sJ}^{+}(2460) \to D_{s}^{+}\gamma$
- $D_{sJ}^{+}(2460) \to D_{s}^{*+}\pi^{0}$

Acknowledgements

This thesis has only been made possible through the efforts and support of many others and I would like to thank all of those who have provided assistance along the way.

Firstly I would like to thank my supervisor Christos Touramanis for providing help and guidance throughout. I'm especially grateful to Carlos for his assistance on all aspects of the work during this period. A big thank you to Dave and Jon as well for their advise and expertise.

My colleagues at Liverpool have always kept me amused and entertained and so a big thank you to Lisa, Mike, Nick, Paul, A.J, Abdi, Craig and Steph.

I would like to thank the University of Liverpool and especially the high energy physics group for giving me the opportunity to conduct this research. Also thanks go to STFC for funding me whilst I have completed this work.

Thank you to the *BABAR* collaboration and everyone working at SLAC for being an excellent host and providing me with the chance to carry out this study.

I'm eternally grateful to my parents without whose support and foundation I wouldn't have achieved what I have. I'm also indebted to Mark for his selfless attitude and inspiration. Thanks also go to my Grandparents for their kindness and warmth over the years.

I would finally like to give special thanks to Charlotte for sharing this journey alongside me and for providing unquestioning support throughout.

Contents

List of Figures

List of Tables

Chapter 1

Introduction

The accepted explanation of how the universe came into existence is the Big Bang theory. In it, there is a description of how matter and antimatter were created in equal amounts and how they would have annihilated later creating radiation. However, in the Universe today all antimatter has been annihilated yet there is still matter. The only way of explaining this is that there is a small matter-antimatter asymmetry that is responsible for the universe we live in today.

The Standard Model (SM) is a description of the fundamental particles that make up the matter (and antimatter) and the interactions between them. In the Standard model all matter is thought to consist of various combinations of 12 elementary spin 1/2 fermions (6 quarks and 6 leptons). Fundamental interactions

are explained by the exchange of spin 1 bosons whilst a further spin 0 Higgs boson accounts for the mass of particles. The Standard Model is a very successful model but it is also incomplete in that it doesn't include gravitation interactions and is unable to address some fundamental questions. One of the central themes of high energy physics is to test the Standard Model and discover any physics beyond it.

CP violation is one of the three conditions identified by Sakharov [1] that must be satisfied in order for the universe to evolve into a system with unequal amounts of matter and antimatter. CP violation is allowed in the Standard Model but the amount predicted is too small by several orders of magnitude to account for the matter-antimatter asymmetry in our universe. Probing this effect experimentally is one of the main goals of the *BABAR* experiment at the SLAC Linear Accelerator Laboratory (SLAC).

Experimentalists and Theorists were set into a flurry of activity in 2003 by the unexpected discovery of two narrow meson states of mass 2.317 GeV/c^2 and 2.460 GeV/c^2 at *BABAR* and CLEO respectively [20, 21]. Whilst similar states were predicted by theory the masses of the discovered states were lower than predicted and it was expected that they would be hard to detect experimentally. In order to account for these lower masses, new theories were proposed, which suggest the need for a better understanding of their quantum numbers. The study of the properties of these mesons ($D_{sJ}^{+}(2317)$ and $D_{sJ}^{+}(2460)$) is the main aim of

the analysis contained within this thesis.

Chapter 2 gives an introduction into the theory behind the Standard Model, CP violation and D meson spectroscopy. The experimental conditions and physics requirements of the *BABAR* experiment are discussed in Chapter 3. Chapter 4 describes how data provided by the detector is processed as well as the tests that are involved to check on its quality. The analysis methods such as event selection and validation are explained in Chapter 5. Chapter 6 provides the results from the analysis and Chapter 7 finishes up by outlining any conclusions that can be drawn.

Chapter 2

Theory

2.1 Introduction

The aim of this chapter is to provide an overview of the theoretical background behind the physics topics contained within this thesis. To aid this discussion it is important to present the wider picture of particle physics and give a summary of the standard model. In discussing the standard model a brief background of the fundamental particles and their interactions is given along with an introduction to the symmetries involved. One of the main goals of the *BABAR* experiment is the study of CP violation and this chapter introduces that concept and describes the experimental methods for examining it. The analysis undertaken in this thesis is

related to spectroscopy which is discussed along with the theory behind it and an introduction to the particular mesons involved.

2.2 The Standard Model

The Standard Model (SM) is a theory of fundamental particles and the electromagnetic, weak and strong forces that act upon them. Together with general relativity, with governs gravity, it provides a description of the four known fundamental forces. This section provides a brief summary of the description of fundamental particles, interactions and symmetries contained within it.

2.2.1 The Fundamental Particles

In the standard model, all matter in the universe is made up of a number of different particle types with associated physical properties, such as mass, and defined by a set of parameters known as quantum numbers. These quantum numbers determine in which way particles interact with each other and therefore categories are defined in which the particles are organised.

Particles are denoted as fermions or bosons, by virtue of their "spin" quantum number (s), where bosons are defined as particles with integer spin and fermions

are defined as having half integer spin. The fundamental, *gauge*, bosons have spin $s = 1$ and act as force carriers for the different particle interactions. The electromagnetic (EM) force is mediated by massless photons, the weak force by massive W and Z bosons and the strong force by massless gluons. Table 2.1 shows a summary of the gauge bosons and their relative strengths at around 1 GeV.

Force	Bosons	M (MeV/c^2)	Strength
Electromagnetic	Photon (γ)	0	10^{-2}
Weak	$W^{\pm}$	80.398	10^{-7}
	Z^0	91.188	
Strong	Gluon (g)	0	1

Table 2.1: *The properties of the four gauge bosons*

The fundamental fermions are divided further into quarks (q), which are acted upon by the strong force, and leptons, which aren't. The leptons comprise three "generations" of charged particles ($e^-\mu^-\tau^-$) and each is associated with a corresponding neutral, light particle, called the neutrino (ν_e, ν_μ, ν_τ). Table 2.2 shows a summary of the leptons.

Particle	Symbol	M (MeV/c^2)	Charge (Q)	Force
Electron	e^-	0.511	-1	Weak, EM
Electron Neutrino	ν_e	$< 2 \times 10^{-6}$	0	Weak
Muon	μ^-	105.7	-1	Weak, EM
Muon Neutrino	ν_μ	< 0.19	0	Weak
Tau	τ^-	1.777×10^3	-1	Weak, EM
Tau Neutrino	ν_τ	< 18.2	0	Weak

Table 2.2: *The properties of the six leptons*

The quarks come in six "flavours" (up, down, charm, strange, top, bottom) which can also be arranged in three "generations" containing an up-type quark (of charge $Q = 2/3$) and a down-type quark (of charge $Q = -1/3$). Table 2.3 shows a summary of the quarks. Unlike the other fundamental particles, quarks are never observed on their own, but rather as part of a multi-quark bound state, known as a hadron. At present the only bound states observed have been baryons which are formed from three quarks (qqq) and mesons which are formed from a quark-antiquark pair ($q\overline{q}$) although others (such as pentaquarks) may exist. The confinement of quarks into bound states is due to the strong force and is described by quantum chromodynamics (QCD). Bound states, specifically mesons, will be discussed in more detail in Section 2.4.1.

Particle	Symbol	M (MeV/c^2)	Charge (Q)	Force
up	u	1.5 - 3.3	2/3	Strong, Weak, EM
down	d	3.5 - 6.0	-1/3	Strong, Weak, EM
charm	c	1.27 $\times 10^3$	2/3	Strong, Weak, EM
strange	s	70.0 - 130.0	-1/3	Strong, Weak, EM
top	t	1.71 $\times 10^5$	2/3	Strong, Weak, EM
bottom	b	4.2 $\times 10^3$	-1/3	Strong, Weak, EM

Table 2.3: *The properties of the six quarks*

As well as those mentioned above, there are also what's known as anti-particles (such as an anti-quark referred to above). Each type of particle is associated with a "mirror image" partner with the same mass, but which has quantum numbers (such as lepton number or charge) with a reversed sign. An example is

the positron (e^+) which is the anti-particle partner of the electron (e^-). If their is an ambiguity with regards to notation, antiparticles are denoted with a bar over them ($\overline{u}$, $\overline{\nu}_e$).

2.2.2 Particle Interactions

Excluding gravity, which is negligible in fundamental particle interactions, there are three forces which act upon the particles above, the electromagnetic force, the weak force and the strong force. In each case the interaction between particles takes the form of a boson exchange, with the boson in question depending on the force (as per Table 2.1).

The Electromagnetic Force

The electromagnetic interaction is described by Quantum Electrodynamics (QED) and acts on all charged particles through the propagation of photons. Formally, QED is derived through the requirement of U(1) gauge symmetry which means that the Lagrangian must be unaltered when the charged particle waveform undergoes the transformation:

$$\psi(x) \rightarrow e^{i\alpha(x)}\psi(x) \tag{2.1}$$

where $\alpha(x)$ is a real constant with spatial dependence. This can only be achieved by introducing a photon field to the free particle Lagrangian.

The Weak Force

The weak force acts on all quarks and leptons through the transfer of charged ($W^{\pm}$) and neutral bosons (Z^0). The weak interaction is the only method by which neutrinos interact in particle reactions and is also the only interaction that allows flavour changing processes (as will be discussed in Section 2.3). The "charge" of the weak interaction is called *weak isospin* (T) and its component along the quantised access, T_3. Left handed fermions have T = 1/2, forming doublets in the quark and lepton sectors, whilst right handed fermions have T = 0. The appropriate representation for the weak interaction is $SU(2)_L$ where the L refers to the fact that the interactions of right-handed massive fermions are suppressed.

The electromagnetic and weak forces are seen to be unified into a single electroweak interaction, as formulated by the Glashow-Weinberg-Salam (GWS) Model [2, 3, 4], and form an $SU(2)_L \times U(1)_Y$ symmetry. The $U(1)_Y$ group is associated with a *weak hypercharge* $Y = 2(Q - T_3)$ and means that right handed fermions can participate in weak interactions as long as they are charged.

The Strong Force

The strong interactions are described by Quantum Chromodynamics (QCD) and act, through the exchange of gluons, on all colour-charged particles. Colour is the "charge" of the strong force and comes in three varieties, Red (R), Green (G) and Blue (B). One difference of the strong force is that the propagator, gluons, carry the colour charge and can therefore self-interact. One consequence of QCD is quark confinement which leads to the fact that quarks can only be found in colourless bound states. The strong force is characterised by the $SU_C(3)$ phase transformation group where the C refers to the colour charge. The interactions in the standard model are therefore described by the $SU_C(3) \times SU(2)_L \times U(1)_Y$ gauge group.

2.2.3 Symmetries and Composite Particles

When a particle decays, it is subject to a number of conservation laws which determine in which way it is allowed to decay and it is necessary to introduce some symmetry principles in order to be able to describe this behavior fully. Examples of properties that must be conserved are Electric Charge, Lepton and Baryon Number, Energy and Momentum. Another conserved quantity of interest is the total quantized angular momentum, $\overrightarrow{J}$. This quantity is formed by the

vector addition of the total spin $\vec{S}$ and the orbital angular momentum $\vec{L}$. In addition to those mentioned above, there are three conserved quantities that are of specific relevance to the *BABAR* experiment and these are described below.

Charge Conjugation

Charge conjugation is a discrete symmetry and its transformation is a replacement of all particles by their corresponding antiparticles and vice versa. Under this transformation, **C**, kinematic variables (mass, energy, etc) stay the same but all internal quantum numbers change sign. Since two successive transformations take the state back to its initial form, the only allowable effect of a single transformation **C** is to produce a multiplication factor of ± 1 to the wavefunction. This means the associated eigenvalue, C, can only take the values ± 1. Charge conjugation symmetry states that physical processes should be invariant under this transformation and this is true for both the strong and electro-magnetic forces. The weak force however violates this symmetry as charge conjugation transforms left handed neutrinos into left handed antineutrinos. For mesons C is given by:

$$C = (-1)^{L+S} \tag{2.2}$$

Parity

The Parity transformation **P** changes the sign of all the spatial co-ordinates (x, y, z) of the wavefunction. Like charge conjugation, the associated eigenvalue P can only take the value ± 1 although the parity is often denoted as being + (even) or - (odd). Fundamental particles have an intrinsic parity, with each fermion having opposite parity to its anti-fermion. For composite particles, the parity is equal to the multiplication of the parities of the constituent particles. The interaction of the particles also gives an additional contribution. For mesons P is given by:

$$P = (-1)^{L+1} \tag{2.3}$$

As with charge conjugation, parity is associated with a symmetry and physics processes should be invariant under the parity transformation. This is true for both strong and electro-magnetic forces however the weak force violates this symmetry and the absence of right handed neutrino interactions is clear evidence for parity non-conservation.

Isospin

Isospin is another symmetry and was initially introduced in order to express protons and neutrons as a single particle called a nucleon. Isospin reflects the fact that up and down quarks have nearly identical masses and the proton and neutrons were said to be nucleons that differ by way of an additional spin-like quality. The nucleon was given spin I= $\frac{1}{2}$ with protons having a projection along an axis $I_3 = +\frac{1}{2}$ and neutrons having $I_3 = -\frac{1}{2}$. Pions were also included in this description and form an isospin singlet:

$$\frac{1}{\sqrt{2}}(u\overline{u} + d\overline{d}) \quad (I = 0, I_3 = 0)$$

and isospin triplet:

$$\pi^+ = u\overline{d} \qquad (I = 1, I_3 = 1)$$

$$\pi^0 = \frac{1}{\sqrt{2}}(u\overline{u} - d\overline{d}) \qquad (I = 1, I_3 = 0)$$

$$\pi^- = d\overline{u} \qquad (I = 1, I_3 = -1)$$

Strong Decays preferentially conserve isospin where the non-zero mass difference between the up and down quarks causes a deviation from a true symmetry. As a result, decays are suppressed in which I_3 is not conserved.

2.3 CP violation

In Section 2.2.3 the charge conjugation and parity transformations were defined and said to be violated in weak decays. Parity Violation was first proposed by Lee and Yang in 1956 [5] and was shown experimentally by Wu *et al.* in 1957 [6]. Also in 1957 Ioffe *et al.* showed that parity violation meant that charge conjugation invariance must also be violated in weak decays [7]. It was thought however that the combined **CP** symmetry would be respected by weak decays. In 1964 Christenson *et al.* discovered that in certain kaon decays this combined CP symmetry was also violated [8]. Investigating CP violation is one of the main physics goals of the *BABAR* experiment and this section introduces CP violation and the CKM description of flavour changing processes.

2.3.1 CP violation in the Standard Model

A property unique to the weak interaction is that it can change flavour. The mechanism that allows this in quarks is called *quark mixing* and was introduced by Cabibbo in 1963 [9]. Cabibbo suggested that the weak eigenstate d' consists of the linear superposition of the flavour eigenstates d and s. For the two quark system this can be written as:

$$\begin{pmatrix} d' \\ s' \end{pmatrix} = \begin{pmatrix} cos\theta_C & sin\theta_C \\ -sin\theta_C & cos\theta_C \end{pmatrix} \begin{pmatrix} d \\ s \end{pmatrix} \tag{2.4}$$

The matrix in equation 2.4 is written using a single Cabibbo angle θ_C which is measured experimentally to be 12.3° [10]. In 1973 Kobayashi and Maskawa proposed a third generation of quarks and leptons [11] with the 2 × 2 Cabibbo matrix becoming the 3 × 3 CKM matrix, $\mathbf{V}_{CKM}$. In order to parameterise this three quark matrix there is required to be three real angles and one complex phase, with the complex phase being the sole source of CP violation in the Standard Model. Shortly afterwards there was experimental evidence for third generation fermions such as the b quark [12] and the τ lepton [13]. With a third generation of quarks the equation 2.4 becomes:

$$\begin{pmatrix} d' \\ s' \\ b' \end{pmatrix} = \mathbf{V}_{CKM} \begin{pmatrix} d \\ s \\ b \end{pmatrix} = \begin{pmatrix} V_{ud} & V_{us} & V_{ub} \\ V_{cd} & V_{cs} & V_{cb} \\ V_{td} & V_{ts} & V_{tb} \end{pmatrix} \begin{pmatrix} d \\ s \\ b \end{pmatrix} \tag{2.5}$$

where each $\mathbf{V}_{CKM}$ matrix element V_{ij} is the weak coupling between quarks i and j. The standard parameterisation of the CKM matrix is shown below:

$$\mathbf{V}_{CKM} = \begin{pmatrix} c_{12}c_{13} & s_{12}c_{13} & s_{13}e^{-i\delta} \\ -s_{12}c_{23} - c_{12}s_{23}s_{13}e^{i\delta} & c_{12}c_{23} - s_{12}s_{23}s_{13}e^{i\delta} & s_{23}c_{13} \\ s_{12}s_{23} - c_{12}c_{23}s_{13}e^{i\delta} & -c_{12}s_{23} - s_{12}c_{23}s_{13}e^{i\delta} & c_{23}c_{13} \end{pmatrix} \tag{2.6}$$

where $s_{ij} = sin\theta_{ij}$, $c_{ij} = cos\theta_{ij}$, θ_{ij} represents the mixing angle and δ represents the phase. Experimental results show a hierarchy in the magnitudes of the matrix elements: $|V_{ii}| \approx 1$, $|V_{12}| \approx |V_{21}| \approx \lambda$, $|V_{23}| \approx |V_{32}| \approx \lambda^2$ and $|V_{13}| \approx |V_{31}| \approx \lambda^3$, where $\lambda = s_{12} \approx 0.22$ is the sine of the Cabibbo angle. Hence it is possible to make an alternative approximate parameterisation, as first suggested by Wolfenstein [14]:

$$\mathbf{V}_{CKM} \approx \begin{pmatrix} 1 - \frac{\lambda^2}{2} & \lambda & A\lambda^3(\rho - i\eta) \\ -\lambda & 1 - \frac{\lambda^2}{2} & A\lambda^2 \\ A\lambda^3(1 - \rho - i\eta) & -A\lambda^2 & 1 \end{pmatrix} + \mathcal{O}(\lambda^4) \tag{2.7}$$

To conserve the number of quarks and be self-contained the CKM matrix must be unitary. This can be expressed by:

$$\mathbf{V}_{CKM}^{\dagger}\mathbf{V}_{CKM} = \mathbf{I} = \mathbf{V}_{CKM}\mathbf{V}_{CKM}^{\dagger} \tag{2.8}$$

There are two relevant types of relation that arise from this:

$$\sum_j |V_{ij}|^2 = 1, \quad \text{and} \tag{2.9}$$

$$\sum_i V_{id}V_{is}^* = 0, \quad \sum_i V_{is}V_{ib}^* = 0, \quad \sum_i V_{id}V_{ib}^* = 0$$

$$\sum_j V_{uj}V_{cj}^* = 0, \quad \sum_j V_{cj}V_{tj}^* = 0, \quad \sum_j V_{uj}V_{tj}^* = 0 \tag{2.10}$$

where $i = u,c,t$ and $j = d,s,b$. Equation 2.9 describes *weak universality* implying that the sum of all the couplings of any up-type quark to the down-type quark is independent of the generation considered. Of the relations in Equation 2.10, the one of specific interest is:

$$V_{ud}V_{ub}^* + V_{cd}V_{cb}^* + V_{td}V_{tb}^* = 0 \tag{2.11}$$

This equation can be depicted as a triangle, called the *Unitarity Triangle*, on the complex plane and is illustrated in Figure 2.1. A Phase convention is chosen such that $V_{cd}V_{cb}^*$ is real and the terms have been normalised by $|V_{cd}||V_{cb}^*|$. This convention ensures that two of the corners lie at (0,0) and (1,0) thus leaving only the apex to find $(\overline{\rho}, \overline{\eta})$ where:

$$\overline{\rho} = \rho(1 - \lambda^2/2), \quad \overline{\eta} = \eta(1 - \lambda^2/2) \tag{2.12}$$

where λ, ρ and η are the quantities used in the Wolfenstein parameterisation shown in Equation 2.7. The three internal angles of the triangle are given by:

$$\alpha \equiv arg\left[-\frac{V_{td}V_{tb}^*}{V_{ud}V_{ub}^*}\right], \quad \beta \equiv arg\left[-\frac{V_{cd}V_{cb}^*}{V_{td}V_{tb}^*}\right], \quad \gamma \equiv arg\left[-\frac{V_{ud}V_{ub}^*}{V_{cd}V_{cb}^*}\right] \tag{2.13}$$

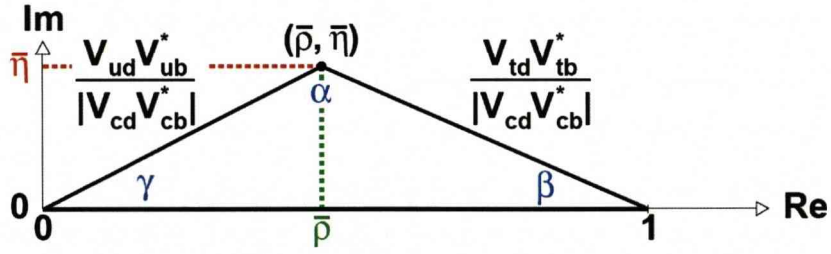

Figure 2.1: *The unitarity triangle (not to scale)*

By measuring the sides and angles of the Unitarity Triangle, in as many independent ways as possible, it is possible to test CP violation in the Standard Model. There is also a model independent measure of the amount of CP violation in the Standard Model, called the Jarlskog invariant [15], which is given by the equation below:

$$J = c_{12}c_{23}c_{13}^2 s_{12}s_{23}s_{13}sin\delta \approx A^2\eta\lambda^6 \tag{2.14}$$

2.3.2 Mixing of Neutral Mesons

The box diagrams in Figure 2.2 demonstrate mixing in the standard model in which particle and antiparticle states can oscillate. This is not permitted in most particle-antiparticle systems as various quantum numbers must be conserved independently of whether it is a strong, electromagnetic or weak interaction. For a few systems however, such as the neutral K, D and B systems, there are no such quantum numbers to conserve when taking the weak interaction into account. In these situations the observed physical properties do not correspond to the flavour eigenstates ($|P^0\rangle$ and $|\overline{P}^0\rangle$), with particular quark content, but to linear combinations of these.

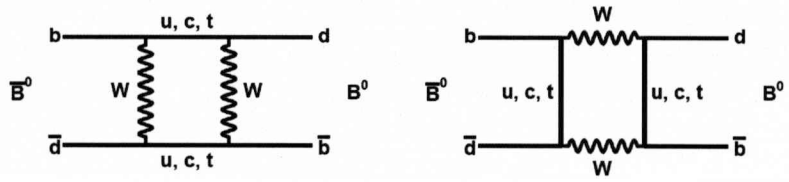

Figure 2.2: *Feynman Diagrams showing the second order weak interactions that give rise to $B^0 - \overline{B}^0$ mixing*

We can consider the time evolution of an arbitrary state consisting of a linear superposition of the flavour eigenstates:

$$|P(t)\rangle = a(t)|P^0\rangle + b(t)|\overline{P}^0\rangle \tag{2.15}$$

which is determined by the time dependent Schrödinger equation (TDSE):

$$i\frac{\partial}{\partial t}\begin{pmatrix} a(t) \\ b(t) \end{pmatrix} = \mathbf{H}\begin{pmatrix} a(t) \\ b(t) \end{pmatrix} = \begin{pmatrix} H_{11} & H_{12} \\ H_{21} & H_{22} \end{pmatrix}\begin{pmatrix} a(t) \\ b(t) \end{pmatrix} = (\mathbf{M}-\frac{i}{2}\Gamma)\begin{pmatrix} a(t) \\ b(t) \end{pmatrix} \tag{2.16}$$

where $\mathbf{H}$ is the Hamiltonian matrix, and $\mathbf{M}$ and Γ are 2×2 Hermitian matrixes describing the mixing and decay respectively.

Invariance under the **CPT** transformation (a prerequisite of quantum field theory and assumed to be true), where $\mathbf{T}$ is the time reversal operator, requires that H_{11} and H_{22} are equal. The off-diagonal elements H_{12} and H_{21} are the amplitudes for mixing and if these elements are zero then no mixing occurs.

Mixing without CP Violation

For CP symmetry to hold we require that $H_{12}^* = H_{21}$. With no CP violation Equation 2.16 becomes:

$$i\frac{\partial}{\partial t}\begin{pmatrix} a(t) \\ b(t) \end{pmatrix} = \begin{pmatrix} A & B \\ B^* & A \end{pmatrix}\begin{pmatrix} a(t) \\ b(t) \end{pmatrix} = \begin{pmatrix} M_{11} - \frac{i}{2}\Gamma_{11} & M_{12} - \frac{i}{2}\Gamma_{12} \\ (M_{12} - \frac{i}{2}\Gamma_{12})^* & M_{22} - \frac{i}{2}\Gamma_{22} \end{pmatrix}\begin{pmatrix} a(t) \\ b(t) \end{pmatrix} \tag{2.17}$$

By diagonalising $\mathbf{H}$ we can move into the mass basis. $\mathbf{X}$ is defined to be the matrix whose columns contain the eigenvectors of $\mathbf{H}$ such that:

$$\mathbf{H} = \mathbf{X}\begin{pmatrix} A + |B| & 0 \\ 0 & A - |B| \end{pmatrix}\mathbf{X}^{-1} \tag{2.18}$$

where $A + |B|$ and $A - |B|$ are eigenvalues of $\mathbf{H}$. The resulting mass eigenstates are given by:

$$|P_{1,2}\rangle = \frac{1}{\sqrt{2}}(|P^0\rangle \pm |\overline{P}^0\rangle) \tag{2.19}$$

The masses and widths of the mass eigenstates are given by the real and imaginary parts of the eigenvalues respectively:

$$M_{1,2} = \Re(A \pm |B|), \quad -\frac{\Gamma_{1,2}}{2} = \Im(A \pm |B|) \tag{2.20}$$

If CP invariance is exact then the mass eigenstates are also CP eigenstates which have eigenvalues of ± 1:

$$\mathbf{CP}|P_1\rangle = (+1)|P_1\rangle, \quad \mathbf{CP}|P_2\rangle = (-1)|P_1\rangle \tag{2.21}$$

Mixing with CP Violation

If CP invariance is not assumed to be exact the off-diagonal elements of **H** are not required to be of equal magnitude and **H** can now be expressed as:

$$\mathbf{H} = \begin{pmatrix} A & B/r \\ rB^* & A \end{pmatrix} \tag{2.22}$$

The mass eigenstates are now:

$$|P'_{1,2}\rangle = \frac{1}{\sqrt{1+|r|^2}}(|P^0\rangle \pm r|\overline{P}^0\rangle) \tag{2.23}$$

The masses and widths of the two states derive from the real and imaginary parts of $A \pm |B|$ and the mass eigenstates are no longer CP eigenstates.

Mixing in the B ^{0} System

The neutral B meson mass eigenstates, $|B_L\rangle$ and $|B_H\rangle$ can be written as linear superpositions of the flavour eigenstates $|B^0\rangle$ and $|\overline{B}^0\rangle$ as shown below:

$$\begin{aligned} |B_L\rangle &= p|B^0\rangle + q|\overline{B}^0\rangle \\ |B_H\rangle &= p|B^0\rangle - q|\overline{B}^0\rangle \end{aligned} \tag{2.24}$$

where p and q are complex coefficients (to allow for a phase difference between the two states) that satisfy the normalisation condition:

$$|p|^2 + |q|^2 = 1 \tag{2.25}$$

The mass, M, mass difference, Δm_B, and lifetime difference, $\Delta\Gamma_B$ are defined as:

$$\begin{aligned} M &= \frac{1}{2}(M_H + M_L) \\ \Delta m_B &= M_H - M_L \\ \Delta\Gamma_B &= \Gamma_H - \Gamma_L \end{aligned} \tag{2.26}$$

where $M_{H,L}$ and $\Gamma_{H,L}$ are the quantities defined in Equation 2.20. It has been shown experimentally [16] that:

$$\Delta m_B \gg \Delta\Gamma_B \tag{2.27}$$

A general B state $|\psi(t)\rangle$ propagating through space is a superposition of the mass eigenstates and evolves with time according to the following:

$$|\psi(t)\rangle = a_L(t)|B_L\rangle + a_H(t)|B_H\rangle \tag{2.28}$$

where the amplitudes $a_L(t)$ and $a_H(t)$ are time dependent and solutions of the TDSE as given by:

$$a_L(t) = a_L(0)e^{-iM_L t}e^{-\frac{1}{2}\Gamma_L t}$$
$$a_H(t) = a_H(0)e^{-iM_H t}e^{-\frac{1}{2}\Gamma_H t} \tag{2.29}$$

Using equations 2.24, 2.28 and 2.29 it can be seen that for a pure $|B^0\rangle$ state at time t = 0 the following condition must follow:

$$a_L(0) = a_H(0) = \frac{1}{2p} \tag{2.30}$$

and similarly for a pure $|\overline{B}^0\rangle$ at time t=0:

$$a_L(0) = -a_H(0) = \frac{1}{2q} \tag{2.31}$$

Substituting Equations 2.24 and 2.29 into Equation 2.28 and using Equations 2.26, 2.30 and 2.31, we are now able to show how a state that is initially pure $|B^0\rangle$ evolves to become pure $|\overline{B}^0\rangle$ and oscillates between the two states (using $\Gamma_L = \Gamma_H = \Gamma$ as implied by Equation 2.27):

$$|B^0(t)\rangle = g_+(t)|B^0\rangle + \frac{q}{p}g_-(t)|\overline{B}^0\rangle$$
$$|\overline{B}^0(t)\rangle = \frac{p}{q}g_-(t)|B^0\rangle + g_+(t)|\overline{B}^0\rangle \tag{2.32}$$

where

$$g_+(t) = e^{-iMt}e^{-\frac{1}{2}\Gamma t}cos\left(\frac{\Delta m_B t}{2}\right)$$
$$g_-(t) = e^{-iMt}e^{-\frac{1}{2}\Gamma t}sin\left(\frac{\Delta m_B t}{2}\right) \tag{2.33}$$

It therefore follows that the probability that a state beginning as a pure $|B^0\rangle$ will decay as a $|\overline{B}^0\rangle$ will oscillate sinusoidally with a frequency that depends on Δm_B.

2.3.3 Three Types of CP Violation

CP violation can manifest itself in the standard model in three distinct ways and each of these ways will now be discussed.

CP Violation in Decay

Direct CP violation occurs when the amplitude for a decay process and its CP conjugate process are not equal and it is the only type of CP violation possible in charged B decays. It has been observed in K decays [17, 18] and B decays [19] The amplitudes for the decay $B \to f$ and its CP conjugate $\overline{B} \to \overline{f}$, where f and $\overline{f}$ are any final states, are given by:

$$A_f = \langle f|H|B\rangle = \sum_j A_j e^{i(\delta_j+\phi_j)}, \quad \overline{A}_{\overline{f}} = \langle \overline{f}|H|\overline{B}\rangle = \sum_j A_j e^{i(\delta_j-\phi_j)} \tag{2.34}$$

Where A_j, δ_j and ϕ_j are the amplitude, strong (or CP-conserving) phase and weak (or CP-violating) phase of the contributing process. For CP violation to occur the following condition must be met:

$$A_f \neq \overline{A}_{\overline{f}} \tag{2.35}$$

In order for this condition to be met there must be contributions from at least two different processes with different strong and weak phases. If there are two contributing processes then:

$$|A_f|^2 - |\overline{A}_{\overline{f}}|^2 = -2\sum_{ij} A_i A_j sin(\phi_i - \phi_j) sin(\delta_i - \delta_j) \tag{2.36}$$

It is helpful, experimentally, if these two contributing processes are of similar magnitudes. The observed asymmetry can be written as:

$$A_{CP}^D = \frac{\Gamma(\overline{B} \to \overline{f}) - \Gamma(B \to f)}{\Gamma(\overline{B} \to \overline{f}) + \Gamma(B \to f)} = \frac{|\overline{A}_{\overline{f}}/A_f|^2 - 1}{|\overline{A}_{\overline{f}}/A_f|^2 + 1} \tag{2.37}$$

CP Violation in Mixing

CP violation in mixing is observed as a difference in the rates for the $P^0 \to \overline{P}^0$ and $\overline{P}^0 \to P^0$ transitions. The difference is observed due to an interference between box diagrams (such as those in Figure 2.2) proceeding via the t quark and those proceeding via other flavours. It occurs when the mass eigenstates are not CP eigenstates :

$$\mathbf{CP}|P_{1,2}\rangle \neq \pm|P_{1,2}\rangle \tag{2.38}$$

or in other words the mass eigenstates are described by Equation 2.23 as opposed to Equation 2.19. Following a similar process to the one used to derive

Equation 2.21 it can be shown that for the B system, as described by Equation 2.24, q/p must equal 1 in order for $|B_{L,H}\rangle$ to be CP eigenstates, thus conserving CP. For a physically meaningful result however, we require a phase convention-independent approach so that δ can take on any value, not just zero.

$$\mathbf{CP}|B_{L,H}\rangle = \pm|B_{L,H}\rangle \tag{2.39}$$

$$\text{if} \qquad |\frac{q}{p}|e^{i(arg(p)-\delta)} = e^{i\,arg(p)} \tag{2.40}$$

$$\text{and} \qquad |\frac{p}{q}|e^{i(arg(p)+\delta)} = e^{i\,arg(q)} \tag{2.41}$$

From this it can be seen that there is always a value of δ that satisfies Equation 2.39 provided that $|q/p| = 1$. For CP violation to occur it is required that:

$$\left|\frac{q}{p}\right| = \left|\sqrt{\frac{\langle\overline{B}^0|H|B^0\rangle}{\langle B^0|H|\overline{B}^0\rangle}}\right| \neq 1 \tag{2.42}$$

CP violation in mixing is also called indirect CP violation and was the first type to be shown experimentally in the K system. The level of indirect CP violation in the B system is expected to be small due to the fact that $|q/p| \approx 1$ as implied by Equation 2.27

CP Violation in the interference between decays with and without mixing

The third form of CP violation arises from the interference between the mixing and decay processes. This is observed in the decays of neutral mesons to the same final state, which must therefore be a CP eigenstate ($f = \overline{f} = f_{CP}$). if A_{fCP} is the amplitude of $B^0 \to f_{CP}$ and $\overline{A}_{fCP}$ is the amplitude of $\overline{B}^0 \to f_{CP}$ then we can define the following phase convention-independent quantity:

$$\lambda_{fCP} = \frac{q}{p}\frac{\overline{A}_f}{A_f} \tag{2.43}$$

If λ_{fcp} is not equal to unity then CP violation occurs and can be due to either direct ($\left|\frac{\overline{A}_f}{A_f}\right| \neq 1$) or indirect ($\frac{q}{p} \neq 1$) CP violation. It can also occur, however, when there is no CP violation in mixing or decay and for this to be true the imaginary part of λ_{fCP} is required to be non-zero:

$$\Im(\lambda_{fCP}) \neq 0, \qquad |\lambda_{fCP}| = 1 \tag{2.44}$$

When this occurs, λ_{fCP} becomes a pure phase that can be calculated without hadronic uncertainties. Using Equation 2.32 the time dependent amplitudes for

B^0, $\overline{B}^0 \to f_{CP}$ can be expressed as:

$$\begin{aligned}\langle f_{CP}|\mathbf{H}|B^0(t)\rangle &= A_{fCP}(g_+(t) + \lambda_{fCP}g_-(t)) \\ \langle f_{CP}|\mathbf{H}|\overline{B}^0(t)\rangle &= A_{fCP}\frac{p}{q}(g_-(t) + \lambda_{fCP}g_+(t))\end{aligned} \tag{2.45}$$

The rates of these processes are obtained by taking the modulus squared of these amplitudes:

$$\begin{aligned}\Gamma(t)(B^0 \to f_{CP}) &= \left|\langle f_{CP}|\mathbf{H}|B^0(t)\rangle\right|^2 \\ &= |A_{fCP}|^2 e^{-\Gamma t}\left[\frac{1+|\lambda_{fCP}|^2}{2} + \frac{1-|\lambda_{fCP}|^2}{2}cos(\Delta m_B t)\right. \\ &\quad \left. - \Im(\lambda_{fCP})sin(\Delta m_B t)\right] \\ \Gamma(t)(\overline{B}^0 \to f_{CP}) &= \left|\langle f_{CP}|\mathbf{H}|\overline{B}^0(t)\rangle\right|^2 \\ &= |A_{fCP}|^2 e^{-\Gamma t}\left[\frac{1+|\lambda_{fCP}|^2}{2} - \frac{1-|\lambda_{fCP}|^2}{2}cos(\Delta m_B t)\right. \\ &\quad \left. + \Im(\lambda_{fCP})sin(\Delta m_B t)\right]\end{aligned} \tag{2.46}$$

where the $g_\pm$ are used as defined as in Equation 2.33 and $|q/p| = 1$ is assumed to be true. The time dependent asymmetry, $A^I_{CP}(t)$, is the difference between the

two rates above as a fraction of their sum:

$$\begin{aligned} A^I_{CP}(t) &= \frac{\Gamma(t)(\overline{B}^0 \to f_{CP}) - \Gamma(t)(B^0 \to f_{CP})}{\Gamma(t)(\overline{B}^0 \to f_{CP}) + \Gamma(t)(B^0 \to f_{CP})} \\ &= \frac{-(1-|\lambda_{fCP}|^2)cos(\Delta m_B t) + 2\Im(\lambda_{fCP})sin(\Delta m_B t)}{1+|\lambda_{fCP}|^2} \\ &= -Cf_{CP}cos(\Delta m_B t) + Sf_{CP}sin(\Delta m_B t) \end{aligned} \tag{2.47}$$

where C and S, the direct and indirect asymmetries, are:

$$C_{fCP} = \frac{1-|\lambda_{fCP}|^2}{1+|\lambda_{fCP}|^2} \quad \text{and} \quad S_{fCP} = \frac{2\Im(\lambda_{fCP})}{1+|\lambda_{fCP}|^2} = sin(2\beta) \tag{2.48}$$

With $|\lambda_{fCP}| = 1$ it can be seen that Equation 2.47 reduces to:

$$A^I_{CP}(t) = \Im(\lambda_{fCP})sin(\Delta m_B t) \tag{2.49}$$

For most B decays the level of direct and indirect CP violation is negligible. CP violation in interference between decays with and without mixing occurs at a much greater level and, with $|\lambda_{fCP}| \approx 1$, is the easiest type to measure at *BABAR*

2.4 D Meson Spectroscopy

Having introduced the standard model and one of the motivations behind the *BABAR* experiment, CP violation, it is now important to discuss the theory behind the analysis. This thesis is a study of the properties of the $D_{sj}(2317)$ and $D_{sj}(2460)$ mesons and in order to begin that study it is useful to introduce the various mesons in the D system and the notion of excited states. There will also be some discussion of the D_{sj} themselves as well as giving an introduction to the approximations needed to understand these properties.

2.4.1 Mesons as $q\overline{q}$ Bound States.

This thesis is concerned with a number of mesons, specifically those containing a charm quark, and how they are arranged inside bound states. The quark content is very important, but the only way to uniquely specify the mesons is if the quantum numbers are known. Physical properties like the mass, lifetimes or the allowed decay chains of a meson are dependent on the specific quantum numbers in the system. The ground state of any given $q\overline{q}$ combination is defined as the lowest energy configuration of the allowed quantum numbers. Excited states are those with different quark configurations that have higher energies.

The Ground State Mesons of Interest

Of the six types of quarks, all form bound states aside from the top quark which has too short a lifetime so decays prior to hadron formation. This gives 25 possible $q\overline{q}$ combinations and all of these have been observed as mesons. As discussed in Section 2.2.3 the similarity between the up and down quarks causes the $u\overline{u}$ and $d\overline{d}$ combinations to produce superpositions, as is the case for pions. The other quark masses are much larger and so quantum interference is heavily suppressed for other states and they therefore have a well defined quark content. Table 2.4 shows the ground state mesons that are of interest in this thesis as well as their quark content, mass and isospin.

Meson	Quark Content	I	J^P	M (MeV/c^2)
$K^{\pm}$	$u\overline{s}, \overline{u}s$	1/2	0^-	493.68
$\pi^{\pm}$	$u\overline{d}, \overline{u}d$	1	0^-	139.57
π^0	$\frac{1}{\sqrt{2}}(u\overline{u} - d\overline{d})$	1	0^-	134.98
$D^0, \overline{D}^0$	$c\overline{u}, \overline{c}u$	1/2	0^-	1864.84
$D^{\pm}$	$c\overline{d}, \overline{c}d$	1/2	0^-	1869.62
$D_s^{\pm}$	$c\overline{s}, \overline{c}s$	0	0^-	1968.49
$B^{\pm}$	$u\overline{b}, \overline{u}b$	1/2	0^-	5279.17
$B^0, \overline{B}^0$	$d\overline{b}, \overline{d}b$	1/2	0^-	5279.50

Table 2.4: *Ground state properties for the mesons of interest to this thesis*

2.4.2 Orbital Excitations

The notion of excited states was explained above in terms of quark-quark interactions leading to quantized energy levels above the ground state. Predicting the physical properties of excited states is hard as perturbative methods can't be used due to the fact that the QCD interaction inside mesons is outside the region of perturbative QCD. In order to do this various approximations are needed such as Heavy Quark Effective Theories (HQET) or Lattice QCD and these are described briefly in Section 2.4.4.

The Excited State Mesons of Interest

The properties of the ground state mesons that are of interest to this thesis were described above. Table 2.5 shows the excited state mesons that are of particular relevance.

Meson	Quark Content	I	J^P	M (MeV/c^2)
ϕ^0	$s\overline{s}$	0	1^-	1019.45
$K^{*0}, \overline{K}^{*0}$	$d\overline{s}, \overline{d}s$	1/2	1^-	896.00
$D^{*0}, \overline{D}^{*0}$	$c\overline{u}, \overline{c}u$	1/2	1^-	2006.97
$D^{*\pm}$	$c\overline{d}, \overline{c}d$	1/2	1^-	2010.27
$D_s^{*\pm}$	$c\overline{s}, \overline{c}s$	0	$?^?$	2112.30

Table 2.5: *Excited state properties for the mesons of interest to this thesis*

2.4.3 The D_{sJ} System

The unexpected discovery at *BABAR* of a narrow meson state decaying to $D_s^+\pi^0$ near the mass of 2.32 GeV/c^2 [20] was of great interest to both theorists and experimentalists alike. Experimentally the state was quickly confirmed by CLEO [21] and Belle [22]. The CLEO collaboration also observed a narrow resonance decaying to $D_s^{*+}\pi^0$ near the mass of 2.46 GeV/c^2 which was also seen by Belle and confirmed by *BABAR* [23]. It was recognised in the *BABAR* paper that the new lower mass state was consistent with being a $c\bar{s}$ meson and so it was assigned the name $D_{sJ}^*(2316)$, with the higher mass state given the name $D_{sJ}^*(2460)$.

At the time, there were 4 known states of the $c\bar{s}$ system, including the $^1S_0$ ground state meson (D_s^+) and the $^3S_1$ ground state meson ($D_s^*(2112)$). There had also been observations of the $D_{s1}^+(2536)$ meson, which preferred $J^P = 1^+$, and the $D_{s2}^+(2573)$ meson, which is consistent with $J^P = 2^+$. The later two mesons were discovered in their decays to D^*K and D^0K^+ respectively.

In the limit of large charm quark mass [24], the spectroscopy of the $c\bar{s}$ states is relatively simple. In that limit the total angular momentum, $\vec{j} = \vec{l} + \vec{s}$, of the light quark is conserved and therefore the P-wave states, all of which have positive parity, have $j = 3/2$ or $j = 1/2$. Combining the $j = 3/2$ state with the spin of the heavy quark gives an angular momentum of $J = 2$ or $J = 1$.

This defines a doublet with $J^P = 1^+$ and $J^P = 2^+$ which are identified as the $D_{s1}^+(2536)$ and $D_{s2}^+(2573)$ mesons respectively. Combining the $j = 1/2$ state with the spin of the heavy quark gives an angular momentum of $J = 1$ or $J = 0$. Hence a doublet exists with $J^P = 0^+$ and $J^P = 1^+$ which are hypothesized to be the discovered $D_{sJ}^*(2316)$ and $D_{sJ}^*(2460)$ mesons. Figure 2.3 shows the spectrum of D_s states along with their predicted quantum numbers.

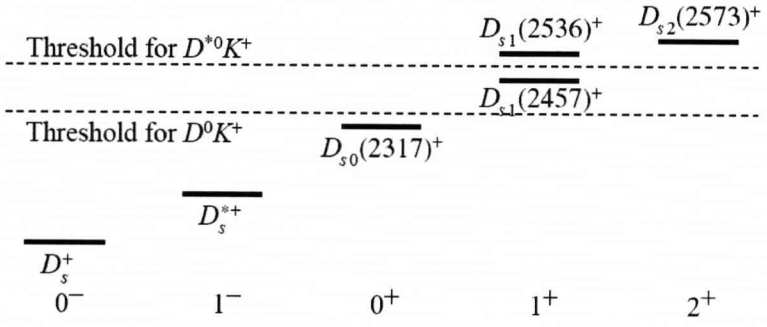

Figure 2.3: *The spectrum of $c\bar{s}$ states*

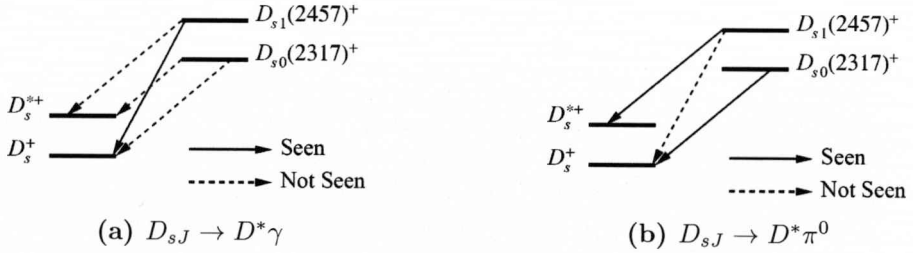

(a) $D_{sJ} \to D^*\gamma$ **(b)** $D_{sJ} \to D^*\pi^0$

Figure 2.4: *D_{sJ} to D_s Transitions*

Figures 2.4 (a) and 2.4 (b) show the possible transitions between the D_{sJ} and D_s states and which ones have been observed to date. The following section addresses why, given that the discovered particles are theorised to be a doublet with total light-quark angular momentum of $j = 1/2$, their discovery was unexpected.

2.4.4 Theoretical Predictions

The discovery of the new $c\bar{s}$ mesons was unexpected in the sense that it was narrow, that it was observed in the isospin violating D_s^0 channel and that its mass was smaller than expected. The previously discovered members of the $j = 3/2$ doublet were expected to have small width but the newly discovered D_{sJ} mesons were expected to have large widths and hence be difficult to detect [25]. The first two reasons can be explained as a consequence of the low mass, since the $D^{(*)}K$ decays modes are not allowed kinematically and therefore the states are narrow and more easy to detect experimentally. The masses however, are lower than those predicted by a variety of theoretical models, for example Godfrey and Isgur [26] predicted the $D_{sJ}(2317)$ and $D_{sJ}(2460)$ masses to be 160 MeV/c^2 and 70 MeV/c^2 higher than was found experimentally.

Since the potential model calculations, as well as some others such as a lattice calculation [27], cannot account for the masses of the new states, a wide variety of possible explanations have been put forth including:

- Mesons comprising one heavy and one light quark can be approximated as having two separate static potentials, one arises as the zeroth component of a vector potential and the other as a Lorentz scalar. The measurement of three p-wave states suffices to predict the mass of the fourth [27]

- Instead of having a conventional $c\overline{s}$ assignment, the discovered particle is a possible quasi-nuclear DK bound state with a mass of 2.3 GeV. Isospin mixing is expected in hadron molecules and a dominantly $I = 0$ DK state with some $I = 1$ admixture could explain the narrow width and observed decay to $D_s^+\pi^0$ [28]

- The $D_{sJ}^+(2317)$ is described as a quasi-bound scalar $c\overline{s}$ state. The low mass of the $D_s(2317)$ can be explained by the existence of a strong OZI-allowed coupling to the nearby DK threshold [29]

- The charmed-strange resonance at 2.3 GeV/c suggests a possible four quark state $cq\overline{qq}$ [30, 31, 32]

- The discovery of the $D_s(2317)$ is consistent with a heavy $J^P(0^+, 1^+)$ spin multiplet, the chiral partner to the $(0^-, 1^-)$ ground state [33, 34, 35]

- The discovered resonance in the $D_s\pi^0$ spectrum can be described in terms of residual $D\pi$ interactions [36]

- All charmed and charmed-strange mesons can be incorporated by the Kaluza-Klein approach. The $D_s(2317)$ fits in with the seventh story of the Kaluza-Klein tower of (KK) excitations for the $D_s\pi$ system and the $D_s(2460)$ fits in with the seventh story of the Kaluza-Klein tower of (KK) excitations for the DK system [37]

- The new resonances observed can be explained by the mixing of D_s mesons with 4-quark states. The narrow states observed in $D_s^+\pi^0$ and $D_s^{*+}\pi^0$ are primarily p-wave excited D_{sJ}^* states while the predominately 4-quark states are shifted above the DK threshold and should be broad [38]

- The $D_{sJ}(2317)$ state is a super-position of three different interpretations; The missing triplet s-wave $(J^P = 0^+)|c\bar{s}\rangle$ quarkonium state, a "single bag" $(|(c\bar{s}u\bar{u}\rangle + |c\bar{s}d\bar{d}\rangle)/\sqrt{2}$ isosinglet state and as an isosinglet "molecular" bound state $(|K^+D^0\rangle + |K^0D^+)/\sqrt{2}$ of two separate hadrons [39]

There were however two theoretical calculations using Heavy Quark Effective Theories (HQET) that predicted low mass D_{sJ} states prior to their discovery [34, 40]. Newer HQET calculation [41, 42] as well as a lattice calculation [43] and a calculation using the MIT bag model [44] have also accounted for the masses of these new states. The predictions given by these models are given in Table 2.6.

Model	Theoretical Predictions		Experimental Results	
	$m(D_{s0}^+)$	$m(D_{s1}^+)$	$m(D_{s0}^+)$	$m(D_{s1}^+)$
HQET [41]	2420 ± 130	2610 ± 136	2317.6 ± 1.3	2463.0 ± 1.7
HQET [42]	2304 ± 25	2446 ± 25		
Lattice QCD [43]	2370 ± 16	2441 ± 10		
MIT Bag Model [44]	2288	2465		

Table 2.6: *Theoretical Predictions for D_{s0}^+ and D_{s1}^+. The D_{s0}^+ and D_{s1}^+* correspond to the 0^+ and 1^+ states in all of the models.

Lattice QCD was designed as a tool to calculate observables in the non-perturbative region of QCD. The continuum quark and gluon fields are replaced by lattice fields occurring on the sites and links of the lattice respectively. The predictions given consider the quenched approximation which sets the determinant of the lattice dirac operator to be equal to 1, analogous to making the virtual quarks infinitely heavy.

The MIT bag model proposes that a strongly interacting particle is a finite region of space to which fields are confined. The confinement is achieved by requiring that the finite region has a constant potential energy per unit volume and this region is called a "bag".

HQET Models

As mentioned above, there are a number of explanations that have been proposed for the lower mass states, and this will be a brief summary of one of those explanations. As discussed in section 2.4.1 D mesons are bound states containing one *heavy* quark (c) and one *light* quark (u, d, s) such that there is a large mass difference $m_c \gg m_{u,d,s}$. This allows the use of HQET in which solutions are determined under the approximation $m_c \to \infty$ and then corrections are added by higher order terms in powers of $1/m_c$. In order to be able to make this ex-

pansion it is necessary that $m_c \gg \Lambda_{QCD}$, where Λ_{QCD} is the QCD confinement energy. This approach is equivalent to fixing the c quark as a static source of electromagnetic and colour fields in which the light quark moves. The reason for this is that in the $m_c \to \infty$ limit of a heavy-light meson, the typical momenta exchanged between mesons are comparable to Λ_{QCD} which is this approximation is much smaller than m_c. This means that the recoil of the heavy, charm quark can be neglected and so it can be treated as a static field.

HQET theories lead to the introduction of a couple of symmetries called Heavy Flavour Symmetry (HFS) and Heavy Spin Symmetry (HSS). Heavy flavour symmetry is introduced for heavy-light mesons in the heavy mass limit and corresponds to an invariance under the flavour transformation $b \to c$. Such an operation cannot change the interactions within the meson state provided that both quarks satisfy $m_{c,b} \gg \Lambda_{QCD}$. Heavy Spin symmetry corresponds to the invariance of meson states under rotations in s_Q space where s_Q is the spin of the heavy quark. With the heavy quark limit there is a vanishing chromomagnetic moment, μ_Q associated to it, where:

$$\mu_Q = \frac{g}{2m_Q} \tag{2.50}$$

Heavy Spin Symmetry predicts that the two states in each j_q doublet should be degenerate in energy. In the finite mass limit, the chromomagnetic moment defined above, is non-zero which gives an s_Q contribution to meson energies. The degeneracies of the $m_Q \to \infty$ case are lifted which splits the j_q doublets into distinct mass states. This can then be used as a description of split j_q doublets, such as in the D_s sector and be used to make predictions of the mass differences as such splittings. In reality the initial approximation $m_{c,b} \gg \Lambda_{QCD}$ does not hold as the quark masses are relatively close to the confinement energy, but the power of the theory lies in the hierarchical arrangement of corrections (in powers of $1/m_c$).

2.4.5 Motivation for Investigating $B \to D_{sj}D$ decays

There are a number of different explanations for the low mass D_{sJ} particles, some of which were introduced in the previous section, however they suggest the need to verify the hypothesised quantum numbers of the two states. The constraints provided by B mesons at the $\Upsilon(4S)$ resonance allow for the properties of these mesons to be studied and that's the aim of this thesis. Chapter 3 gives a detailed description of the experimental conditions at *BABAR* whilst Chapter 5 gives an overview of the analysis undertaken.

Chapter 3

The *BABAR* Experiment

3.1 Introduction

The primary motivation behind the construction of the *BABAR* detector was to study CP-violating asymmetries in the decay of B mesons to CP eigenstates. There were also many secondary goals such as precision measurements of the rates of rare decays, detailed studies of τ and charm physics and contributions towards precision spectroscopy. This section gives an outline of the design of the *BABAR* detector and PEP-II accelerator, shown in Figure 3.1, with these physics considerations in mind.

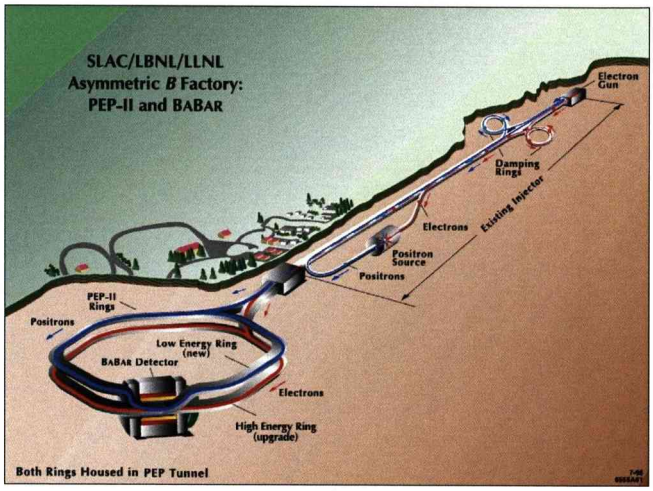

Figure 3.1: *SLAC linac and PEP-II storage rings*

3.2 The PEP-II Accelerator

3.2.1 PEP-II Overview

The *BABAR* experiment uses the PEP-II accelerator which collides electrons and positrons at asymmetric energies. The collider operates at a centre of mass of 10.58 GeV which is chosen as it is $\Upsilon(4S)$ resonance, which decays almost exclusively to B meson pairs. PEP-II collides a beam of 9 GeV electrons with a beam of 3.1 GeV positrons to provide a Lorentz boost of $\beta\gamma = 0.56$ which allows a difference in decay time to be seen as a separation in z of the decay vertices. This is essential in order to study time-dependent CP asymmetries. A complete description of the PEP-II machine can be found in [45]

3.2.2 PEP-II Injection System

Figure 3.1 shows the two mile long linear accelerator (linac) which acts as the source of electrons and positions injected into the PEP-II storage rings. Electron bunches, created by an electron gun at one end of the linac, are stored in the north damping ring. They are then accelerated by the linac to 9.0 GeV where they are then injected into the High Energy Ring (HER). Separate electron bunches are produced by the electron gun and then collided with a Beryllium target. Positron bunches are produced by this process and are stored in the south damping ring, before being accelerated by the linac to 3.1 GeV. From there they are then injected into the Low Energy Ring (LER). There are around 10^{10} particles per bunch and the bunch crossing rate at *BABAR* is 238 MHz which helps achieve the large luminosities the physics program requires.

Originally, PEP-II operated by filling the HER and LER to a maximum value, at which point the system would stop injection and begin data taking. This continued until the decreasing Luminosity reached a lower limit at which data taking would stop. At that point, the injection system would start again and this process was repeated in a cycle. One advantage of this method was that backgrounds were high during injection and so during these times the Detector could be "ramped down" and protected against radiation damage. The disadvantage of

this method was that it didn't maximise the integrated luminosity as data taking wasn't taking place during the periods of injection.

Another method, which was introduced in 2004, is to inject continuously whilst also taking data and this method is known as trickle injection. This method is more technically challenging and increases machine backgrounds but it increases the integrated luminosity produced. The reason for this is because it is possible to keep the instantaneous luminosity constant at a high level without losing time due to injection and thus increasing the production of B mesons by up to 50%. Figure 3.2 shows how the Instantaneous Luminosity changes with respect to time, and demonstrates the increase in Integrated Luminosity due to trickle injection.

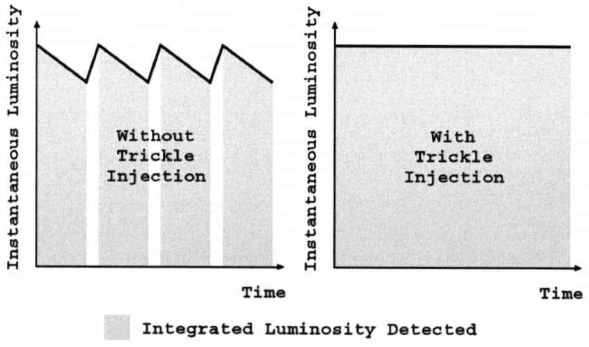

Figure 3.2: *Effect of trickle injection on integrated luminosity)*

3.2.3 PEP-II Interaction Region

To achieve the high luminosities needed the beams are divided into many low charge bunches which minimises beam-beam interference. It is also necessary to

keep the two beams separated until just before the Interaction point (IP) so that secondary collisions, which could increase backgrounds, cannot occur. In order to separate the beams they are subjected to magnetic fields generated by strong dipole magnets located inside the *BABAR* detector. The magnets also have an effect on both the detector acceptance and the background conditions. Figure 3.3 shows the layout of the interaction region and shows the beams being separated by the same dipole magnets (labeled B1) before and after the IP. Focusing of the beam is achieved by sets of quadruple magnets, (labeled Q). The HER beam is focused by magnets Q4 and Q5 whereas the LER beam is focused by magnet Q2. Q1 is a permanent magnet, is partially enclosed in the Detector volume and is used as the final focus for both beams.

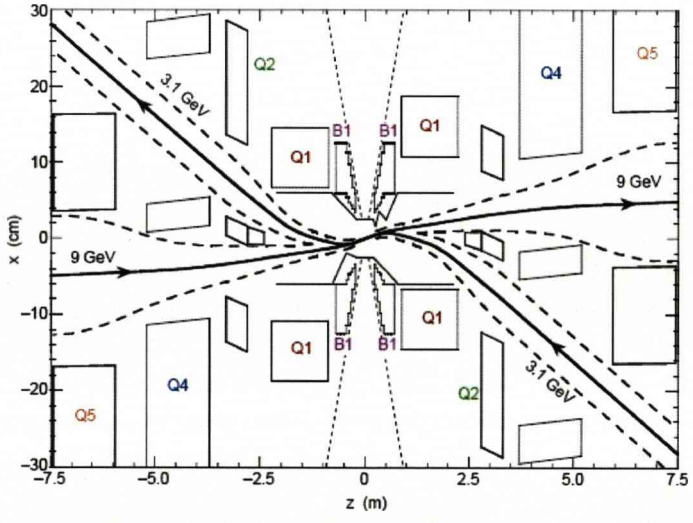

Figure 3.3: *Plan view of the PEP-II interaction region (The vertical scale has been exaggerated)*

3.2.4 PEP-II Backgrounds

Machine Backgrounds lead to an increased occupancy in the *BABAR* detector causing physics measurements to be degraded due to increased dead-time. They can also lead to radiation damage in the detector systems through long term exposure or short acute doses.

Synchrotron radiation is particularly problematic due to the complicated optics near the IP. The geometry of the interaction region was designed so that the majority of the synchrotron radiation, from the extra bending magnets, passes through the detector with minimal interaction. In order to help prevent interaction with the beam pipe, copper masks have been used.

Another source of background is due to "lost" particles striking the beam pipe wall or gas molecules in the beam pipe. These are beam particles that undergo bremsstrahlung or Coulomb interactions with gas molecules in the beam pipe and have momenta that fall outside the maximum range of the storage rings. It is important to keep a very good vacuum in the beam pipe near the IP, in order to reduce this background.

Bhabha scattering is the scattering of an electron and a positron and causes a further source of background. When an electron or positron hits material a short distance away from the IP it causes electromagnetic showers that enter the

detector. This machine background has become more of a problem with increased luminosity is the largest source of machine background.

3.3 The *BABAR* Detector

BABAR is designed as a general purpose detector optimised for its primary physics goals of precision measurements of CP violation parameters as well as the study of B, tau and charm physics. In order to achieve these goals the detector must satisfy the following requirements:

- To maximise the physics potential of the asymmetric PEP-II machine, the *BABAR* detector is itself asymmetric in design in order to obtain the maximum coverage in the $\Upsilon(4S)$ CM frame.
- High reconstruction efficiency for charged and neutral particles
- Good position and momentum resolution for charged particles over the momentum range 60 MeV/c – 4 GeV/c.
- Good energy and angular resolution for neutral particles over the energy range 20 MeV/c – 4 GeV/c, especially important for π^0 and η resolution.
- Excellent vertex resolution in all three dimensions to allow for accurate

measurements of the decay time difference between the two B mesons, as well as reconstructing secondary charm and τ vertices.

- Excellent particle identification for e, μ, π, K and p over a wide range of momenta. This is essential for identifying the hadron species of the non-CP B in CP violation measurements and for separating important final states such as $K^{\pm}\pi^{\mp}$ and $\pi^{\pm}\pi^{\mp}$.

- The detector must be able to operate under the high background conditions expected at high luminosities.

- A reliable and efficient data acquisition system (DAQ) which can handle the large volume of data produced at high luminosities.

- An efficient, flexible and redundant trigger that can reduce the event rate to a level that can be handled by the DAQ without losing important physics events.

To achieve the criteria set out above, whilst taking into account other factors such as cost and reliability, the final design consists of a system containing 5 sub-detectors as shown in Figure 3.4.

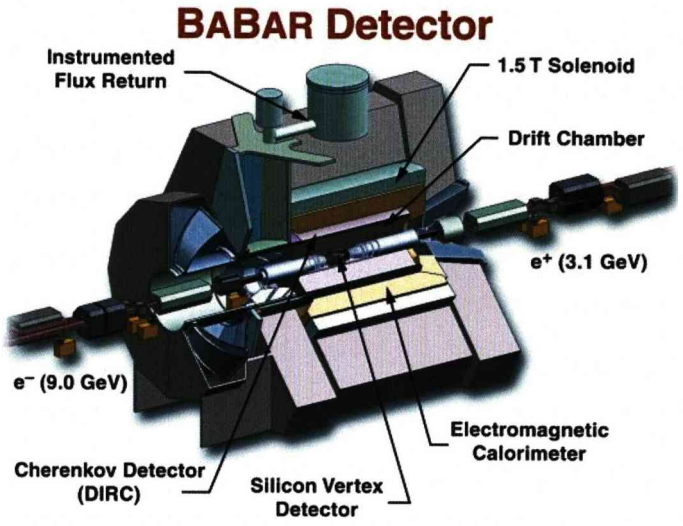

Figure 3.4: *The BABAR detector*

The 5 sub-detectors, starting with the most innermost detector, are as following:

- Silicon Vertex Tracker (SVT)
- Drift Chamber (DCH)
- Detector of Internally Reflected Cherenkov radiation (DIRC)
- Electromagnetic Calorimeter (EMC)
- Instrumented Flux Return (IFR)

The first four of these are enclosed in a superconducting magnetic coil which provides a 1.5 T magnetic field. A complete description of the detector can be found in [46].

BABAR uses a right handed co-ordinate system with the origin at the Interaction Point (IP). The z-axis corresponds to the principle axis of the Drift Chamber in the direction of the HER. The y-axis points vertically upwards and the x-axis points horizontally outwards from the centre of the PEP-II ring. The polar (θ) and azimuthal (ϕ) angles are defined as in the standard polar co-ordinate system.

Table 3.1 details the different data taking periods of the *BABAR* detector and the luminosity provided by each run. The analysis contained within this thesis is based on the data taken from runs 1-5.

Run	Begin	End	Luminosity (fb^{-1})
Run 1	22 Oct 1999	28 Oct 2000	23.62
Run 2	10 Feb 2001	30 Jun 2002	70.30
Run 3	08 Dec 2002	27 Jun 2003	35.79
Run 4	17 Sep 2003	31 Jul 2004	111.97
	Trickle Injection implemented		
Begin replacing IFR RPCs with LSTs,			
Run 5	16 Apr 2005	17 Aug 2006	148.57
Remaining IFR Barrel RPCs replaced with LSTs			
Run 6	25 Jan 2007	04 Sep 2007	86.57
Run 7	13 Dec 2007	30 Sep 2008	54.0

Table 3.1: *Dates, Modifications and Luminosity of the different data taking periods*

3.4 The Silicon Vertex Tracker (SVT)

3.4.1 SVT Physics Requirements

The Silicon Vertex Tracker was designed in order to measure the separation of the decay vertices of the B mesons to a very high precision. This is vital for the study of time-dependent CP violation which is one of the primary goals of the experiment. To do this requires measurement of the azimuthal (ϕ) and longitudinal (z) coordinates of charged particles in the immediate vicinity of the beam-pipe. This can then be combined with coordinate information from the Drift Chamber (see Section 3.5) to provide very accurate information on the position, direction and momentum of charged particles produced by the e^+e^- collisions. The SVT is required to measure the difference in position of the two decay vertices up to a precision of $\approx 135\ \mu m$. Monte-Carlo Studies Show that this corresponds to a vertex resolution of $\approx 60\ \mu m$ [47].

There are also constraints placed by other physics aims such as requiring a resolution of 100 μm in order to make precise measurements of secondary decay vertices such as D mesons and τ leptons. The primary tracking system of *BABAR* the DCH, will not reliably detect tracks with low transverse momentum, p_T. It is therefore very important that the SVT provides excellent efficiencies for such

particles, examples of which are as slow pions from the decays of D^* mesons, a common decay product of B mesons. The SVT is the sole tracking device for charged particles with momenta less than 120 MeV/c as these will not reach the drift chamber. The SVT is also used for particle Identification, measuring the energy loss (dE/dx) of particles with momenta less than 700 MeV/c.

3.4.2 SVT Design

The SVT is made up of 5 layers of double-sided silicon strip sensors, divided azimuthally into modules, as shown in Figure 3.5. Layers 1–3 contain 6 modules each, which are tilted by 5 ° in ϕ so that they overlap slightly, providing complete coverage and aiding alignment, and so as to compensate for the lorentz angle of the drifting charge. Layers 4 and 5 have 16 and 18 modules respectively and they are arch shaped as can be seen in Figure 3.6. This arch shape is to minimise the amount of material the tracks pass through whilst increasing the angular coverage. The main purpose of the inner 2 layers is to measure the track angle accurately as this is best measured as close to the interaction point as possible so as to reduce the effect of multiple scattering. The third layer provides momentum information for low momentum (p_T) tracks that don't reach the DCH. The purpose of the outer 2 layers is for linking tracks found in the SVT to tracks in the Drift Chamber.

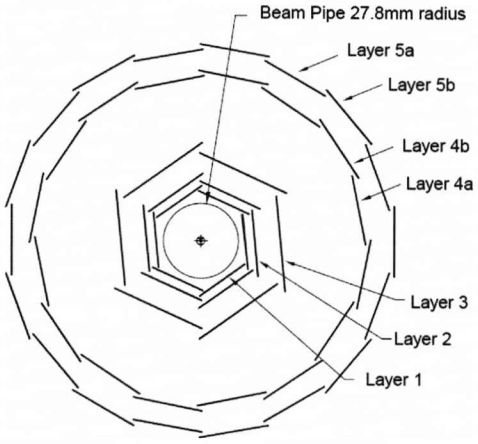

Figure 3.5: *End on view of the SVT showing the 5 Layer Structure*

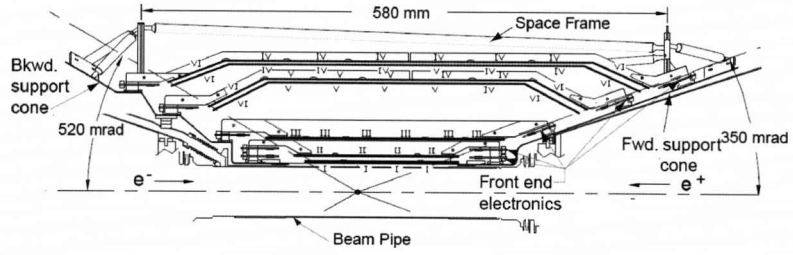

Figure 3.6: *Side on view of the SVT showing the 5 layer structure*

The strips on either side of the sensors are orthogonal to each other with the outer side of the sensors giving ϕ information and the inner side of the sensors giving information on z. Each module is split into forward and backward sections (in z) which are electronically isolated, with each half module being read out by electronics fixed to the module but outside the coverage of the detector acceptance. The readout uses a custom made radiation-hard chip which uses a time-over-threshold (TOT) technique to determine the total charge deposited in the strip. The signal is amplified and shaped before being compared with a threshold which

is dependent on background conditions. The TOT is approximately logarithmically related to the deposited charge and this allows a large range to be covered with a small number of bits. Precise knowledge of the alignment of the SVT both locally in terms of the modules, and globally in terms of the detector, is very important in order to achieve the best position and momentum resolution. The radiation limit for the SVT was 5 MRad but despite the improvements in luminosity, and corresponding radiation dose, only a small percentage of channels reached that limit.

The SVT resolution for all five layers, in both ϕ and z, is shown in figure 3.7.

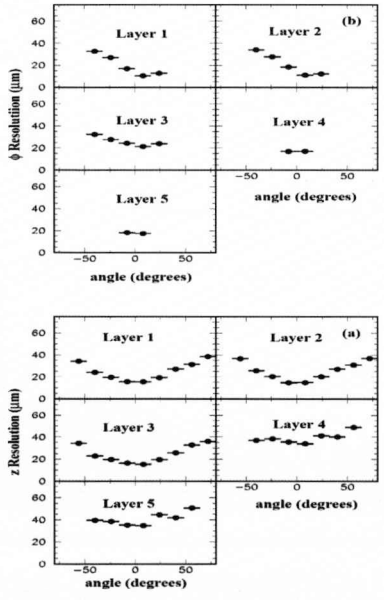

Figure 3.7: *Track resolution in the ϕ and z directions as a function of the track polar angle, for each SVT Layer*

3.5 The Drift Chamber (DCH)

3.5.1 DCH Physics Requirements

The DCH is the main charged particle tracking device of the *BABAR* detector. In order to do this it is required to make precision measurements of the momenta and angular position of charged particles. The DCH is also used to provide dE/dx information which is required for particle identification, especially at low momenta where the DIRC (see Section 3.6) is not effective. In order to be effective the DCH must cover as large a solid angle as possible whilst minimising the amount of material that the particles pass through. The DCH is required to perform under harsh background conditions produced by the PEP-II machine.

3.5.2 DCH Design

The DCH, as shown in Figure 3.8, is a 2.8m long cylinder positioned asymmetrically around the Interaction Point as to gain increased coverage in the forward direction. The chamber has an inner radius of 23.6 cm, an outer radius of 80.9 cm and is filled with a low mass gas mixture containing helium and isobutane in a ratio of 4:1. The reason for using that mixture is to provide good spatial and dE/dx resolution, a short drift time and reduce multiple scattering. A small

amount of water vapour (0.3%) is also added to prolong the life of the chamber.

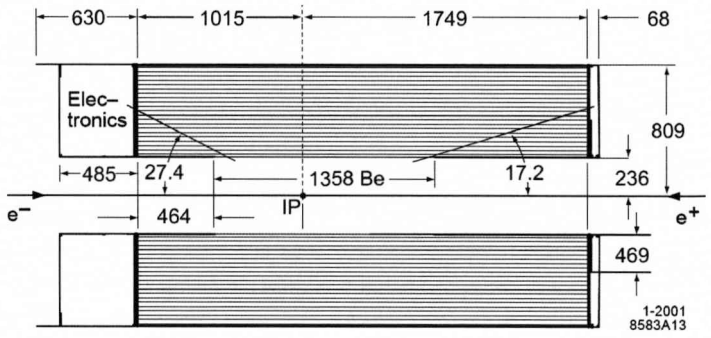

Figure 3.8: *Side on view of the DCH with dimensions in mm*

Field wires and sense wires extend between the two ends of the DCH and together they create hexagonal drift cells in the x-y plane. There are 7,104 of these drift cells and they are typically 1.2×1.8 cm^2 in size. Each cell consists of a single 20μm diameter gold plater tungsten-rhenium sense wire surrounded by six gold plated aluminium field wires which are 120μm or 80μm in diameter. These cells then form layers around the axis of the drift chamber with a group of 4 layers forming a "superlayer". The complete DCH contains 10 "superlayers" and Figure 3.9 shows the cell layout for the first 4 superlayers.

The sense wires are held at a high, positive voltage whilst the field wires are grounded, which creates an electric field with almost circular symmetry over most of the cell. The wires in 6 of the 10 superlayers are orientated at a small angle relative to the z axis which allows positional information to be extracted. The superlayers alternate between axial (A) and positive and negative stereo (U,V) from

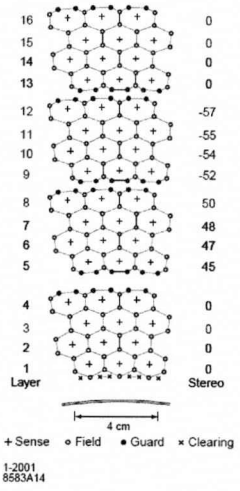

Figure 3.9: *The cell layout for the first four superlayers in the DCH*

the innermost superlayer outwards according to the pattern AUVAUVAUVA. The stereo angle varies from 45 mr (milliradians) in the innermost superlayer to 76 mr in the outermost superlayer. In order to track particles in the drift chamber, the individual hits in the DCH are combined to make a track, which allows the measurement of the curvature of charged particles and in turn provides information of the momenta of said particle. A hit occurs when a charged particle passes through a drift cell and ionises the gas mixture. The liberated electrons are then accelerated by the electric field towards the sense wire. These electrons can further ionise the gas to provide a "charge avalanche" towards the sense wire. To determine the drift time, and gain positional information, the leading edge of the signal is detected and digitised with a 1 ns resolution. The total charge deposited is used in order to gain information on the dE/dx of the track.

Figure 3.10 shows the track reconstruction efficiency as a function of both transverse momentum and polar angle. The figure shows these for both the design voltage of 1960V and for 1900V which was used initially as a safety precaution. The distribution of dE/dx measurements as a function of track momentum is show in Figure 3.11. The Bethe-Bloch predictions for each of the labeled particles types are displayed and demonstrate good K/π separation can be achieved up to 0.6 GeV/c.

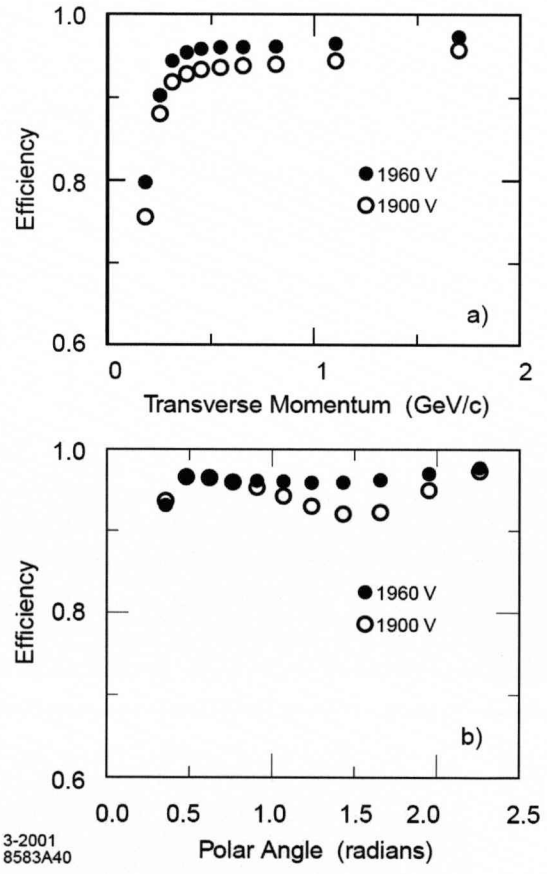

Figure 3.10: *Tracking Efficiency for the DCH as a function of p_T (top) and polar angle (bottom)*

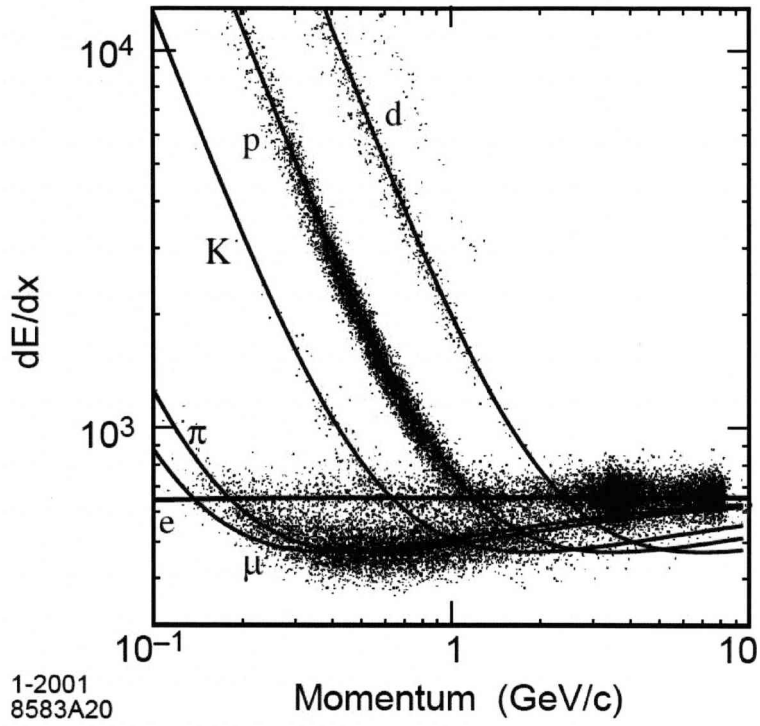

Figure 3.11: *dE/dx measurements in the DCH as a function of track momentum. The overlaid curves are Bethe-Bloch predictions for each of the labeled particles types*

3.6 The Detector of Internally Reflected Cerenkov Radiation (DIRC)

3.6.1 DIRC Physics Requirements

The DIRC is a Cherenkov ring-imaging detector and is the primary charged hadron identification system. One of its important roles is to distinguish between pions and kaons which is vital for B flavour tagging in CP violation measurements.

It is very important in order to be able to distinguish between rare two body B decays involving kaons and pions and these final state particles can have momenta of up to 4.2 GeV/c. The DCH can only provide effective separation up to 0.6 GeV/c and so it is very important for the DIRC to provide charged particle separation in the range of 0.6 GeV/c – 4.2 GeV/c.

Another requirement on the DIRC is that it is small in terms of radiation lengths, so as not to decrease the Calorimeter resolution. It must also be small so as to minimise the size and cost of the calorimeter (see Section 3.7). In order to operate in the high luminosity environment it must be able to operate in high backgrounds and have a fast signal response.

3.6.2 DIRC Design

The DIRC is a ring imaging Cherenkov detector and is used to achieve the required π/K separation and other physics goals. Cherenkov radiation occurs when a charged particle travels through a medium at a velocity greater than the speed of light in that medium. The DIRC, as shown in Figure 3.12, uses this principle as it contains quartz bars with a refractive index n=1.473, through which the charged particles will pass, producing Cherenkov photons. The photons will then travel along the quartz by total internal reflection to the back of the detector,

although some signal will be lost due to the incorrect incident angle. Any photons traveling in the forward direction will be reflected back by a mirror at the front end. At the back of the detector they enter into a water filled standoff box, which is lined with an array of photomultiplier (PMT) tubes which detect any photons.

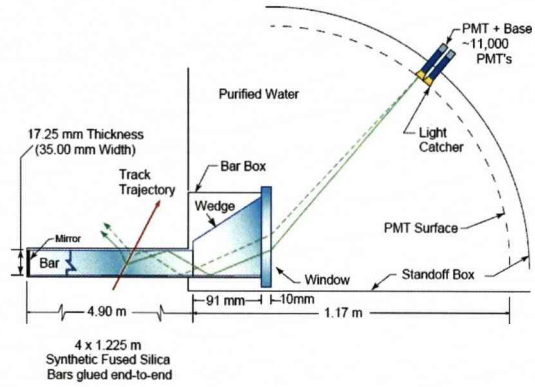

Figure 3.12: *Structure and concept of the DIRC*

The DIRC design, as shown in Figure 3.13, contains 144 synthetic quartz bars which are arranged in a 12 sided polygon around the DCH. The standoff box contains 6000 litres of purified water because it has a refractive index close to that of quartz and thus reduces any reflection at the quartz-water junction. The standoff box is lined with an array of 10,752 PMTs, each of which are 2.82 cm in diameter. To reduce the effect of the magnetic field on the PMTs there is magnetic shielding placed around the outside of the standoff box. The DIRC has a coverage from 25.5° to 141.4° in polar angle, has an acceptance of 94 % in the azimuthal angle, due to small gaps in coverage between the bar boxes, and contributes only 17 % of a radiation length for tracks at normal incidence.

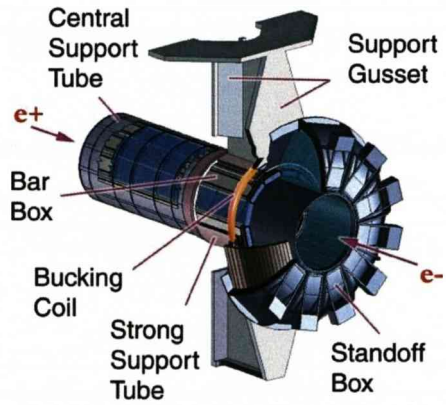

Figure 3.13: *An illustration of the DIRC particle Identification System*

Figure 3.14 shows the π/K separation as a function of momentum. The discriminating power provided by the DIRC is illustrated in Figure 3.15 which shows the peak in the $K\pi$ spectrum. It can be seen that using the DIRC information greatly reduces combinatorial background while leaving the signal unaffected.

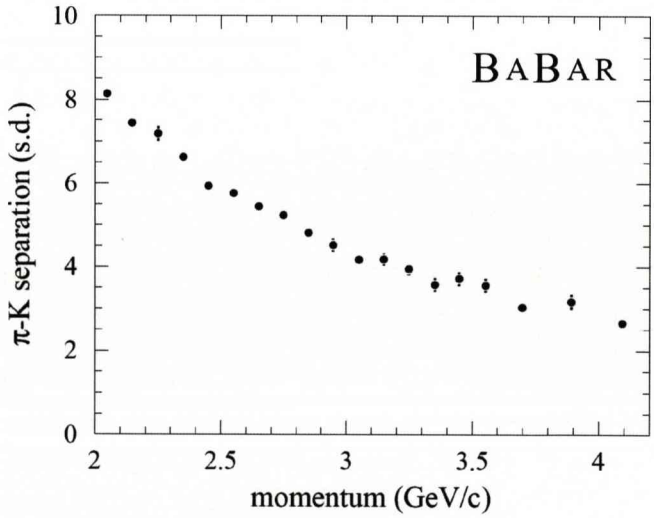

Figure 3.14: *DIRC π/K separation as a function of track momentum*

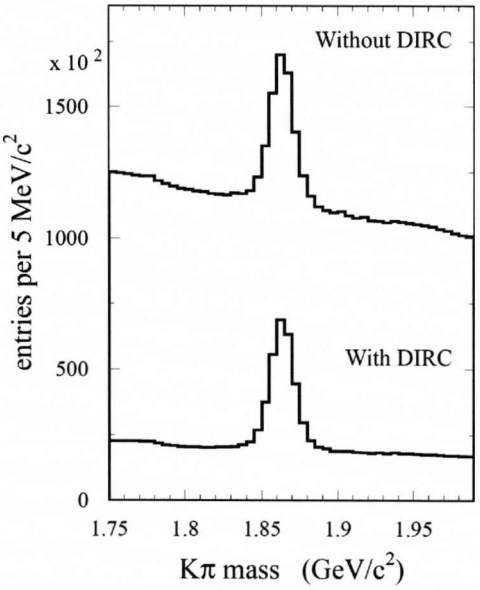

Figure 3.15: *Reconstructed $K\pi$ mass with and without the use of DIRC information for kaon identification. The peak corresponds to the decay $\overline{D}^0 \to K^+\pi^-$]*

3.7 The Electromagnetic Calorimeter (EMC)

3.7.1 EMC Physics Requirements

It is very important for the EMC to be able to detect photons efficiently, with excellent energy and angular resolution, as well as detecting them over a large energy range. There are many important B decays that include π^0 or η particles which often decay into low energy photons, and it is therefore important for the EMC to detect and measure photons down to 20 MeV. There are also processes that produce high energy photons up to 9 GeV in the laboratory frame. Examples of which are $e^+e^- \to e^+e^-\gamma$ and $e^+e^- \to \gamma\gamma$ and these are important for

calibration and luminosity monitoring. The EMC is also used for electron identification which is important for flavour tagging and in semi-leptonic B decays.

3.7.2 EMC Design

The EMC contains 6,580 thallium doped caesium iodide (CsI) crystals arranged in a barrel and forward endcap, as shown in Figure 3.16. CsI was chosen as a scintillator because it has a high light yield, which provides good energy resolution, and a small Molière radius, which provides good angular resolution. Table 3.2 shows the properties of CsI as a scintillator. The EMC has complete coverage in the azimuthal angle and covers the polar angle range 15.8° – 141.8° which corresponds to a 90% coverage of the solid angle in the CM frame. There are 5,760 crystals in the barrel and these are arranged into 48 rows in θ and 120 rows in ϕ. The crystals in the forward direction of the barrel are longer, 32.4 cm (17.5 radiation lengths), than the crystals in the backward direction, which are 29.6 cm (16 radiation lengths). There are 820 crystals in the endcap and these are arranged into 8 rings in θ, 3 of which contain 120 rows in ϕ, 3 of which contain 100 rows in ϕ and 2 of which contain 80 rows in ϕ. All the endcap crystals are 32.4 cm (17.5 radiation lengths) long except for the innermost ring which is shorter by 1 radiation length due to space constraints. There is another ring inside the innermost ring which contains lead shielding to reduce the effects of background

on the endcap crystals. The crystals have a front face size of ≈ 5 cm^2 which is chosen to be comparable with the Molière radius so as to give a good angular resolution. Each crystal has two 1 cm^2 silicon pin diodes glued to the back face for photon detection. There are two diodes used to increase the reliability of the system.

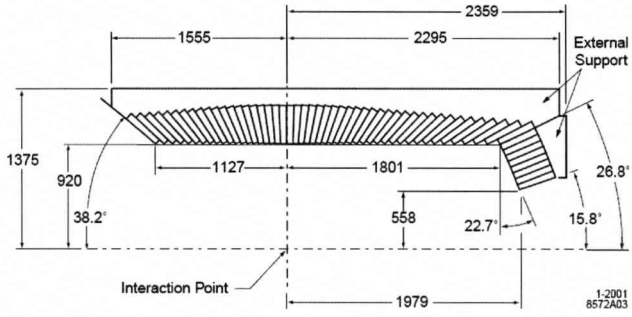

Figure 3.16: *Side on view of the calorimeter showing the top half only*

Parameter	Value
Radiation Length (cm)	1.85
Molière radius (cm)	3.8
Light Yield (γ /MeV)	50,000
Peak λ (nm)	565
Signal Decay Time (ns)	940
Radiation Hardness (rad)	$10^{3} - 10^{4}$

Table 3.2: *CsI scintillator parameters*

Figure 3.17 shows the EMC energy resolution as a function of energy for a few relevant processes.

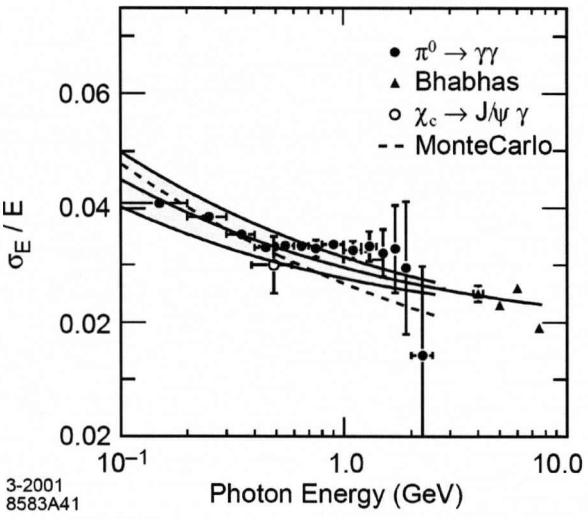

Figure 3.17: *Energy Resolution of the EMC as a function of energy, measured for photons and electrons*

3.8 The Instrumented Flux Return (IFR)

3.8.1 IFR Physics Requirements

Efficient and accurate identification of muons is essential for precise CP measurements. Many of the important CP modes contain a J/ψ which is reconstructed from its decay to e^+e^- or $\mu^+\mu^-$. Muons are also used in tagging the flavour (B or $\overline{B}$) of the non-CP B meson through semi-leptonic decays. The IFR is designed to identify muons with good efficiency and high background rejection, with a minimum momentum of 1 GeV/c. It is also required to efficiently detect neutral hadrons, especially K_L^0 identification, as the mode $B^0 \to J/\psi K_L^0$ can be used to calculate sin2β.

3.8.2 IFR Design

The IFR fulfills two roles which are to act as both a flux return for the 1.5 T magnetic field and as a support structure for the rest of the *BABAR* detector. The IFR consists of alternating layers of iron and Resistive Plate Chambers (RPCs), with the RPCs being the detecting components and the iron layers serving two purposes. They act as both the flux return for the magnetic field and also to provide discrimination between muons, which generally travel through iron layers, and hadrons, which are more readily absorbed due to hadronic showers. The detector is arranged in a hexagonal barrel with forward and backward endcaps as shown in Figure 3.18. There are 19 RPC layers in the barrel with each layer on each side split into 3 modules in the z direction. In the endcaps there are 18 layers split vertically in half with each half containing 6 modules. The thickness of iron between each layer increases from 2 cm at the inner radius to 10 cm at the outer side. In addition to these there are also two cylindrical RPC layers between the EMC and the magnet in order to detect particles leaving the EMC and to link tracks and/or EMC clusters to IFR clusters. These layers are split into 4 quarter cylinder modules.

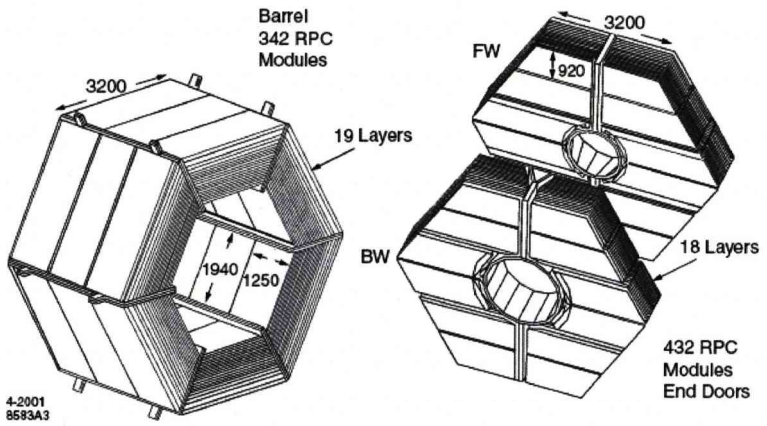

Figure 3.18: *The IFR geometry showing the barrel (Left) and the forward (FW) and backward (BW) endcaps*

Figure 3.19 shows a cross section of an RPC and the gas used is a non-flammable mixture of 57 % argon, 39 % freon-143a and 4 % isobutane. A charged particle traveling through the mixture will ionise the gas molecules, causing a trail of ions and electrons. The electrodes are 2 mm thick plates of graphite coated Bakelite, the lower of which is grounded whilst the upper electrode is connected to an 8 kV high-voltage supply. This causes an avalanche, similar to that in the DCH, in which ionised electrons cause further ionisation. Unlike the DCH, RPC's operate in "streamer" mode which means the avalanche effect becomes saturated causing vast ionisation that goes beyond being proportional to the energy loss of the incident particle. The aluminium readout strips (labeled X and Y Strips in Figure 3.19) are arranged orthogonally to give, together with the radial position of the RPC, three dimensional position information.

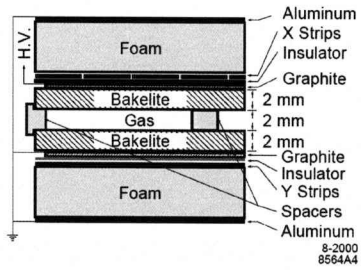

Figure 3.19: *Cross section of an RPC*

Unfortunately, the IFR performance deteriorated over time due to decreased RPC efficiencies. This prompted the decision to replace all barrel RPCs with Limited Streamer Tubes (LST) which took place in 2004–2006 and led to significant improvements in detection efficiency in the replacement segments.

Figure 3.20 shows the muon efficiency and pion misidentification probability as functions of momentum and polar angle.

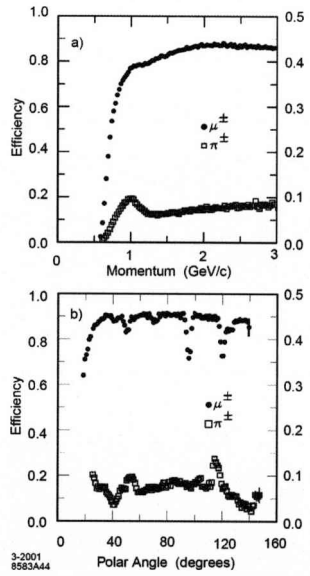

Figure 3.20: *Muon Efficiency (left scale) and pion misidentification (right scale) as a function of momentum (top) and polar angle (bottom)*

3.9 The Trigger (TRG)

The aim of the *BABAR* Trigger systems is to select interesting physics events whilst rejecting background events, such that the event rate is manageable for processing and storage. It is important that the trigger efficiency is high, stable and that it is well understood.

The Trigger consists of two levels, the Level 1 hardware trigger (L1T) that is designed to retain nearly all physics events and the level 3 Software trigger (L3T) that is designed to select physics events of interest. The design allowed for a Level 2 trigger to be introduced should it be required but it has never been implemented as the L3T had enough capacity to cope with the increased luminosities.

3.9.1 Level 1 Trigger (L1T)

The level 1 Trigger was designed to select events with a rate of around 1 kHz at design luminosity. It consists of a drift chamber trigger (DCT), a calorimeter trigger (EMT), an IFR trigger (IFT) and a global trigger (GLT). The DCT, EMT and IFT constantly receive data from their parent systems and produce trigger "primitives", which are summaries of data in terms of position and energy or momentum. These primitives are then combined by the GLT to form trigger

lines which are indicators of physical processes. If a Trigger line is active then it is sent to the Fast Control and Timing System (FCTS), which can pre-scale or mask triggers. The logic, masks and rates are not fixed and can be configured on a run by run basis. For any triggers surviving, an L1 accept (L1A) is produced and this leads to all the detector subsystems reading out their event buffers.

3.9.2 Level 3 Trigger (L3T)

The Level 3 Trigger is software based and is designed to reduce the rate produced by the Level 1 Trigger (1 kHz) to a rate of around 100 Hz. The Level 3 Trigger has all the event information available so it is able to implement more sophisticated algorithms. An attempt is made to reduce backgrounds and retain certain events which can be useful for detector calibration and monitoring. Level 3 output lines can be pre-scaled to reduced the rates of certain processes, such as Bhabha events which are required for luminosity measurements and calibrations, but aren't required at the rates at which they're produced. To allow efficiencies to be calculated, some events that are not required to pass the L1 and L3 triggers, are accepted and called "Pass Through" events. All events that pass the L3T are sent to the logging manager which writes the data to disk.

3.10 Data Acquisition Systems (DAQ)

Figure 3.21 shows a schematic diagram of the data acquisition systems (DAQ). The raw detector output is passed through the subsystem Front End Electronics (FEE) and the processed digital signals are sent over fibre optic cables to VME (Virtual Machine Environment) dataflow crates containing the dataflow Read Out Modules (ROMs). For the DCH and IFR these signals are also continuously sent to the DCT and IFT respectively. Apart from the EMC, the ROMs contain Triggered Personality Cards (TPCs) for all systems and therefore the signals are only accepted from the FEE if the FCTS issued an L1A. For the EMC, the signals are continuously received from the FEE, processed and if an L1A is issued, sent to another TPC ROM. The TPC ROMs carry out feature extraction (FEX), with subsystem dependent algorithms, to extract the signal whilst minimising backgrounds and noise. This data is then, should an L1A be present, passed to the Level 3 Trigger. Events passing the L3T are then written to temporary files before Online Prompt Reconstruction (OPR) is carried out.

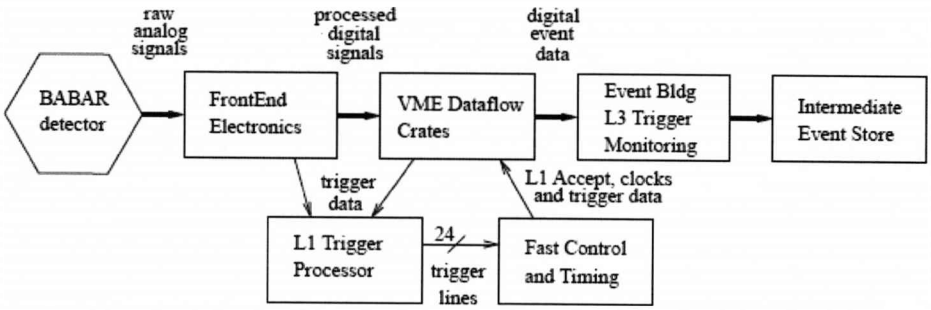

Figure 3.21: *Schematic of BABAR data acquisition system*

Chapter 4

BABAR Data

The previous chapter explained the experimental conditions of the PEP-II accelerator and *BABAR* detector and how it is used to obtain data. The process doesn't end there however, as the raw data coming off the detector is not usable and needs to go through various processes before it can be made available for the end-user to perform their analysis. This chapter outlines the process the data goes through from detector to user and describes how the quality of the data is tested.

4.1 The Path Of Data

Section 3.10 mentioned how the Data Acquisition System (DAQ) took events passing the L3 Trigger. Such events are then sent to a logging manager which writes the data to an eXtended Tagged Container (XTC) where each XTC file represents a single *run* which typically corresponds to 1 hour of data taking. At this stage there is an early quality control check in the form of the data quality manager (DQM), a role undertaken by people taking shifts in the *BABAR* control room. The DQM is responsible for assessing the quality of data coming off the detector live and for checking that the hardware is functioning properly. The DQM will then submit a flag for each run describing whether it is OK, flawed or unusable and this flag will then be used later in the process.

The XTC files are passed to the Prompt Reconstruction (PR) system which is tasked with producing calibrations and processing the incoming data by performing a complete reconstruction of events. In order to do this, the PR system has two "passes" called Prompt Calibration (PC) and Event Reconstruction (ER). The Prompt Calibration pass calculates and stores the new calibrations for each run into a database. These calibrations are then used by the Event Reconstruction pass which fully reconstructs the events and writes them to the event store database. The two passes are performed by farms of CPUs including a dedicated

server that runs a Logging Manager (LM). The LM is responsible for taking the events from the XTC files and distributing them to the reconstruction processes running on the nodes of the farm. The PC farm must process runs in sequential order whereas the ER farms can process any runs from the PC pass. Figure 4.1 shows a detailed view of the farm control systems and these are discussed in more detail in [48].

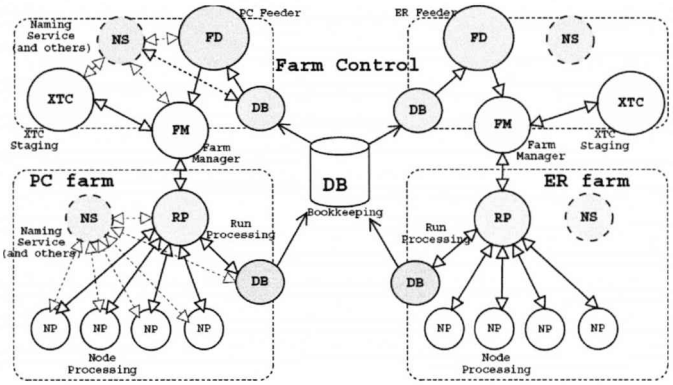

Figure 4.1: *The deployment of the control systems of the PR farms*

In the process of both the Prompt Calibration and Event Reconstruction there are files which are stored containing information that can be used for quality assurance (QA files). After the processing the data contained in a number of collections per run is merged into one collection. These are then written out in three streams (collections) called AllEvents, TriggerStream and BackgroundEvents.

The AllEvents data set is the most general one available, but often for an analysis only a subset is required of the total data produced. In order to do that, an application is used to *skim* the data and label each event with a set of tags, producing

an AllEventsSkim data set. These tags give information on the characteristics of the event such as whether it contains a particular decay. Analysis groups can then create their own skims whereby they use those tags to select data from the AllEventsSkim to produce their own dataset containing only events that may be of relevance to a particular analysis.

4.2 Quality Control

An important task in processing the data is to test the quality of it so as to make sure the detector is functioning correctly and that the data is of necessary standard. In order to make sure the data is accurate and of good quality, it is important to make checks on a regular basis.

4.2.1 The Data Quality Group

The Data Quality Group (DQG) at *BABAR* is a group set up to monitor the data produced and check that it is suitable for use, keeping any good data and removing any bad. In order to do this a list is created, on a weekly basis, of all processings that have been classified as "done" by PR that week. The Run Quality Manager (RQM) will then use that list to create stripcharts from the

QA files corresponding to those runs. The stripcharts are plots of specific physics quantities against a suitable run range.

The stripcharts are categorized corresponding to the various subsystems of the detector and the quantities are chosen so as to probe the effectiveness of the detector and reconstruction. The Data Quality Group has an expert for each subsystem and they are responsible for monitoring the stripcharts and deciding on whether the data is acceptable or not. That subsystem expert will then mark the processing as being good, flawed or bad. Good corresponds to the data being acceptable, flawed means that this processing shouldn't be used at the moment but may be OK and bad means that the data is never going to be usable. The RQM will then make a global decision on the state of the run. Every night the DQG flags are checked and the PR collections are labeled accordingly. In order to get significant physics it is important to maximise the statistics and the amount of data available to the end-user. It is therefore important not to waste events and so data that was deemed not good enough will often be reprocessed and go through the DQG checks again. Due to improvements in reconstruction all data has been reprocessed, leading to a standardised data-set.

4.2.2 Data Quality Tools

In order to test the quality of the data produced it is important to have the right tools in place to produce the necessary results to be checked. As part of the research, the specific role undertaken in the DQG has been as the Data Quality Group Tools Expert. This required being responsible for the tools used by the DQG over the last three years and involved overseeing a number of packages such as RqmootTreeTools, OprQaUtils and DqmJas. RqmRootTreeTools is the main package used to provide the weekly stripcharts used by the DQG or for any ad-hoc uses. It takes the processed files from ER and PC and extracts information to produce files or stripcharts containing relevant physics quantities for testing. Figure 4.2 shows stripcharts produced by RqmRootTreeTools for the SVT.

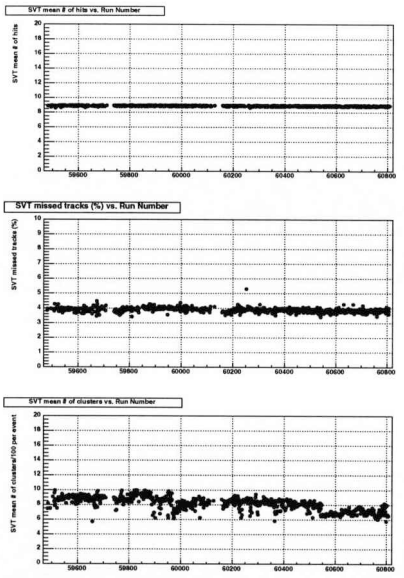

Figure 4.2: *Example stripcharts showing the number of hits (top plot), missed tracks (middle plot) and clusters (bottom plot) in the SVT over a range of runs*

OprQaUtils is a package designed to manipulate the QA files produced by the Prompt Reconstruction. It can then be used to manage or merge the QA files, produce stripcharts for monitoring and is also used create an updatable web page that allows the operator to browse and search for runs. DqmJas is a package for run quality monitoring using Java Analysis Studio (JAS). DqmJas uses as input information the histograms produced in PR and the stripcharts produced by RqmRootTreeTools. Figure 4.3 shows a screenshot of the DqmJas output displaying information on the DCH. It then allows the user to look over and monitor the various physics quantities involved in a user friendly manner. In order to oversee these packages it has been necessary to add new sections to the code, fix any compatibility issues or problems that arise and liaise with other members of the group to make improvements.

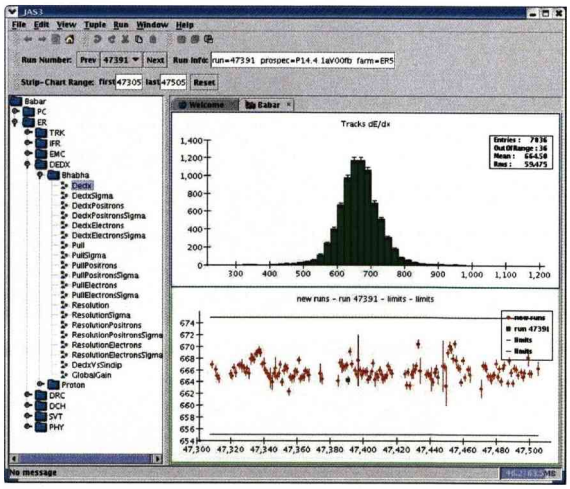

Figure 4.3: *View of DqmJas showing the dE/dx distribution in the DCH for a particular run (top plot) and the mean dE/dx over a run range (bottom plot)*

4.3 Reconstruction

Section 4.1 described the first stage of the reconstruction process, however there is also a second reconstruction process the data needs to go through. This second process combines the output from the OPR stages to form particle candidates from their decay products. This is achieved by using several analysis packages based on the common *BABAR* framework.

4.3.1 Tracking

Charged Tracks

In order to reconstruct tracks there are specific routines and these use data from the Level 3 Trigger, the SVT and the DCH. Charged tracks are described by five quantities defined at the point of closest approach (POCA) of the track to the z-axis:

- d_0- the distance in the x-y plane to the z-axis.
- ϕ_0- the azimuthal angle of the track.
- $\omega = 1/P_T-$ the track curvature.
- z_0- the distance in the z direction to the co-ordinate system origin.

- $tan\lambda$– the tangent of the track's dip angle with respect to the x-y plane.

A Kalman fitting technique [49] is applied to hits that make up the L3 tracks and the technique accounts for detector material distribution and local magnetic field variations. Additional DCH hits consistent with the tracks are then added and the fit is re-applied with the resulting tracks used to estimate the collision time. The collision time is important for rejecting out of time hits in the SVT and for precision on the track hits in the DCH, since the position of a hit within any given cell is related to the drift time. The other DCH hits that are inconsistent are then used to search for tracks that do not originate from the IP or those that do not span the whole chamber.

All tracks found in the DCH are then extrapolated into the SVT, accounting for material and magnetic fields, whilst consistent SVT hits are added. SVT hits that are not consistent with DCH tracks are then subjected to a further track finding algorithm in order to identify SVT-only tracks which fail to reach the DCH due to having low momentum or scattering by the SVT support structure.

The tracks are placed into *lists* in the event store depending on the quality of the track. The track list used in the analysis contained within this thesis is the *GoodTracksVeryLoose* list which has the following requirements:

- A maximum momentum of 10.0 GeV/c.

- At least 1 hit in the DCH.
- $d_0 < 1.5$ cm.
- $z_0 < 10$ cm.

Neutral Particles

In addition to the charged tracks described above, there are algorithms used to reconstruct neutral particles using information from the EMC. The EMC reconstruction algorithms combine individual crystals into clusters, where clusters correspond to individual particle showers. This begins by identifying crystals with energy greater than 10 MeV. Any neighbouring crystals with energies greater than 1 MeV, or those that neighbour a crystal included in the cluster with an energy greater than 3 MeV, are included. This process continues until there are no further crystals that fulfill those requirements.

The established cluster will then be subjected to a "bump" finding algorithm which runs over all the crystals contained within that cluster. The algorithm searches for local maxima within the cluster as a single cluster may be caused by two or more showers. Charged tracks are also projected onto the inner face of the EMC and an attempt is made to associate each track with a bump. Those bumps that are associated with tracks are accounted for in the subsequent reconstruction

code. Those bumps that are not associated with tracks are assumed to be neutral particles and are placed into a list analogous to those used for tracks called *GoodPhotonLoose*.

4.3.2 Particle Identification (PID)

The next stage in the reconstruction process is particle identification. There are five types of charged particles that may be detected as a track by the *BABAR* detector and these are pions, kaons, electrons, muons and protons. PID uses data from each of the subsystems and combines them to form particle selectors. Each selector uses probability density functions (PDFs) to form a per-track likelihood for the particle track it is designed to select. There is no specific selector for pions but if a track fails the other selectors it is assumed to be a pion.

The kaon selectors make use of the Cerenkov angle and number of photons measured by the DIRC along with the dE/dx information from the SVT and DCH. The Cherenkov angle is used by comparing the measured angle with the expected angle for the given particle type and track momentum. The difference between the two is divided by the experimental errors to give a "pull". The distribution of this pull is a Gaussian and the PDF is calculated using control samples. For low momentum tracks, which are near the Cerenkov emission threshold, there will be

a much smaller amount of photons emitted, making it hard to get a good measurement of the Cerenkov angle. Instead, only the number of measured photons is used to form the likelihood which follows a Poisson distribution. The dE/dx PDF's are also derived from Gaussian pull distributions and the expected values are modeled by Bethe-Bloch functions, with the pull distributions coming from data control samples.

The idea of a likelihood selector, such as the "KLH" selectors used in this analysis, is to calculate a likelihood for each particle hypothesis. The LH selector combines the likelihoods from the DIRC, DCH and SVT. The DCH and SVT likelihoods are calculated by comparing the measured dE/dx with the expected dE/dx from the Bethe-Block parameterisation. The DCH likelihood is calculated based on a Gaussian PDF and the SVT likelihood is calculated based on a bifurcated Gaussian PDF. The DIRC likelihood can not be used in this way, due to significant tails on the fitted Cerenkov angle, and so a new likelihood is constructed from the Cerenkov angle, number of photons and track quality. There are a number of selectors (NotPion, VeryLoose, Loose, Tight or VeryTight) which are defined by how *tight* they are where the tightness corresponds to the values of the cuts they must satisfy. The KLHNotPion selector used in the analysis contained within this thesis requires that $\mathcal{L}_K/(\mathcal{L}_K + \mathcal{L}_\pi) > 0.2$, whilst the KLHTight selector requires that $\mathcal{L}_K/(\mathcal{L}_K + \mathcal{L}_\pi) > 0.9$ and $\mathcal{L}_K/(\mathcal{L}_K + \mathcal{L}_p) > 0.2$.

The tightness of the selector has an effect on the selection efficiency and purity, with tighter cuts lowering the efficiency but increasing the purity. Figures 4.4, 4.5 and 4.6 show the efficiencies of the Kaon NotAPion, Kaon Tight and Electron selectors as a function of momentum, for different polar angles.

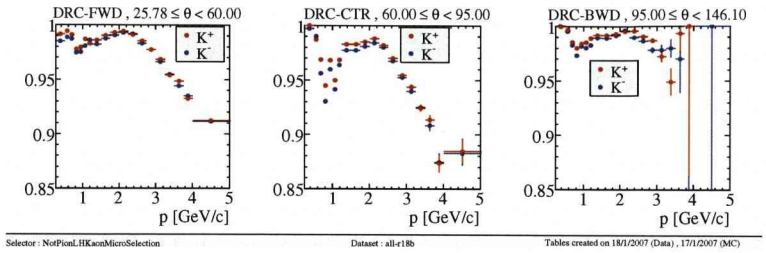

Figure 4.4: *Efficiency of the KLHNotPion selector as a function of momentum, for different polar angles*

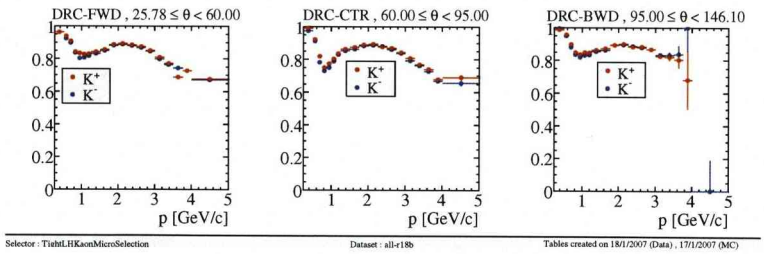

Figure 4.5: *Efficiency of the KLHTight selector as a function of momentum, for different polar angles*

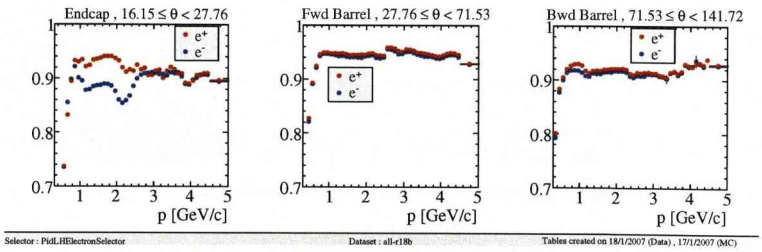

Figure 4.6: *Efficiency of the electron LH selector as a function of momentum, for different polar angles*

4.3.3 Vertexing

Composite candidates are particles that cannot be detected directly by *BABAR* but have to be reconstructed from their decay products. There are a number of composite particles of interest in this analysis, such as the D and B mesons. There is more than one *BABAR* vertex fitting routine although the one called *TreeFitter* is primarily used in the analysis contained within this thesis. TreeFitter is able to fit a complete decay chain at once by using the reconstructed tracks, clusters and PID along with a hypothesis for the decay chain. It uses a Kalman fitter for χ^2 minimisation to find the vertex.

It is also possible to place constraints on the fits such as the mass of the composite candidate. In that case the set of tracks is required to have the invariant mass equal to that of the composite particle. The constrained fit has the advantage that it improves resolution and is important when the daughters of the composite particle have width smaller than the detector resolution. The constrained particle lists are then used to form composite particles as you build the decay tree. However it is also necessary to perform an unconstrained fit and these are used so that it is possible to use the unconstrained kinematic variables, such as mass, in distinguishing between background and signal.

4.4 Monte-Carlo Simulation

Interpretation of the large amounts of data recorded by the *BABAR* detector is made possible by the use of Monte-Carlo (MC) simulated data. This simulated data is the result of full detector simulation followed by the application of the same reconstruction routines as applied to the actual data. The simulation can be broken down into three main parts:

- Generation of the event
- Simulation of the passage of the particles through the detectors and the response to the detector material
- Response of the detector electronics, including the trigger system

The first stage is handled by the *EvtGen* package which simulates the decays of B mesons and other particles. This allows for effects such as CP violation and interference to be included. A package called *Jetset* is used to generate continuum events as well as some B events that *EvtGen* doesn't implement.

The simulation of the detector is carried out by *BABAR* code based on the *GEANT4* package. This includes a detailed model of the *BABAR* detector including the geometry and materials used. The behaviour of the particles as they travel through

the detector material is included including how they trigger the actual detector systems. All this information is stored in an object called a "gHit" which contains the information on the interaction with the detector.

The third stage is a full software implementation of the *BABAR* electronics, simulating the processing of detector signals through the front end electronics and the dataflow crates to the data acquisition system. It also includes a software simulation of the trigger system which determines when an event would be triggered on and stored.

Also present in real data are machine backgrounds and electronic noise. During data taking, cyclic triggers are issued, about once every second, causing the DAQ system to read out its event buffers. The data written from these triggers represent a good sample of the background conditions in the detector. These events are stored and overlaid with simulated data to form the full data simulation.

The reconstruction for simulated data is almost identical for that of data. One exception is that truth information is stored for Monte-Carlo as this can be used to estimate the misreconstruction effects for data.

4.5 Fitting Tools

Minuit [50] is the dedicated fitting package used to maximise user-defined likelihood functions for the analysis contained within this thesis. *Minuit's MIGRAD* routine is used to find the function maximum and return the parameter values. *MIGRAD* also makes a first attempt at calculating parameter errors whilst the *HESSE* and *MINOS* routines perform more precise calculations.

The modelling package *RooFit* [51] provides a user interface to *Minuit* and likelihood normalisation is carried out automatically by *RooFit* before the function is passed to *Minuit*. Numerous PDF shapes are available in the *RooFit* package which can be combined by addition, multiplication or convolution to form the desired fit model.

Chapter 5

Analysis Methods

5.1 Introduction

Before discussing the analysis it is important to first describe what the objectives of the analysis are and introduce the different decay processes of interest. It is also necessary to explain how events are selected from the data collated by the *BABAR* experiment. This chapter provides details of the analysis objectives and procedures as well as outlining the processes by which events are selected.

5.2 Analysis Overview

Chapter 2 discussed the motivations behind *BABAR* and performing this analysis. This section outlines the objectives of the analysis and the procedures followed in order to achieve those objectives.

5.2.1 Analysis Objectives

The purpose of this analysis is to study the $D_{sJ}^{+}(2317)$ and $D_{sJ}^{+}(2460)$ mesons and provide results in order to determine the quantum numbers of those mesons. In order to do this the following modes for production of the D_{sJ} (and their charge conjugated modes) are considered:

- $B^{+} \to D_{sJ}^{+}(2317)\overline{D}^{(*)0}$
- $B^{+} \to D_{sJ}^{+}(2460)\overline{D}^{(*)0}$
- $B^{0} \to D_{sJ}^{+}(2317)D^{(*)-}$
- $B^{0} \to D_{sJ}^{+}(2460)D^{(*)-}$

Where $\overline{D}^{(*)0}$ and $D^{(*)-}$ refer to the fact that the B mesons decay to both the ground state and excited state D mesons. For decays of the D_{sJ} mesons the modes considered are those shown to be seen in Figure 2.4:

- $D_{sJ}^{+}(2317) \to D_s^{+}\pi^0$
- $D_{sJ}^{+}(2460) \to D_s^{+}\gamma$
- $D_{sJ}^{+}(2460) \to D_s^{*+}\pi^0$

The B decay modes are chosen as they are the most abundant and are used to calculate branching ratio measurements and to ultimately extract the D_{sJ} quantum numbers by means of an angular analysis.

5.2.2 Analysis Procedure

In order to perform the analysis D mesons are fully reconstructed in a number of decay modes shown in Table 5.1.

D Meson	Decay Modes		
D^0	$D^0 \to K^-\pi^+$	$D^0 \to K^-\pi^+\pi^-\pi^+$	$D^0 \to K^-\pi^+\pi^0$
D^+	$D^+ \to K^-\pi^+\pi^+$		
D^{*0}	$D^{*0} \to D^0\pi^0$	$D^{*0} \to D^0\gamma$	
D^{*+}	$D^{*+} \to D^0\pi^+$		
D_s^+	$D_s^+ \to \phi\pi^+$	$D_s^+ \to \overline{K}^{*0}K^+$	
D_s^{*+}	$D_s^{*+} \to D_s^+\gamma$		

Table 5.1: *The Decay modes by which the D mesons are reconstructed*

The ϕ and $\overline{K}^{*0}$ mesons are reconstructed through the $\phi \to K^+K^-$ and $\overline{K}^{*0} \to K^-\pi^+$ decays respectively. The D_s mesons are then combined with π^0 or γ to

construct D_{sJ} candidates which are in turn combined with other $D^{(*)}$ candidates to form B candidates with one B candidate per event being selected so as to reduce combinatorial backgrounds. Events which are found to be consistent with two-body decays $B \to D_s^{(*)} D^{(*)}$ are discarded from the D_{sJ} analysis but are selected separately in order to use as a control sample (See Section 6.1).

The selection is performed on the full *BABAR* data set from the runs 1-5 data taking periods, which correspond to an integrated luminosity of about 390.82 fb^{-1}. It is also performed on Monte-Carlo simulated signal and background event samples (see Section 4.4. The selection is performed in a number of stages and is described in detail in Section 5.3. Signal yields are determined from fits to the $m(D_s\gamma)$ and $m(D_s^{(*)}\pi^0)$ distributions on the data. Branching ratios are calculated from these using selection efficiencies and cross feed corrections from Monte-Carlo. Finally an angular analysis on the D_{sJ} decays is performed based on the fact that the decay $B \to DD_{sJ}$ is an $0^- \to 0^- J^P$ transition. This means that the resulting D_{sJ} is polarised and information on the D_{sJ} spin, J, can be obtained from the distribution of the helicity angle. The helicity angle, θ_h is defined as the angle between the D_{sJ} momentum in the B meson rest frame and the D_s momentum in the D_{sJ} rest frame.

There are three types of simulated data used, Signal Monte-Carlo, Two-Body signal Monte-Carlo and generic Monte-Carlo. For the signal MC, data is simulated

separately for each of the different decays modes used. This is used to determine the efficiencies of detecting these decay modes as well as the cross-feed, which is how many events are incorrectly reconstructed as a different mode. For Two-Body signal MC, data is simulated in the same way, with one set of data corresponding to each of the two-body decay modes (see Section 6.1). These are used to determine the efficiencies whilst also providing a background sample for the main analysis. The generic Monte-Carlo is simulated decays of B^+B^- and $B^0\overline{B}^0$.

5.3 Event Selection

The process used to select events is split up into three different stages. The first stage takes events from the event store and *skims* them for events that could contain the decay modes of interest to the analysis. The second stage, *pre-selection*, processes the skimmed events and imposes more demanding criteria on them whilst also calculating physical quantities that can be used in later stages. The third stage, *final selection*, further selects the final states of interest by imposing tight requirements on the events. This section will introduce these stages and give details on the constraints which are applied.

5.3.1 Skims

Section 4.1 introduced the process of *skimming* whereby the data produced by the experiment is labeled with tags describing various characteristics of the data. The data is read from the event store and is passed through a fitter algorithm which outputs into a skimmed collection. The skim collection used in this analysis is called *BToD2sD* which contains the events corresponding to the decays modes outlined above. The collection is also subject to a number of loose constraints on the reconstructed candidates which are applied during the skim. Since the pre-selection (see Section 5.3.2) either duplicates the constraints or provides harsher ones it is not worthwhile to provide a detailed list of constraints applied at skim level.

5.3.2 Pre-selection

The output from the skims is further refined by placing an number of different, more demanding criteria on the events with the output being written to *Root ntuples* [52]. An outline of the track lists and PID criteria was set out in Section 4.3.

Charged pions are selected from the GoodTracksVeryLoose list (see Section 4.3.1) and charged kaons are selected from the GoodTracksVeryLoose list and are re-

quired to satisfy the KLHNotPion PID criteria (see Section 4.3.2). π^0 candidates are built from pairs of photons taken from the neutrals list, GoodPhotonLoose (see Section 4.3.1), with Energy $E(\gamma) > 30$ MeV, LAT < 0.8, and having an invariant mass $115 < m(\gamma\gamma) < 150$ MeV/c^2. The photon lateral moment, LAT, is a dimensionless quantity and is defined [53] as:

$$LAT = \frac{\sum_{i=3}^{N} E_i r_i^2}{\sum_{i=3}^{N} E_i r_i^2 + E_1 r_0^2 + E_2 r_0^2} \tag{5.1}$$

where N is the number of crystals associated with the cluster and E_i is the energy deposited in the i-th crystal ordered from highest to lowest ($E_i > E_{i+1}$). r_0 is the average distance between the centres of neighbouring crystal faces and is approximately 5 cm as described by Section 3.7. The lateral distance r_i from the i-th crystal to the cluster centre is measured in the plane perpendicular to the line pointing from the IP to the cluster centre. In order to improve the π^0 momentum resolution a mass constrained fit is applied to the π^0 used in reconstructing the D, $D^{(*)}$ and B mesons.

D Reconstruction Cuts

D candidates are built by combining the K,π and π^0 tracks and fitting assuming a common vertex with no requirement on convergence. The D mass window for the D candidates is ± 30 MeV/c^2 around the nominal PDG [54] mass, except for the $D^0 \to K^-\pi^+\pi^0$ mode where the mass window is taken to be ± 50 MeV/c^2. A summary of the pre-selection criteria on the D candidates is shown in Table 5.2.

D modes:	$D^0 \to K\pi\pi\pi$	$D^0 \to K\pi$	$D^0 \to K\pi\pi^0$	$D^- \to K\pi\pi$
π^+ tracks	GTVL	GTVL	GTVL	GTVL
K^- PID	KLHNotPion	KLHNotPion	KLHNotPion	KLHNotPion
γ Mom. (MeV/c)	-	-	$E(\gamma) > 30$	-
γ LAT	-	-	LAT < 0.8	-
π^0 Mom. (MeV/c)	-	-	$P(\pi^0) > 0$	-
π^0 Mass (MeV/c^2)	-	-	$[115, 150]$	-
D Mass (MeV/c^2)	$m_{PDG} \pm 30$	$m_{PDG} \pm 30$	$m_{PDG} \pm 50$	$m_{PDG} \pm 30$

Table 5.2: *D pre-selection cuts. GTVL refers to the GoodTracksVeryLoose list.*

D_s^+ candidates are built by combining the K and π tracks with K^{*0} and ϕ candidates respectively. The ϕ candidates are reconstructed from K^+K^- pairs with a mass window of ± 30 MeV/c^2 around the nominal PDG mass. The K^{*0} candidates are reconstructed from $K^+\pi^-$ pairs with a mass window of ± 75 MeV/c^2 around the nominal PDG mass. A summary of the pre-selection criteria on the D_s candidates is shown in Table 5.3.

D_s^+ modes:	$D_s^+ \to K^*K$	$D_s^+ \to \Phi\pi$
π^+ tracks	GTVL	GTVL
K^+ PID	KLHNotPion	KLHNotPion
K^- PID	KLHNotPion	KLHNotPion
Φ or K^* Mass (MeV/c^2)	$m_{PDG} \pm 75$	$m_{PDG} \pm 50$
D_s^+ Mass (MeV/c^2)	$m_{PDG} \pm 30$	$m_{PDG} \pm 30$

Table 5.3: *D_s pre-selection cuts*

D^{*+} candidates are reconstructed by combining D^0 candidates, as described previously, with a charged track from the GoodTracksVeryLoose list with a momentum in the $\Upsilon(4S)$ frame of < 450 MeV/c. A cut on the $D^{*+} - D^0$ mass difference (Δm) is applied such that $|\Delta m - \Delta m_{PDG}| < 4.1$ MeV/c^2, where Δm_{PDG} is the nominal PDG difference. For modes containing $D^0 \to K^-\pi^+\pi^0$ the cut on the mass difference is increased from 4.1 MeV/c^2 to 5.1 MeV/c^2.

D^{*0} candidates are built by combining D^0 candidates, as described previously, with a photon (γ) or a π^0, as described previously. The π^0 are mass constrained and a cut $p_{CMS}(\pi^0) < 450$ MeV/c is applied on their momentum in the $\Upsilon(4S)$ frame. A cut $138 < \Delta m < 146$ MeV/c^2 is applied on the reconstructed $D^{*0} - D^0$ mass difference. The photons are taken from the neutrals list, GoodPhotonLoose, with Energy $E(\gamma) > 100$ MeV and LAT < 0.8. A cut $112 < \Delta m < 172$ MeV/c^2 is applied on the reconstructed $D^{*0} - D^0$ mass difference.

D_s^{*+} candidates are reconstructed by combining D_s^+ candidates, as described previously, with a photon from the neutrals list, GoodPhotonLoose, with Energy

$E(\gamma) > 100$ MeV and LAT < 0.8. A π^0 veto is applied to these photons which should not belong to a π^0 candidate built from two photons with $E(\gamma) > 100$ MeV, LAT < 0.8 and an invariant mass $115 < m(\gamma\gamma) < 150$ MeV/c^2. A cut $114 < \Delta m < 174$ MeV/c^2 is applied on the reconstructed $D_s^{*+} - D_s^+$ mass difference. A summary of the pre-selection criteria on the D^* candidates is shown in Table 5.4.

D^* modes:	$D^{*0} \to D^0\pi^0$	$D^{*0} \to D^0\gamma$	$D^{*+} \to D^0\pi^+$	$D_s^{*+} \to D_s^+\gamma$
π^+ tracks	-	-	GTVL	-
γ/π Mom. (MeV/c)	$p^*(\pi^0) < 450$	$p(\gamma) > 100$	$P^*(\pi^+) < 450$	$p(\gamma) > 100$
π^0 veto on γ	-	yes	-	yes
γ LAT	-	LAT< 0.8	-	LAT< 0.8
ΔM (MeV/c^2)	$[138, 146]$	$[112, 172]$	$\Delta M_{PDG} \pm 4.1$	$[114, 174]$
(if $D^0 \to K\pi\pi^0$)			$(\Delta M_{PDG} \pm 5.1)$	

Table 5.4: *D^* pre-selection cuts*

Kinematic Variables

Before reconstructing the B mesons it is important to introduce a couple of kinematic variables first. An obvious discriminating variable is the reconstructed mass of the candidate B meson

$$m_B = \sqrt{E_B^2 - \overrightarrow{p}_B^2} \tag{5.2}$$

which should be distributed, for well reconstructed B mesons, around the actual

B mass of 5.279 GeV. However, since B candidates are generally reconstructed from many tracks and neutral clusters they suffer from the detector resolution on each one. The overall effect is large and causes the B mass distribution to become very wide ($\sim$ 25 MeV). Operating at the $\Upsilon(4S)$ energy, the four momenta of the B mesons are very well constrained by the beam energy, which is in turn very well measured compared with detector energy resolution. It is therefore possible to construct two, mostly uncorrelated, variables which are better constrained [55, 56]. These are the difference between the reconstructed and expected beam energy (ΔE) which is defined as:

$$\Delta E = E_B - E_X \tag{5.3}$$

and the beam-energy substituted mass (m_{ES}) which is defined as:

$$m_{ES} = \sqrt{E_X^2 - \overrightarrow{p}_B^2} \tag{5.4}$$

where $(E_B, \overrightarrow{p}_B)$ is the four momentum of the reconstructed B meson and E_X is the beam-energy constrained derived energy for the B defined as:

$$E_X = \frac{E_{beam}^2 - \overrightarrow{p}_{beam}^2 + 2\overrightarrow{p}_{beam} \cdot \overrightarrow{p}_B}{2E_{beam}} \tag{5.5}$$

where $(E_{beam}, \overrightarrow{p}_{beam})$ is the four momentum of the beams and these quantities are all defined in the laboratory frame. Since m_{ES} is only calculated from the beam four-momentum and the momentum of the B candidate it is independent of the mass hypothesis for the B daughter tracks. ΔE however does depend on it as it uses the reconstructed energy of the B candidate. For well constructed B mesons m_{ES} should peak at the B mass, 5.279 GeV, and ΔE should peak at zero. Figure 5.1 shows examples of ΔE and m_{ES} plots.

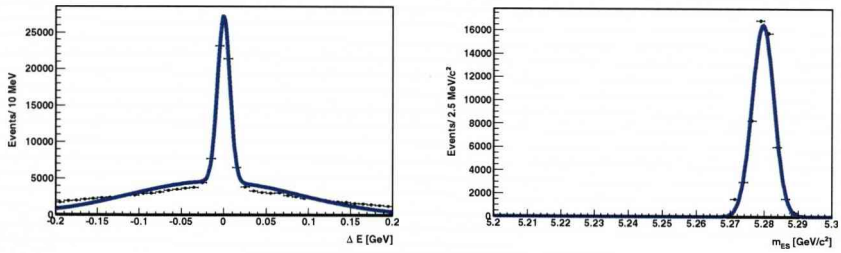

Figure 5.1: *Example ΔE (left) and m_{ES} (right) spectra from signal Monte-Carlo*

B Reconstruction Cuts

The $D^{(*)}$ and $D_s^{(*)}$ candidates, as defined previously, are combined with π^0 or γ in a series of B reconstructions to form each of the 12 final states. Neutral pions from B are built from pairs of photons taken from the neutrals list, GoodPho-

tonLoose, with Energy $E(\gamma) > 30$ MeV, LAT < 0.8, having an invariant mass $115 < m(\gamma\gamma) < 150$ MeV/c^2 and with no π^0 momentum or energy requirement. Photons from B are selected from the neutrals list, GoodPhotonLoose, with Energy $E(\gamma) > 100$ MeV, LAT < 0.8 and with a π^0 veto. Cuts of $5.15 < m_{ES} > 5.35$ GeV/c^2 and $-0.3 < \Delta E > 0.3$ are applied to the reconstructed B candidates. A summary of the pre-selection criteria on the B candidates is shown in Table 5.5.

B modes:	All Modes
Mass (GeV/c^2)	$5.0 < M > 5.5$
ΔE (GeV)	$-0.3 < \Delta E > 0.3$
M_{es} (GeV/c^2)	$5.15 < m_{ES} > 5.35$

Table 5.5: *B pre-selection cuts*

5.3.3 D Reconstruction

It is important to investigate the inclusive mass spectra for all of the D mesons present in the events from pre-selection to determine which final selection cuts to make on the D mass. Figure 5.2 shows the inclusive mass spectra for data and Figure 5.3 shows the inclusive mass spectra for signal Monte-Carlo. It should be noted that unless explicitly mentioned, all following plots include both combinatorial background and the effect of cross feed between different $B \to D_{sJ}\overline{D}^{(*)}$ modes. The inclusive mass spectra are fitted by the sum of a polynomial background and Gaussian signal.

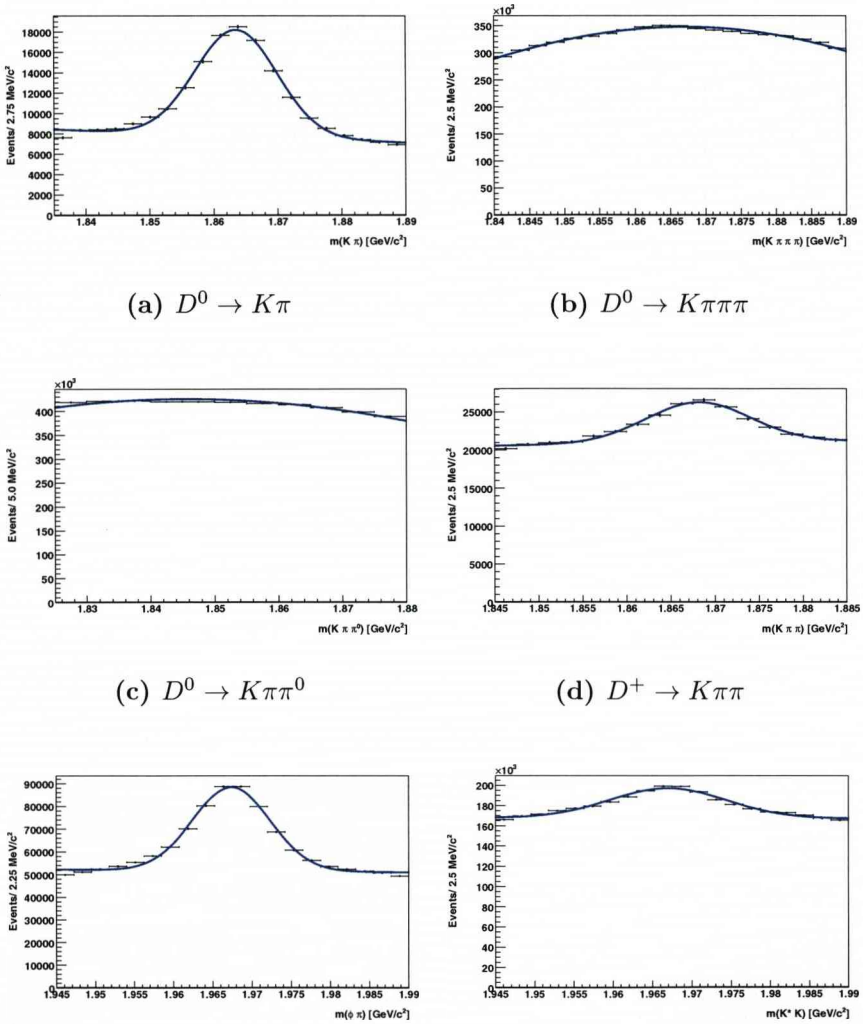

(a) $D^0 \to K\pi$ (b) $D^0 \to K\pi\pi\pi$

(c) $D^0 \to K\pi\pi^0$ (d) $D^+ \to K\pi\pi$

(e) $D_s^+ \to \phi\pi$ (f) $D_s^+ \to K^*K$

Figure 5.2: *D Reconstruction Mass Plots for data*

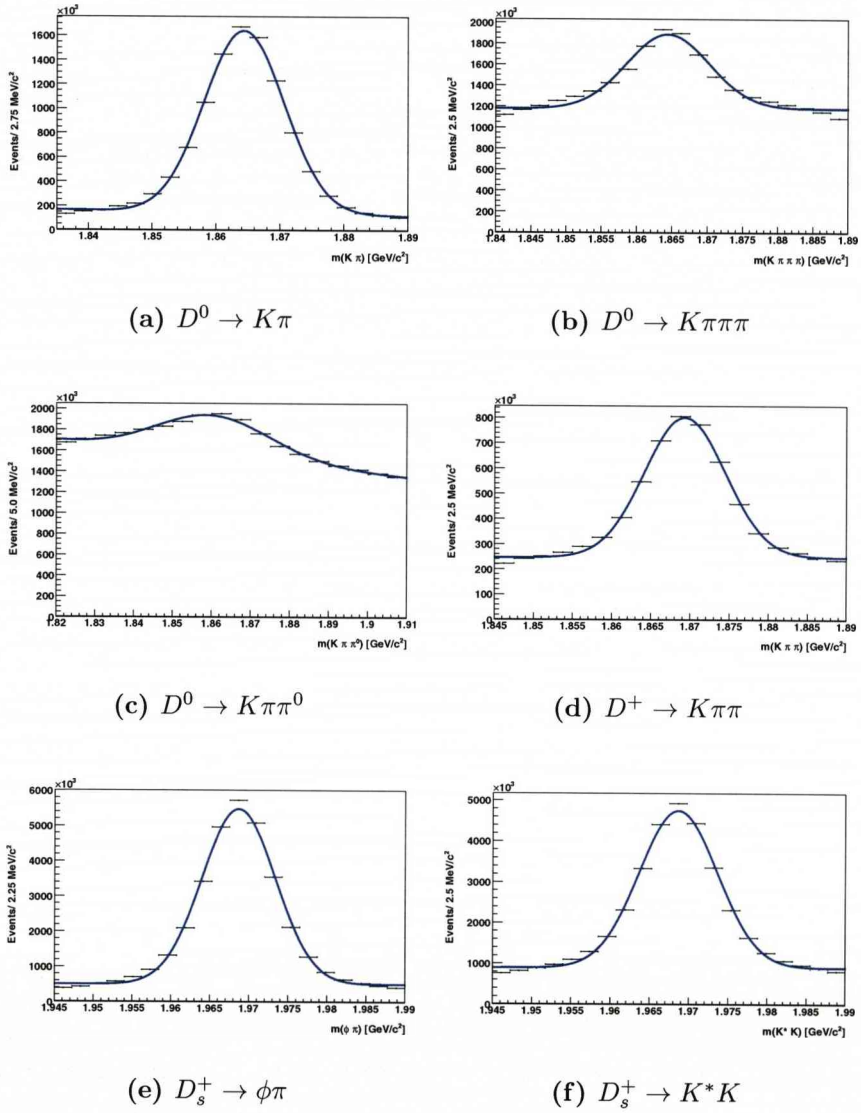

(a) $D^0 \to K\pi$ (b) $D^0 \to K\pi\pi\pi$

(c) $D^0 \to K\pi\pi^0$ (d) $D^+ \to K\pi\pi$

(e) $D_s^+ \to \phi\pi$ (f) $D_s^+ \to K^*K$

Figure 5.3: *D Reconstruction Mass Plots for signal Monte-Carlo*

It is found that for modes $D^0 \to K\pi$, $D^+ \to K\pi\pi$, $D_s^+ \to \phi\pi$ and $D_s^+ \to K^*K$ clear mass peaks are present in both data and signal Monte-Carlo. For modes $D^0 \to K\pi\pi^0$ and $D_0 \to K\pi\pi\pi$ peaks are observed in the signal Monte-Carlo

but are unclear in the data. Figure 5.4 shows the inclusive mass spectra for both signal Monte-Carlo and generic Monte-Carlo. It can be seen that for the $D^0 \to K\pi\pi^0$ and $D_0 \to K\pi\pi\pi$ modes there are more D mesons reconstructed in the generic Monte-Carlo. The reason for this is due to larger combinatorial backgrounds in those decay modes which gives rise to the poor signal peaks in data.

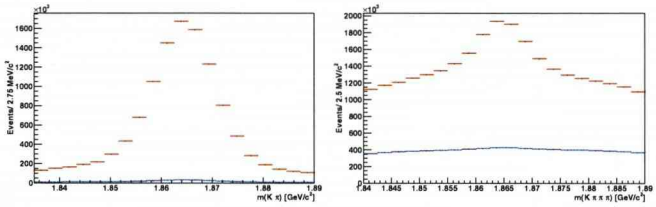

(a) $D^0 \to K\pi$ (b) $D^0 \to K\pi\pi\pi$

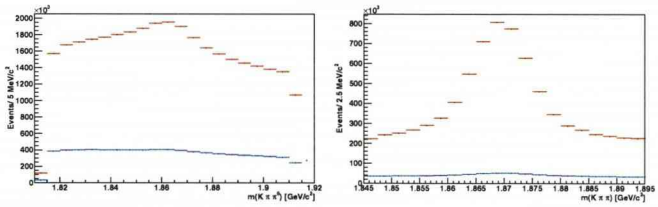

(c) $D^0 \to K\pi\pi^0$ (d) $D^+ \to K\pi\pi$

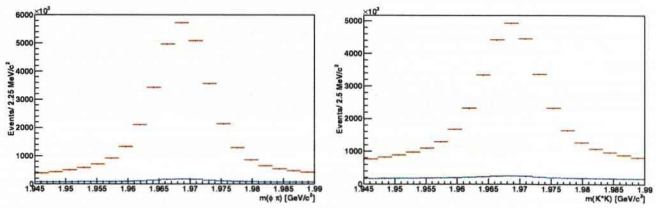

(e) $D_s^+ \to \phi\pi$ (f) $D_s^+ \to K^*K$

Figure 5.4: *D Reconstruction Mass Plots for signal Monte-Carlo (red points) and generic Monte-Carlo (blue points)*

Decay modes	Mass (Data)	σ_m (Data)	Mass (MC)	σ_m (MC)	Mass (PDG)	Systematic (%)
$D^0 \to K^+\pi^-$	1863.5 ± 0.05	6.37 ± 0.06	$1864.4 \pm 0.00^*$	$6.26 \pm 0.00^*$		1
$D^0 \to K^+\pi^-\pi^0$	1845.7 ± 0.22	71.38 ± 0.71	1860.4 ± 0.04	14.60 ± 0.06	1864.84	90
$D^0 \to K^+\pi^-\pi^+\pi^-$	1866.9 ± 0.05	44.09 ± 0.18	$1864.4 \pm 0.00^*$	5.84 ± 0.01		85
$D^+ \to K^+\pi^-\pi^+$	1868.1 ± 0.20	5.93 ± 0.29	$1869.3 \pm 0.00^*$	$5.18 \pm 0.00^*$	1869.62	9
$D_s^+ \to \phi\pi^+$	1967.4 ± 0.03	4.93 ± 0.03	1968.6 ± 0.01	4.60 ± 0.01	1968.49	3
$D_s^+ \to K^*K^+$	1967.0 ± 0.10	7.40 ± 0.14	$1968.6 \pm 0.00^*$	$4.70 \pm 0.00^*$		24

Table 5.6: *Reconstructed D masses and resolution in data and signal Monte-Carlo.* **Errors given as 0.00 are very small due to large statistics*

Table 5.6 shows the average reconstructed D and D_s masses along with their width for both data and signal Monte-Carlo. For some modes the width in data is substantially larger than that for Monte-Carlo and this will lead to a difference in reconstruction efficiency. To obtain a systematic error on the efficiency, the widths are shifted and the difference in signal size is calculated. Table 5.6 also shows the systematic errors, calculated as a percentage, on the different sub-modes.

For the final selection the following cuts are applied to the D^0, D^+ and D_s^+ masses:

- $D^0 \to K^-\pi^+$
  - $m = m_{RECO} \pm 3\sigma$

- $D^0 \to K^-\pi^+\pi^0$
  - $m = m_{RECO} \pm 2.5\sigma$
- $D^0 \to K^-\pi^+\pi^-\pi^+$
  - $m = m_{RECO} \pm 2.5\sigma$
- $D^+ \to K^-\pi^+\pi^+$
  - $m = m_{RECO} \pm 3\sigma$
- $D_s^+ \to \phi\pi^+$
  - $m = m_{RECO} \pm 3\sigma$
- $D_s^+ \to K^*K^+$
  - $m = m_{RECO} \pm 2.5\sigma$

Where m is the reconstructed mass in a given event, m_{RECO} is the reconstructed mass from Monte-Carlo and σ is the width of the reconstructed mass spectrum from Monte-Carlo. The D^* and D_s^* reconstruction are studied in the same way and Figure 5.5 shows plots of the $D^* - D$ mass for data and Figure 5.6 shows plots of the $D^* - D$ mass for signal Monte-Carlo.

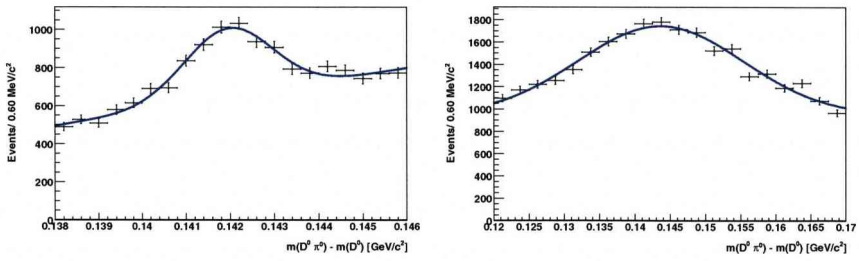

(a) $D^{*0} \to D^0\pi^0$ (b) $D^{*0} \to D^0\gamma$

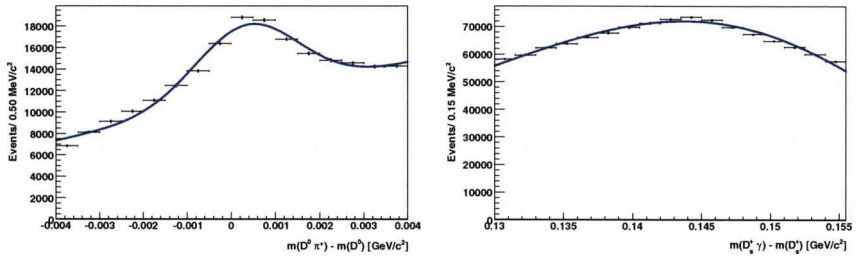

(c) $D^{*+} \to D^0\pi^+$ (d) $D_s^{*+} \to D_s^+\gamma$

Figure 5.5: *$D^* - D$ Reconstruction Mass Plots for data*

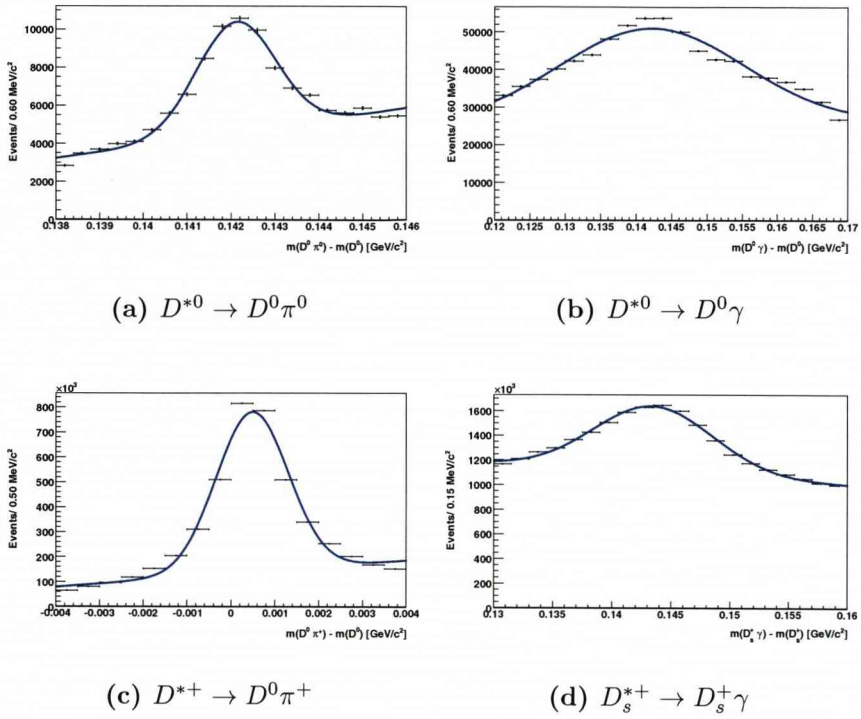

(a) $D^{*0} \to D^0\pi^0$ (b) $D^{*0} \to D^0\gamma$

(c) $D^{*+} \to D^0\pi^+$ (d) $D_s^{*+} \to D_s^+\gamma$

Figure 5.6: *$D^* - D$ Reconstructed Mass difference for signal Monte-Carlo*

Decay modes	Δm (Data)	$\sigma_{\Delta m}$ (Data)	Δm (MC)	$\sigma_{\Delta m}$ (MC)	Δm (PDG)	Systematic (%)
$D^{*0} \to D^0\pi^0$	141.95 ± 0.06	1.00 ± 0.07	142.11 ± 0.01	0.91 ± 0.01	142.13	7
$D^{*0} \to D^0\gamma$	143.61 ± 0.27	11.69 ± 1.11	142.09 ± 0.13	13.02 ± 0.30		15
$D^{*+} \to D^0\pi^+$	145.56 ± 0.01	2.43 ± 0.01	$145.69 \pm 0.00^*$	$1.60 \pm 0.00^*$	145.43	19
$D_s^{*+} \to D_s^+\gamma$	147.00 ± 0.74	15.97 ± 0.83	143.46 ± 0.01	5.04 ± 0.01	143.81	77

Table 5.7: *Reconstructed $\Delta M(D^* - D)$ and resolutions in data and signal Monte-Carlo. *Errors given as 0.00 are very small due to large statistics*

Table 5.7 shows the average reconstructed $D^* - D$ masses along with their width for both data and signal Monte-Carlo. For some modes the width in data is substantially larger than that for Monte-Carlo and this will lead to a difference in reconstruction efficiency. Table 5.7 also shows the systematic errors, calculated

as a percentage, on the different sub-modes.

For the final selection the following cuts are applied to the $D^* - D$ masses:

- $D^{*0} \to D^0\pi^0$
  - $140.0 < \Delta m > 144.0$ MeV/c^2
- $D^{*0} \to D^0\gamma$
  - $132.0 < \Delta m > 152.0$ MeV/c^2
- $D^{*+} \to D^0\pi^+$
  - $143.0 < \Delta m > 149.0$ MeV/c^2
- $D_s^{*+} \to D_s\gamma$
  - $133.8 < \Delta m > 153.8$ MeV/c^2

5.3.4 Final Selection

In addition to the Skim and ntuple stages a third set of selection criteria is used in order to further suppress the backgrounds. The analysis strategy for reconstructing the decays $B \to D_{sJ}^+\overline{D}^{(*)}$ is to reconstruct all the final states $\overline{D}^{(*)}D_s^+\pi^0$, $\overline{D}^{(*)}D_s^+\gamma$ and $\overline{D}^{(*)}D_s^{*+}\pi^0$. Then to select events in the B signal region and look

for a peak in the $D_s^+\pi^0$, $D_s^+\gamma$ or $D_s^{*+}\pi^0$ invariant mass spectra at the D_{sJ} mass. The final selection cuts are optimised by maximising the ratio $S/\sqrt{S+B}$ where S is the expected signal and B is the background (as discussed in Section 6.2.

D Reconstruction Cuts

The selection cuts placed on the D^0 candidates are as follows:

- Final Selection for $D^0 \to K\pi$
  - Require $K^\pm$ to satisfy the KLHNotPion PID criteria
  - Require $K^\pm$ to have a momentum $p(K) > 250$ MeV/c
- Final Selection for $D^0 \to K\pi\pi^0$

  For modes $B \to D_{sJ}D^{*+}$:
  - Require $K^\pm$ to satisfy the KLHNotPion PID criteria
  - Require $K^\pm$ to have a momentum $p(K) > 250$ MeV/c

  For all other modes :
  - Require $K^\pm$ to satisfy the KLHTight PID criteria.
  - Require $K^\pm$ to have a momentum $p(K) > 250$ MeV/c
  - Require that the $K\pi\pi^0$ vertex fit has converged and that the vertex χ^2 probability is $> 10^{-3}$

- Final Selection for $D^0 \to K\pi\pi\pi$

  For modes $B \to D_{sJ}D^{*+}$:

  - Require $K^{\pm}$ to satisfy the KLHNotPion PID criteria
  - Require $K^{\pm}$ to have a momentum $p(K) > 250$ MeV/c

  For all other modes :

  - Require $K^{\pm}$ to satisfy the KLHTight PID criteria
  - Require $K^{\pm}$ to have a momentum $p(K) > 250$ MeV/c
  - Require that the $K\pi\pi\pi$ vertex fit has converged and that the vertex χ^2 probability is $> 10^{-3}$

The selection cuts placed on the D^+ candidates are as follows:

- Final Selection for $D^+ \to K\pi\pi$

  - Require $K^{\pm}$ to satisfy the KLHNotPion PID criteria
  - Require that the $K\pi\pi$ vertex fit has converged and that the vertex χ^2 probability is $> 10^{-3}$

A summary of the final selection criteria on the D candidates is shown in Table 5.8.

D modes:	$D^0 \to K\pi$	$D^0 \to K\pi\pi^0$	$D^0 \to K3\pi$	$D^+ \to K\pi\pi$
π^+ tracks	GTVL	GTVL	GTVL	GTVL
K^- PID	KLHNotPion	KLHTight	KLHTight	KLHNotPion
(if D^0 from D^{*+})		(KLHNotPion)	(KLHNotPion)	
K^- Mom. (MeV/c)	$p(K) > 250$	$p(K) > 250$	$p(K) > 250$	-
γ Mom. (MeV/c)	-	$p(\gamma) > 30$	-	-
γ LAT	-	LAT< 0.8	-	-
π^0 energy (MeV/c)	-	$E(\pi^0) > 200$	-	-
D mass window	3σ	2.5σ	2.5σ	3σ
vertex χ^2 prob.	-	$> 10^{-3}$	$> 10^{-3}$	$> 10^{-3}$
(if D^0 from D^{*+})			(none)	

Table 5.8: *D final selection cuts*

The selection cuts placed on the D_s^+ candidates are as follows:

- Final Selection for $D_s^+ \to \phi\pi$

  For modes $B \to D_{sJ}D^{*+}$:

  For modes $\overline{D}^0 \to K^+\pi^-$:

  - Require $K^\pm$ to satisfy the KLHNotPion PID criteria
  - Cut on the ϕ mass, $1005 < m(K^+K^-) < 1035$ MeV/c^2

  For modes $\overline{D}^0 \to K^+\pi^-\pi^0$ and $\overline{D}^0 \to K^+\pi^-\pi^+\pi^-$:

  - Require $K^\pm$ to satisfy the KLHNotPion PID criteria
  - Cut on the ϕ mass, $1005 < m(K^+K^-) < 1035$ MeV/c^2
  - Cut on the ϕ helicity angle $|cos(\theta_h)| > 0.3$

  For other modes :

  For modes $\overline{D}^0 \to K^+\pi^-$ and $\overline{D}^- \to K^+\pi^-\pi^-$:

- Require $K^{\pm}$ to satisfy the KLHNotPion PID criteria
- Cut on the ϕ mass, $1005 < m(K^+K^-) < 1035$ MeV/c^2
- Cut on the ϕ helicity angle $|cos(\theta_h)| > 0.3$

For modes $\overline{D}^0 \to K^+\pi^-\pi^0$ and $\overline{D}^0 \to K^+\pi^-\pi^+\pi^-$:

- Require that at least one K satisfies the KLHTight PID criteria
- Cut on the ϕ mass, $1005 < m(K^+K^-) < 1035$ MeV/c^2
- Cut on the ϕ helicity angle $|cos(\theta_h)| > 0.3$

- Final Selection for $D_s^+ \to K^{*0}K$

For modes containing $\overline{D}^0 \to K^+\pi^-$:

- Require that at least one K satisfies the KLHTight PID criteria
- Cut on the K^{*0} helicity angle $|cos(\theta_h)| > 0.3$
- Cut on the K^{*0} mass, $821 < m(K^-\pi^+) < 971$ MeV/c^2

For all other modes :

- Require that at least one K satisfies the KLHTight PID criteria
- Cut on the K^{*0} helicity angle $|cos(\theta_h)| > 0.3$
- Cut on the K^{*0} mass, $821 < m(K^-\pi^+) < 971$ MeV/c^2
- Require that the $K^{*0}K^+$ vertex fit has converged and that the vertex χ^2 probability is $> 10^{-3}$

A summary of the final selection criteria on the D_s candidates is shown in Table 5.9.

D_s modes:	$D_s^+ \to \phi\pi^+$	$D_s^+ \to K^{*0}K^+$
π^+ tracks	GTVL	GTVL
$K^\pm$ PID	≥ 1 KLHTight	≥ 1 KLHTight
(In decays with D^{*+})	(2 KLHNotPion)	
ϕ or K^{*0} mass cut (MeV/c^2)	$m_{PDG} \pm 15$	$m_{PDG} \pm 75$
Helicity	$\lvert cos(\theta_h)\rvert > 0.3$	$\lvert cos(\theta_h)\rvert > 0.3$
(In decays with D^{*+} where $D^0 \to K^+\pi^-$)	(none)	
vertex χ^2 prob.		$> 10^{-3}$
(In decays with $D^0 \to K^+\pi^-$)		(none)
D_s mass window	3σ	2.5σ

Table 5.9: *D_s final selection cuts*

Aside from the new cuts on the $D^{*0} - D^0$ mass differences, the final selection cuts placed on the D^{*0} are the same as those used in the pre-selection stage and are as follows:

- Final Selection for $D^{*0} \to D^0\pi^0$
  - Require π^0 to have a momentum in $\Upsilon(4S)$ frame of $p^*(\pi^0) < 450$ MeV/c
- Final Selection for $D^{*0} \to D^0\gamma$
  - Cut on the photon momentum, $p(\gamma) > 100$ MeV/c
  - Cut on the photon lateral moment, $LAT < 0.8$

- Require Photon to have passed π^0 veto whereby the photon shouldn't belong to a π^0 candidate built from two photons with $E(\gamma) > 100$ MeV, LAT < 0.8 and having an invariant mass of $115 < m(\gamma\gamma) < 150$

Aside from the new cut on the $D^{*+} - D^0$ mass difference, the final selection cuts placed on the D^{*+} are the same as those used in the pre-selection stage and are as follows:

- Final Selection for $D^{*+} \to D^0\pi^+$
  - Require π^+ to have a momentum in $\Upsilon(4S)$ frame of $p^*(\pi^+) < 450$ MeV/c

Aside from the new cut on the $D_s^{*+} - D_s^+$ mass difference, the final selection cuts placed on the D_s^{*+} are the same as those used in the pre-selection stage and are as follows:

- Final Selection for $D_s^{*+} \to D_s^+\gamma$
  - Cut on the photon momentum, $p(\gamma) > 100$ MeV/c
  - Cut on the photon lateral moment, $LAT < 0.8$
  - Require Photon to have passed π^0 veto whereby the photon shouldn't belong to a π^0 candidate built from two photons with $E(\gamma) > 100$

MeV, LAT < 0.8 and with an invariant mass of $115 < m(\gamma\gamma) < 150$ MeV/c^2

A summary of the final selection criteria on the D^* candidates is shown in Table 5.10.

D^* modes:	$D^{*+} \to D^0\pi^+$	$D^{*0} \to D^0\pi^0$	$D^{*0} \to D^0\gamma$	$D_s^{*+} \to D_s^+\gamma$
π^+ tracks	GTVL	-	-	-
γ/π Mom. (MeV/c)	$p^*(\pi^+) < 450$	$p^*(\pi^0) < 450$	$p(\gamma) > 100$	$p(\gamma) > 100$
π^0 veto on γ	-	-	yes	yes
γ LAT	-	-	LAT< 0.8	LAT< 0.8
Δm (MeV/c^2)	[143.4, 145.4]	[140.0, 144.0]	[132.0, 152.0]	[133.8, 153.8]

Table 5.10: *D^* final selection cuts*

5.3.5 B Reconstruction

Definition of the Signal Region in the ΔE, m_{ES} Plane

As described in Section 5.3.2, the $D_s^{(*)+}$ and $D^{(*)}$ candidates are combined with photons (γ) and neutral pions (π^0) for form B candidates. The D_{sJ} signal is extracted from the $D_s^{(*)+}\pi^0$ and $D_s^+\gamma$ mass distributions of events in the m_{ES}, ΔE signal region. Alternatively it is possible to select D_{sJ} signal by cutting on m_{ES} and the $D_s^{(*)+}\pi^0$ or $D_s^+\gamma$ mass and investigating the ΔE spectra for events inside or outside of the signal region.

The m_{ES} signal region is independent of the decay mode being considered and so

a cut, $5.27 < m_{ES} < 5.29$ GeV/c^2, is applied to all events:

The ΔE resolution however depends on the final states. Figure 5.7 shows the ΔE spectra with the final selection and m_{ES} cut described above for $D_s^+\overline{D}^{(*)}\pi^0$ final states (a), $D_s^{*+}\overline{D}^{(*)}\pi^0$ final states (b), and $D_s^+\overline{D}^{(*)}\gamma$ final states (c). The spectra are from signal Monte-Carlo and are fitted with the sum of a first order polynomial background and Gaussian signal.

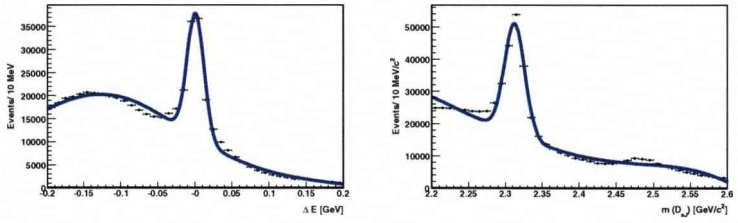

(a) $B \to D_s^+ D^{(*)}\pi^0$

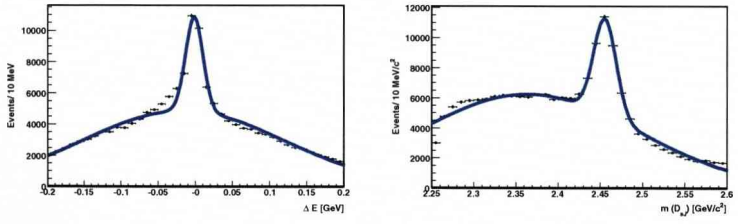

(b) $B \to D_s^{*+} D^{(*)}\pi^0$

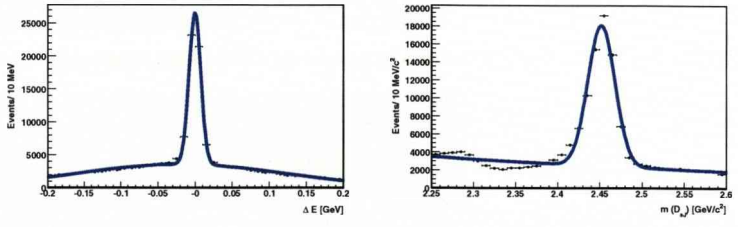

(c) $B \to D_s^+ D^{(*)}\gamma$

Figure 5.7: *ΔE and $m(D_{sJ})$ spectra for final states using signal Monte-Carlo*

The peaks in the ΔE spectra correspond to the $B \to D_s^+ D^{(*)}\pi^0$, $B \to D_s^{*+} D^{(*)}\pi^0$ and $B \to D_s^+ D^{(*)}\gamma$ signals. The resolutions fitted are shown in Table 5.11. No truth matching is included and the spectra include both combinatorial background and the effect of cross feed between different $B \to D_{sJ}\overline{D}^{(*)}$ modes.

Modes:	ΔE (MeV)	$\sigma_{\Delta E}$	m(D_{sJ}) (MeV/c^2)	σ_m
$B \to D_{s0}^+ \overline{D}^{(*)}(D_{s0} \to D_s^+\pi^0)$	0.58	11.36	2312.4	13.81
$B \to D_{s1}^+ \overline{D}^{(*)}(D_{s1} \to D_s^{*+}\pi^0)$	-1.83	11.71	2455.3	13.32
$B \to D_{s1}^+ \overline{D}^{(*)}(D_{s1} \to D_s^+\gamma)$	-0.61	7.89	2451.8	15.99

Table 5.11: *ΔE and $m(D_{sJ})$ resolutions for signal Monte-Carlo*

ΔE distributions for the $D_s^+\pi^0$, $D_s^+\gamma$ and $D_s^{*+}\pi^0$ final states in data are shown in Figure 5.8 and are fitted with a Gaussian and straight line. The result from the ΔE fit along with the ΔE resolutions are shown in Table 5.12. Due to the large backgrounds $\sigma_{\Delta E}$ had to be fixed.

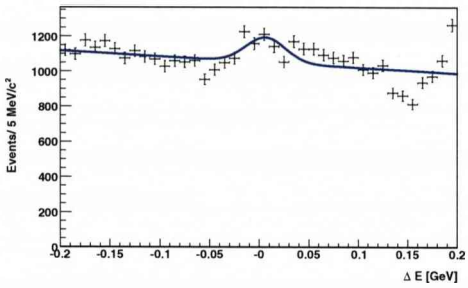

(a) $B \to D_s^+ D^{(*)} \pi^0$

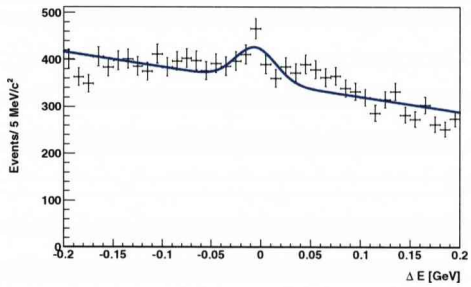

(b) $B \to D_s^+ D^{(*)} \gamma$

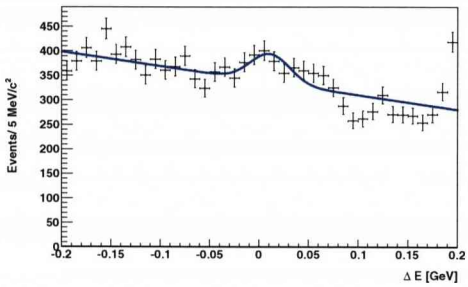

(c) $B \to D_s^{*+} D^{(*)} \pi^0$

Figure 5.8: *ΔE spectra for data*

Modes:	ΔE yield	ΔE_0 (MeV)	$\sigma_{\Delta E}$
$B \to D_{s0}^+ \overline{D}^{(*)} (D_{s0} \to D_s^+ \pi^0)$	711.51 ± 99.52	6.26 ± 4.53	20.0 (fixed)
$B \to D_{s1}^+ \overline{D}^{(*)} (D_{s1} \to D_s^+ \gamma)$	289.35 ± 57.48	10.72 ± 6.62	20.0 (fixed)
$B \to D_{s1}^+ \overline{D}^{(*)} (D_{s1} \to D_s^{*+} \pi^0)$	360.77 ± 59.50	-5.53 ± 4.92	20.0 (fixed)

Table 5.12: *ΔE yields and resolutions for data*

Figure 5.9 shows the ΔE spectra for Monte-Carlo described above with the addition of truth matching, whilst Figure 5.10 shows the reconstructed D_{sJ} mass spectra. The resolutions fitted are shown in Table 5.13 and are found to be better than for non truth matched events.

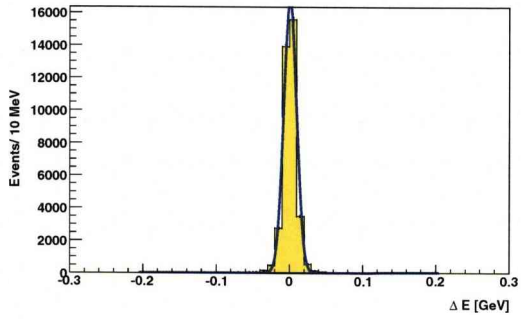

(a) $B \to D_s^+ D^{(*)} \pi^0$

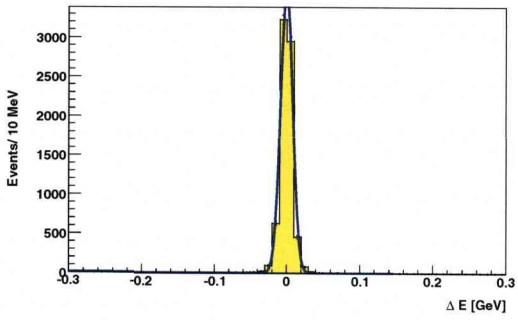

(b) $B \to D_s^{*+} D^{(*)} \pi^0$

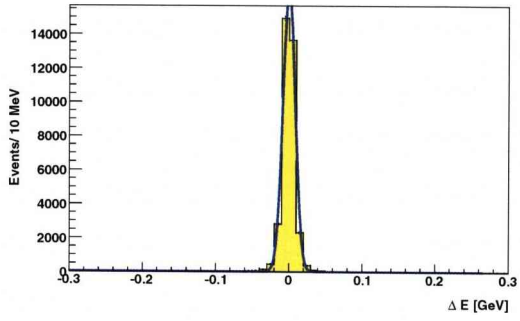

(c) $B \to D_s^+ D^{(*)} \gamma$

Figure 5.9: *ΔE spectra for signal Monte-Carlo, requiring truth matching*

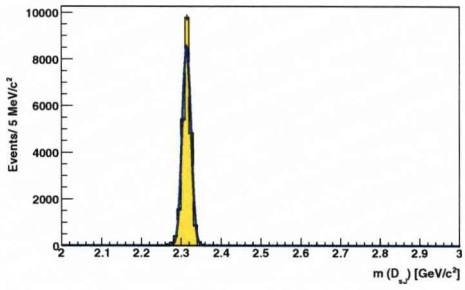

(a) $B \to D_s^+ D^{(*)} \pi^0$

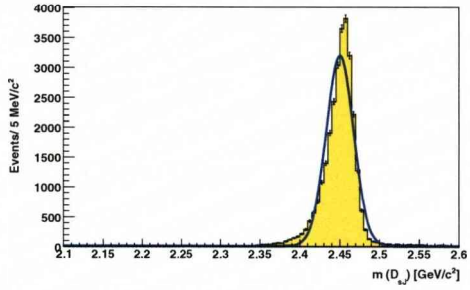

(b) $B \to D_s^+ D^{(*)} \gamma$

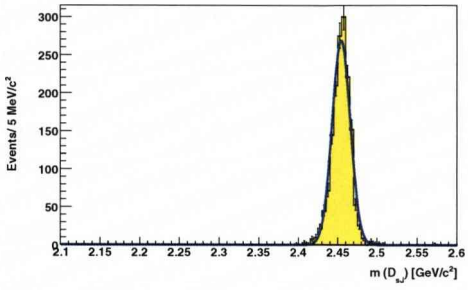

(c) $B \to D_s^{*+} D^{(*)} \pi^0$

Figure 5.10: *$m(D_{sJ})$ spectra for final states using signal Monte-Carlo with truth matching*

Modes:	ΔE (MeV)	$\sigma_{\Delta E}$	m(D_{sJ}) (MeV/c^2)	σ_m
$B \to D_{s0}^+ \overline{D}^{(*)} (D_{s0} \to D_s^+ \pi^0)$	0.60	8.78	2313.8	10.00
$B \to D_{s1}^+ \overline{D}^{(*)} (D_{s1} \to D_s^{*+} \pi^0)$	-0.60	8.33	2453.9	11.16
$B \to D_{s1}^+ \overline{D}^{(*)} (D_{s1} \to D_s^+ \gamma)$	-0.48	8.38	2450.9	15.62

Table 5.13: *ΔE and $m(D_{sJ})$ resolutions for truth matched signal Monte-Carlo*

In order to give the best $S/\sqrt{S+B}$ ratio, a cut of 2σ is chosen on ΔE and therefore the signal region is defined to be $|\Delta E - \Delta E_0| < 2\sigma_{\Delta E}$ where ΔE_0 and $\sigma_{\Delta E}$ are defined, for signal Monte-Carlo, as:

- $\Delta E_0 = 0$ MeV
- For $D_s^+\overline{D}^{(*)}\pi^0$ and $D_s^{*+}\overline{D}^{(*)}\pi^0$:
  - $\sigma_{\Delta E} = 10$ MeV
- For $D_s^+\overline{D}^{(*)}\gamma$:
  - $\sigma_{\Delta E} = 7.5$ MeV

For data $\Delta E_0 = 0$ MeV, whilst a fixed $\sigma_{\Delta E} = 20$ MeV is used because of the high backgrounds in the data.

Veto of Two-Body $B \to D_s D^{(*)}$ Decays

A large combinatorial background to the $D_s^{(*)+}D^{(*)}\gamma$ and $D_s^{(*)+}D^{(*)}\pi^0$ final states are two body decays $B \to D_s D^{(*)}$ which are associated with a random γ or π^0. To reduce this background a veto is applied on two body decays which are reconstructed using exactly the same selection cuts as in the D_{sJ} analysis. If a $B \to D_s D^{(*)}$ candidate with $|\Delta E - \Delta E_0| < 20$ MeV is found in the event then that event is rejected in the $B \to D_{sJ} D^{(*)}$ analysis.

Multiplicity

Final states containing π^0 and γ lead to a significant amount of B candidates per event, often due to the large combinatorial backgrounds. Figure 5.11 shows the multiplicity distributions for $D_s^+\overline{D}^{(*)}\pi^0$ final states (a), $D_s^{*+}\overline{D}^{(*)}\pi^0$ final states (b) and $D_s^{*+}\overline{D}^{(*)}\gamma$ final states (c) for data. Figure 5.12 shows the same multiplicity plots for signal Monte-Carlo.

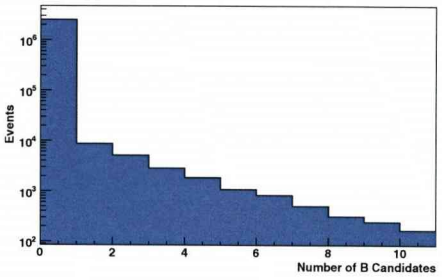

(a) $D_s^+\overline{D}^{(*)}\pi^0$

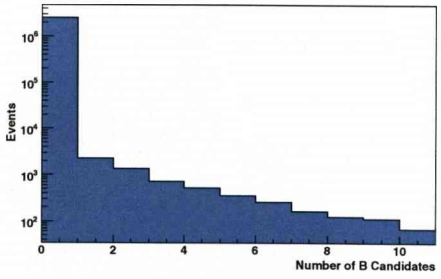

(b) $D_s^{*+}\overline{D}^{(*)}\pi^0$

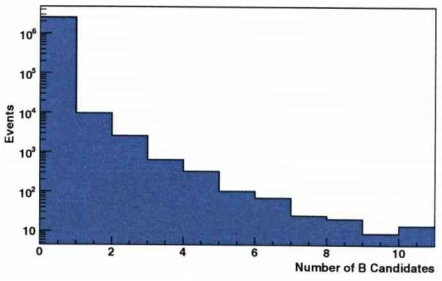

(c) $D_s^+\overline{D}^{(*)}\gamma$

Figure 5.11: *Number of B candidates per event for data*

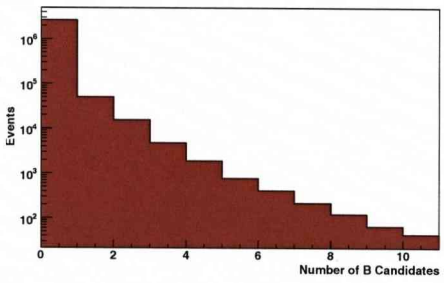

(a) $D_s^+\overline{D}^{(*)}\pi^0$

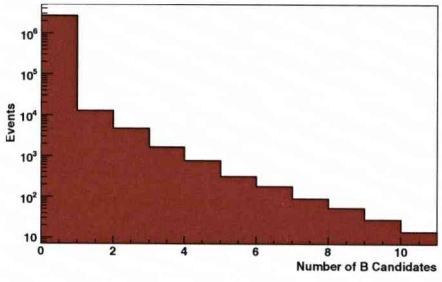

(b) $D_s^{*+}\overline{D}^{(*)}\pi^0$

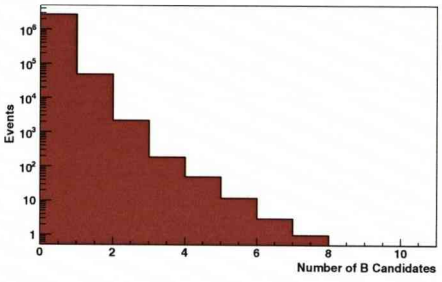

(c) $D_s^+\overline{D}^{(*)}\gamma$

Figure 5.12: *Number of B candidates per event for signal Monte-Carlo*

In order to reduce this "multiplicity" only one B candidate per event is selected and the candidate with the lowest $|\Delta E - \Delta E_0|$ is the one chosen.

To further reduce combinatorial backgrounds the following cuts are made on the γ and π^0 momenta:

- $p(\gamma) > 300$ MeV/c
- $p(\pi^0) < 600$ MeV/c

5.4 $\mathbf{D_{sJ}}$ Mass

The mass distributions for $D_s^+\pi^0$ (a), $D_s^+\gamma$ (b) and $D_s^+\pi^0$ (c) are shown in Figure 5.13 without the requirement of one candidate per event. The D_{sJ}^+ mass distributions are fitted with the sum of a Gaussian signal and exponential background and the reconstructed masses of the D_{sJ} are shown in Table 5.14.

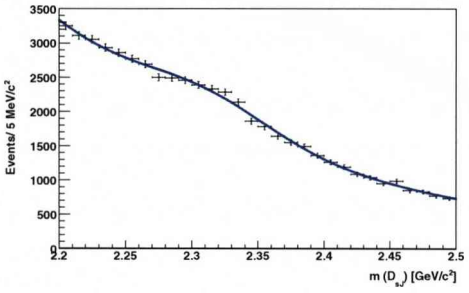

(a) $B \to D_s^+ D^{(*)}\pi^0$

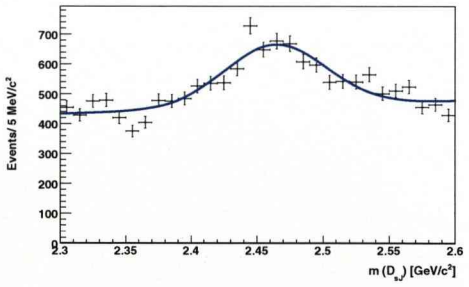

(b) $B \to D_s^+ D^{(*)}\gamma$

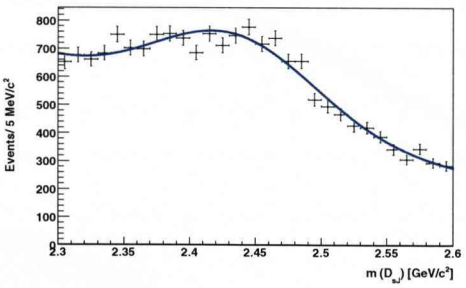

(c) $B \to D_s^{*+} D^{(*)}\pi^0$

Figure 5.13: *$m(D_{sJ})$ spectra for final states using data without the requirement of one candidate per events*

Modes:	Number of Events	m(D_{sJ}) (MeV/c^2)	σ_m
$B \to D_{s0}^{+}\overline{D}^{(*)}(D_{s0} \to D_s^{+}\pi^0)$	5647.5 ± 791.53	2310.1 ± 4.52	51.33 ± 6.79
$B \to D_{s1}^{+}\overline{D}^{(*)}(D_{s1} \to D_s^{+}\gamma)$	4956.7 ± 734.10	2434.0 ± 3.86	63.45 ± 6.26
$B \to D_{s1}^{+}\overline{D}^{(*)}(D_{s1} \to D_s^{*+}\pi^0)$	2003.2 ± 235.05	2463.9 ± 3.12	38.50 ± 4.09

Table 5.14: *Reconstructed D_{sJ} masses for data with multiple candidates*

m(D_{sJ}) distributions for the $D_s^{+}\pi^0$, $D_s^{+}\gamma$ and $D_s^{*+}\pi^0$ final states , with the requirement of a single B candidate, are shown in Figure 5.14. The distributions of m(D_{sJ}) are fitted with the sum of a Gaussian signal and an exponential background and the new reconstructed masses of the D_{sJ} are shown in Table 5.15.

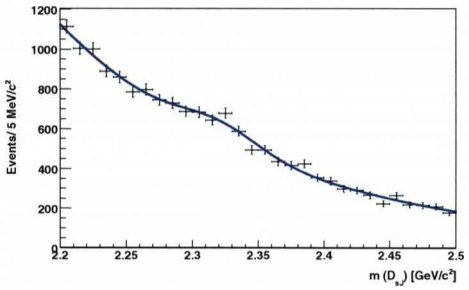

(a) $B \to D_s^{+}D^{(*)}\pi^0$

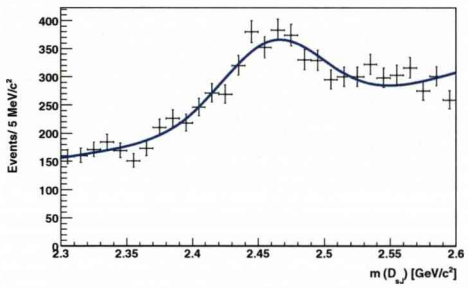

(b) $B \to D_s^{+}D^{(*)}\gamma$

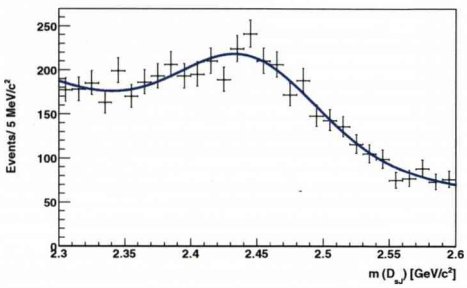

(c) $B \to D_s^{*+}D^{(*)}\pi^0$

Figure 5.14: *m(D_{sJ}) spectra for final states using data with the requirement of one candidate per event*

Modes:	Number of Events	m(D_{sJ}) (MeV/c^2)	σ_m
$B \to D_{s0}^{+}\overline{D}^{(*)}(D_{s0} \to D_s^{+}\pi^0)$	752.48 ± 198.4	2320.2 ± 5.0	30.6 ± 7.8
$B \to D_{s1}^{+}\overline{D}^{(*)}(D_{s1} \to D_s^{+}\gamma)$	1300.4 ± 195.3	2443.3 ± 4.1	51.7 ± 5.9
$B \to D_{s1}^{+}\overline{D}^{(*)}(D_{s1} \to D_s^{*+}\pi^0)$	1352.8 ± 168.7	2461.0 ± 3.3	38.6 ± 4.5

Table 5.15: *Reconstructed D_{sJ} masses for data*

The fits for the D_{sJ} are redone using different background functions so as to calculate a systematic error on the background fitting. In addition to the exponential background function, yields are determined for a second order polynomial and Gaussian background. The maximum difference in signal size is found to be 20% and this is taken as an estimate of the systematic error linked to the background description.

Chapter 6

Analysis Results

This chapter discusses the results of the analysis including an investigation of the two body cross check, the backgrounds of the analysis and finally the D_{sJ} Helicity Analysis to determine the D_{sJ} quantum numbers.

6.1 Two-Body Cross Check

The "Two-Body cross check" is designed to validate the analysis procedure used by calculating branching fractions and checking efficiencies and resolutions. Instead of pairing each D_s meson with a π^0 or γ it is combined with a $D^{(*)}$ to form the decay products of the B^+ and B^0. The analysis method used almost

duplicates that of the $B \to D^{(*)} D_{sJ}$ analysis (See Chapter 5) and the results from the $B \to D_s D^{(*)}$ can give confidence to the results produced in this thesis

The selection criteria are chosen to be the same as described in Chapter 5 which isn't optimal for measuring the branching fractions but is better for verifying the analysis procedure. The methods used are the same apart from the pairing of a π^0 or γ with the D_s candidate. Figures 6.1 and 6.2 show the ΔE distributions for Monte-Carlo and data respectively.

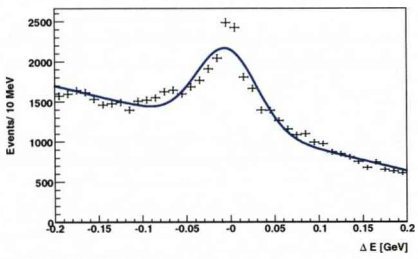

(a) $B^+ \to D_s^+ D^0$

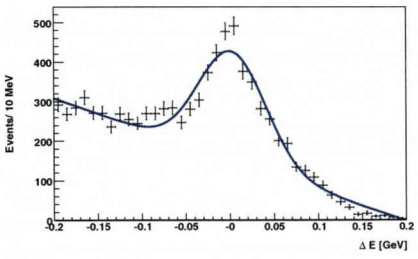

(b) $B^+ \to D_s^{*+} D^0$

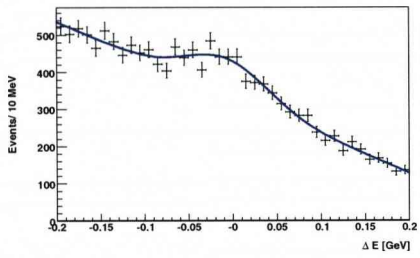

(c) $B^0 \to D_s^+ D^-$

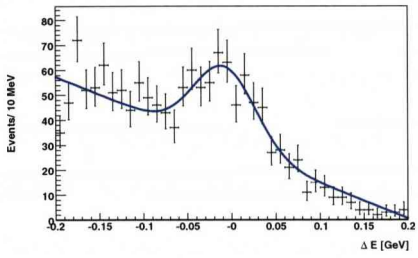

(d) $B^0 \to D_s^{*+} D^-$

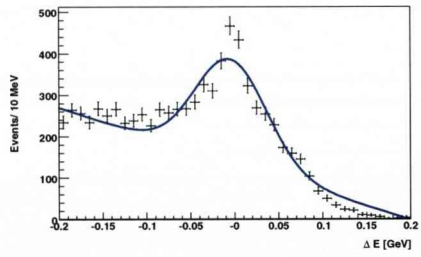

(e) $B^+ \to D_s^+ D^{*0}$

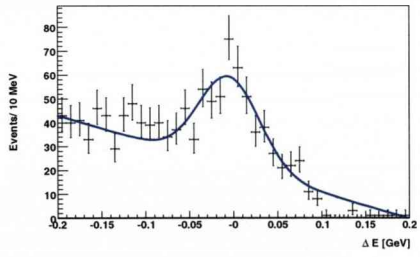

(f) $B^+ \to D_s^{*+} D^{*0}$

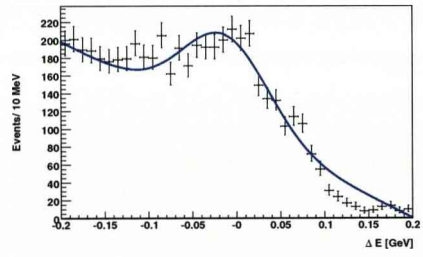

(g) $B^0 \to D_s^+ D^{*-}$

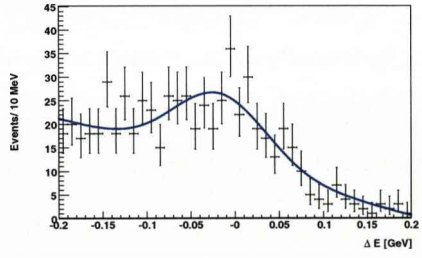

(h) $B^0 \to D_s^{*+} D^{*-}$

Figure 6.1: *ΔE spectra for $B \to D_s^{(*)} D^{(*)}$ using signal Monte-Carlo*

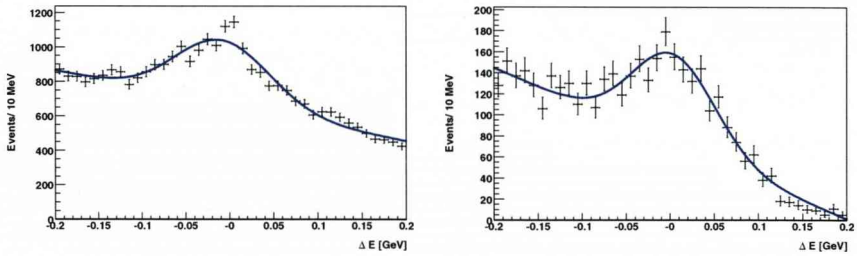

(a) $B^+ \to D_s^+ D^0$ (b) $B^+ \to D_s^{*+} D^0$

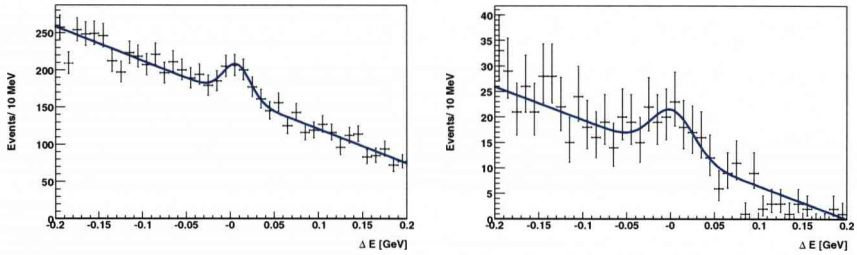

(c) $B^0 \to D_s^+ D^-$ (d) $B^0 \to D_s^{*+} D^-$

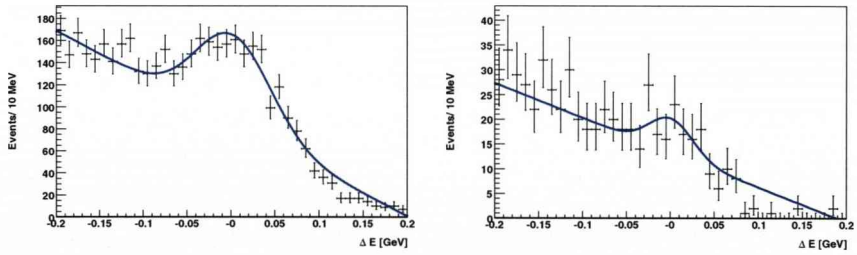

(e) $B^+ \to D_s^+ D^{*0}$ (f) $B^+ \to D_s^{*+} D^{*0}$

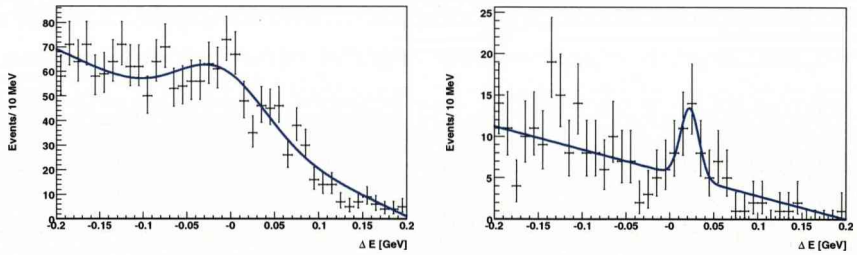

(g) $B^0 \to D_s^+ D^{*-}$ (h) $B^0 \to D_s^{*+} D^{*-}$

Figure 6.2: *ΔE spectra for $B \to D_s^{(*)} D^{(*)}$ using data*

Efficiencies are calculated by taking the Monte-Carlo samples and fitting the ΔE histograms for events yields. The ΔE spectra are fitted with the sum of a Gaussian signal and an exponential background, with fixed mean. These are then divided by the number of generated events to produce the efficiencies shown as percentages in Table 6.1. Event yields for data are calculated by fitting the ΔE histograms and are shown in Table 6.2.

Mode:			D_s^+		D_s^{*+}	
			$\phi\pi^+$	K^*K^+	$\phi\pi^+$	K^*K^+
	D^0	$K^+\pi^-$	$1.08^{-0.04}$	$1.42^{-0.34}$	$0.22^{-0.17}$	$0.26^{-0.21}$
		$K^+\pi^-\pi^0$	$1.01^{-0.92}$	$1.23^{-1.14}$	$0.19^{-0.19}$	$0.21^{-0.20}$
		$K^+\pi^-\pi^+\pi^-$	$0.99^{-0.84}$	$1.17^{-1.03}$	$0.17^{-0.16}$	$0.17^{-0.17}$
	D^+	$K^+\pi^-\pi^+$	$0.69^{-0.08}$	$1.11^{-0.34}$	$0.08^{-0.06}$	$0.12^{-0.10}$
$D^{*0} \to D^0\pi^0$	D^0	$K^+\pi^-$	$0.45^{-0.04}$	$0.61^{-0.18}$	$0.08^{-0.07}$	$0.10^{-0.08}$
		$K^+\pi^-\pi^0$	$0.15^{-0.13}$	$0.18^{-0.17}$	$0.03^{-0.03}$	$0.00^{-0.0}$
		$K^+\pi^-\pi^+\pi^-$	$0.18^{-0.16}$	$0.27^{-0.24}$	$0.03^{-0.03}$	$0.04^{-0.04}$
$D^{*0} \to D^0\gamma$	D^0	$K^+\pi^-$	$0.13^{-0.01}$	$0.17^{-0.05}$	$0.03^{-0.02}$	$0.04^{-0.03}$
		$K^+\pi^-\pi^0$	$0.13^{-0.11}$	$0.15^{-0.14}$	$0.09^{-0.09}$	$0.00^{-0.00}$
		$K^+\pi^-\pi^+\pi^-$	$0.02^{-0.01}$	$0.13^{-0.12}$	$0.01^{-0.01}$	$0.03^{-0.03}$
$D^{*0} \to D^0\pi^+$	D^0	$K^+\pi^-$	$0.23^{-0.02}$	$0.52^{-0.15}$	$0.03^{-0.02}$	$0.01^{-0.00}$
		$K^+\pi^-\pi^0$	$0.12^{-0.11}$	$0.30^{-0.28}$	$0.02^{-0.02}$	$0.01^{-0.01}$
		$K^+\pi^-\pi^+\pi^-$	$0.12^{-0.11}$	$0.25^{-0.23}$	$0.01^{-0.01}$	$0.03^{-0.03}$

Table 6.1: *Efficiencies for $B \to D_s^{(*)}D^{(*)}$ Monte-Carlo. The error shown is the systematic error due to the difference in width between data and Monte-Carlo*

Mode:			D_s^+		D_s^{*+}	
			$\phi\pi^+$	K^*K^+	$\phi\pi^+$	K^*K^+
	D^0	$K^+\pi^-$	$28.50 \pm 11.41 \pm 5.57$	$67.26 \pm 20.42 \pm 13.14$	$11.59 \pm 5.39 \pm 2.26$	$24.04 \pm 8.36 \pm 4.70$
		$K^+\pi^-\pi^0$	$369.62 \pm 35.88 \pm 72.22$	$1087.10 \pm 62.74 \pm 212.40$	$81.12 \pm 15.06 \pm 15.85$	$223.89 \pm 23.72 \pm 43.74$
		$K^+\pi^-\pi^+\pi^-$	$133.45 \pm 27.09 \pm 26.07$	$521.19 \pm 53.17 \pm 101.83$	$45.14 \pm 11.90 \pm 8.82$	$129.00 \pm 20.03 \pm 25.20$
	D^+	$K^+\pi^-\pi^+$	$31.04 \pm 18.50 \pm 6.06$	$166.73 \pm 36.30 \pm 32.58$	$10.63 \pm 7.05 \pm 2.08$	$35.69 \pm 11.42 \pm 6.97$
$D^{*0} \to D^0\pi^0$	D^0	$K^+\pi^-$	$17.55 \pm 5.67 \pm 3.43$	$14.13 \pm 5.77 \pm 2.76$	$0.79 \pm 1.81 \pm 0.15$	$1.49 \pm 1.40 \pm 0.29$
		$K^+\pi^-\pi^0$	$19.21 \pm 6.95 \pm 3.75$	$66.86 \pm 13.63 \pm 13.06$	$1.43 \pm 1.99 \pm 0.28$	$2.12 \pm 4.47 \pm 0.41$
		$K^+\pi^-\pi^+\pi^-$	$26.98 \pm 7.55 \pm 5.27$	$64.76 \pm 13.69 \pm 12.65$	$3.18 \pm 2.77 \pm 0.62$	$3.15 \pm 3.99 \pm 0.62$
$D^{*0} \to D^0\gamma$	D^0	$K^+\pi^-$	$3.50 \pm 4.18 \pm 0.68$	$8.61 \pm 6.77 \pm 1.68$	$4.79 \pm 3.07 \pm 0.94$	$6.47 \pm 3.14 \pm 1.26$
		$K^+\pi^-\pi^0$	$38.93 \pm 10.99 \pm 7.61$	$90.88 \pm 17.74 \pm 17.76$	$14.77 \pm 5.36 \pm 2.89$	$4.41 \pm 5.86 \pm 0.86$
		$K^+\pi^-\pi^+\pi^-$	$20.84 \pm 8.16 \pm 4.07$	$124.75 \pm 18.78 \pm 24.37$	$4.36 \pm 3.66 \pm 0.85$	$7.48 \pm 5.24 \pm 1.46$
$D^{*0} \to D^0\pi^+$	D^0	$K^+\pi^-$	$5.13 \pm 3.13 \pm 1.00$	$16.08 \pm 6.51 \pm 3.14$	$1.09 \pm 1.76 \pm 0.21$	$5.21 \pm 3.02 \pm 1.02$
		$K^+\pi^-\pi^0$	$23.61 \pm 8.72 \pm 4.61$	$73.57 \pm 15.53 \pm 14.37$	$9.75 \pm 4.27 \pm 1.91$	$10.49 \pm 4.44 \pm 2.05$
		$K^+\pi^-\pi^+\pi^-$	$15.76 \pm 6.14 \pm 3.08$	$35.33 \pm 12.64 \pm 6.90$	$3.29 \pm 3.43 \pm 0.64$	$4.88 \pm 4.24 \pm 0.95$

Table 6.2: *Event Yields for $B \to D_s^{(*)} D^{(*)}$ data. The errors shown are the statistical error and the systematic error due to the background fit*

The $B \to D^{(*)} D_s^*$ Branching Fractions are calculated according to the following equation:

$$BR(B \to D^{(*)} D_s^{*+}) = \frac{N_{obs}}{N_{B\overline{B}} \times BR(D^{(*)} \to j) BR(D_s^{(*)} \to k) \times \varepsilon_{jk}} \tag{6.1}$$

Where N_{obs} is the number of observed events of the decay mode, $N_{B\overline{B}}$ is the total number of $B\overline{B}$ events, $BR(D^{(*)} \to j)$ and $BR(D_s^{(*)} \to k)$ are the daughter branching fractions of the $D^{(*)}$ and $D_s^{(*)}$, j and k are the products of those decays and ε_{jk} is the efficiency of the submodes with j and k decay products.

The $B \to D^{(*)}D_s^*$ branching fractions produced are shown in Table 6.3. The branching fractions are also shown in Figure 6.3 which also shows the branching fractions contained within the PDG [54]. The results suggests that the analysis procedure is valid, although there are high backgrounds which need keeping under control.

Mode:			D_s^+		D_s^{*+}	
			$\phi\pi^+$	K^*K^+	$\phi\pi^+$	K^*K^+
	D^0	$K^+\pi^-$	$8.07 \pm 3.46 \pm 1.58^{-0.28}$	$12.12 \pm 4.13 \pm 2.37^{-2.94}$	$17.45 \pm 8.54 \pm 3.41^{-13.52}$	$25.37 \pm 9.66 \pm 4.96^{-20.89}$
		$K^+\pi^-\pi^0$	$31.18 \pm 5.72 \pm 6.09^{-28.30}$	$63.42 \pm 10.67 \pm 12.39^{-58.82}$	$38.84 \pm 9.41 \pm 7.59^{-38.00}$	$82.21 \pm 15.65 \pm 16.06^{-80.81}$
		$K^+\pi^-\pi^+\pi^-$	$19.90 \pm 5.06 \pm 3.89^{-17.01}$	$55.09 \pm 10.26 \pm 10.76^{-48.80}$	$41.69 \pm 12.72 \pm 8.15^{-40.28}$	$98.57 \pm 21.70 \pm 19.26^{-95.94}$
	D^+	$K^+\pi^-\pi^+$	$5.81 \pm 3.58 \pm 1.14^{-0.64}$	$16.25 \pm 4.36 \pm 3.18^{-4.91}$	$17.95 \pm 12.22 \pm 3.51^{-14.22}$	$34.34 \pm 12.23 \pm 6.71^{-28.74}$
$D^{*0} \to D^0\pi^0$	D^0	$K^+\pi^-$	$19.33 \pm 6.96 \pm 3.78^{-1.88}$	$9.65 \pm 4.24 \pm 1.89^{-2.82}$	$5.01 \pm 11.50 \pm 0.98^{-3.95}$	$6.80 \pm 6.49 \pm 1.33^{-5.68}$
		$K^+\pi^-\pi^0$	$18.21 \pm 7.22 \pm 3.56^{-16.63}$	$42.24 \pm 11.07 \pm 8.25^{-39.37}$	$6.98 \pm 9.78 \pm 1.36^{-6.84}$	$0.00 \pm 0.00 \pm 0.00^{-0.00}$
		$K^+\pi^-\pi^+\pi^-$	$34.96 \pm 11.28 \pm 6.83^{-30.21}$	$48.50 \pm 12.94 \pm 9.48^{-43.33}$	$23.21 \pm 20.55 \pm 4.53^{-22.47}$	$15.29 \pm 19.52 \pm 2.99^{-14.90}$
$D^{*0} \to D^0\gamma$	D^0	$K^+\pi^-$	$20.86 \pm 25.17 \pm 4.08^{-2.03}$	$33.78 \pm 27.19 \pm 6.60^{-9.86}$	$158.04 \pm 104.80 \pm 30.88^{-124.74}$	$113.90 \pm 58.66 \pm 22.25^{-95.07}$
		$K^+\pi^-\pi^0$	$68.74 \pm 22.77 \pm 13.43^{-62.80}$	$117.52 \pm 30.84 \pm 22.96^{-109.54}$	$37.46 \pm 15.07 \pm 7.32^{-36.70}$	$0.00 \pm 0.00 \pm 0.00^{-0.00}$
		$K^+\pi^-\pi^+\pi^-$	$513.76 \pm 219.58 \pm 100.38^{-443.89}$	$304.42 \pm 69.93 \pm 59.48^{-271.94}$	$149.21 \pm 127.84 \pm 29.15^{-144.48}$	$96.22 \pm 69.44 \pm 18.80^{-93.82}$
$D^{*0} \to D^0\pi^+$	D^0	$K^+\pi^-$	$9.86 \pm 6.20 \pm 1.93^{-0.96}$	$11.74 \pm 5.09 \pm 2.29^{-3.43}$	$17.92 \pm 29.07 \pm 3.50^{-14.15}$	$366.33 \pm 219.79 \pm 71.57^{-305.77}$
		$K^+\pi^-\pi^0$	$25.11 \pm 10.06 \pm 4.91^{-22.94}$	$26.19 \pm 6.91 \pm 5.12^{-24.41}$	$58.70 \pm 27.29 \pm 11.47^{-57.52}$	$206.52 \pm 93.33 \pm 40.35^{-203.25}$
		$K^+\pi^-\pi^+\pi^-$	$28.15 \pm 11.79 \pm 5.50^{-24.32}$	$25.32 \pm 9.88 \pm 4.95^{-22.62}$	$53.15 \pm 56.01 \pm 10.38^{-51.46}$	$29.51 \pm 26.05 \pm 5.77^{-28.77}$

Table 6.3: *Branching fractions for $B \to D_s^{(*)}D^{(*)}$ ($\times 10^{-3}$). The errors shown are the statistical error, the systematic error due to the background fit and the systematic error due to the difference in width between data and Monte-Carlo)*

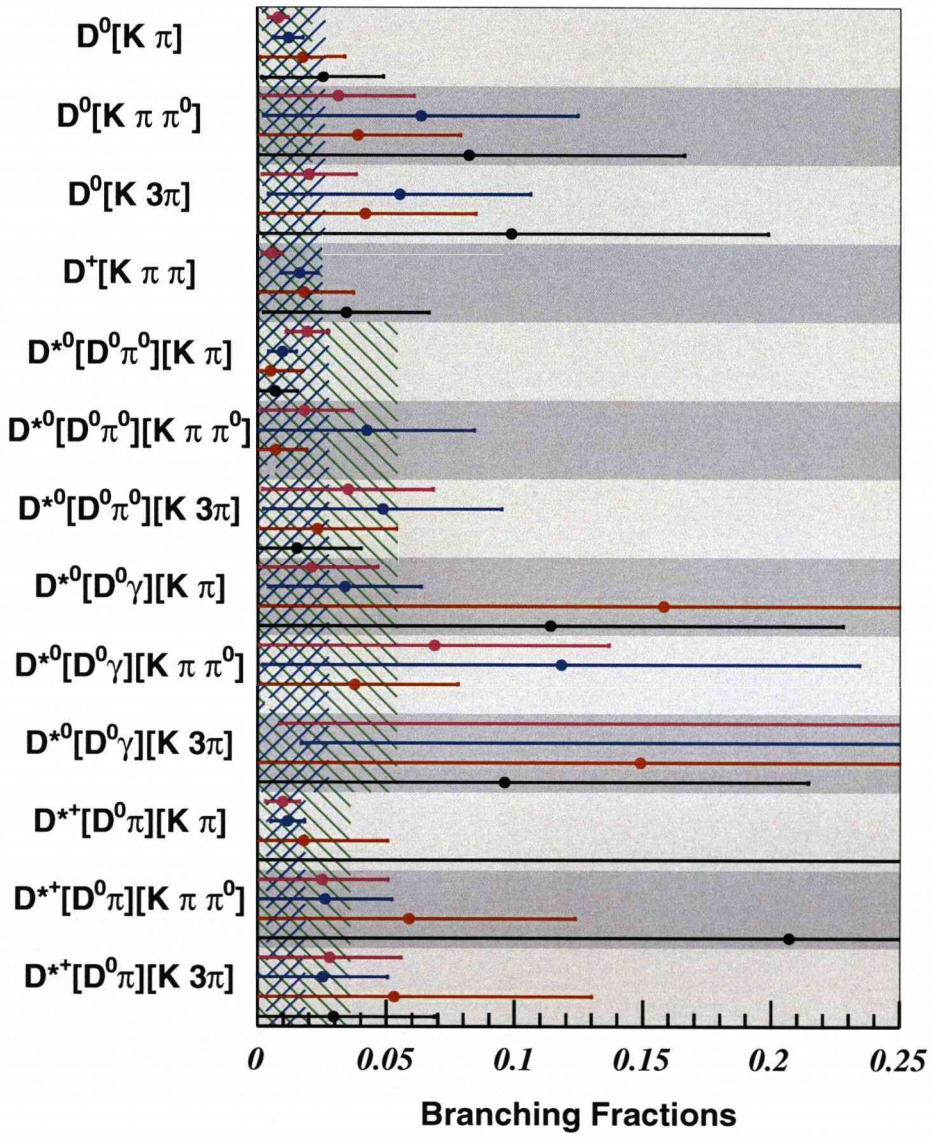

Figure 6.3: *Branching Fractions for $B \to D_s^{(*)} D^{(*)}$. The pink points correspond to $D_s^+ \to \phi\pi$ decays. The blue points correspond to $D_s^+ \to K^*K$ decays. The red points correspond to $D_s^{*+} \to D_s\gamma(D_s \to \phi\pi)$ decays. The black points correspond to $D_s^{*+} \to D_s^+\gamma(D_s \to K^*K)$ decays. The purple shaded region corresponds to the one sigma uncertainty around the $D^{(*)}D_s$ PDG branching fractions. The green shaded region corresponds to the one sigma uncertainty around the $D^{(*)}D_s^*$ PDG branching fractions.* Pink and blue points compare to the purple band, red and black compare to the green band.

6.2 Backgrounds and Signal Efficiency

This section introduces some of the backgrounds to this analysis and investigates their possible effects. There are three types of background that are studied which are two body decays, generic B decays and signal cross-feed. The two-body and generic samples are studied to determine whether there are any peaking in the backgrounds and the cross-feed is studied to determine whether events can be incorrectly reconstructed in the wrong mode.

6.2.1 Generic Background

The generic B sample was used to look for potential sources of peaking background that may be present. The generic events were processed in the same way as the signal events described in Section 5.3. Figure 6.4 shows plots of ΔE and m(D_{sJ}) analogous to those in Figure 5.7. There is found to be peaking background, the reason is that some proportion of the D_{sJ} decay chains are found in the generic MC datasets.

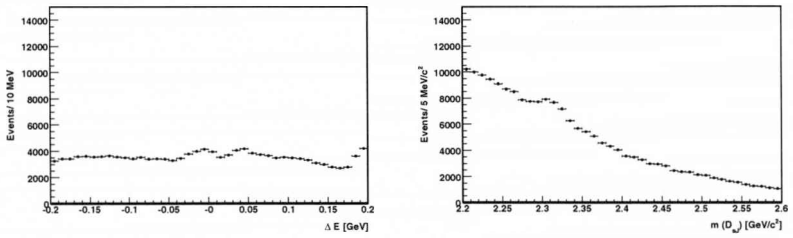

(a) $B \to D_s^+ D^{(*)} \pi^0$

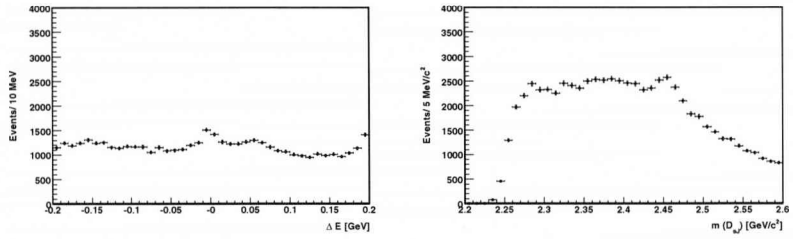

(b) $B \to D_s^{*+} D^{(*)} \pi^0$

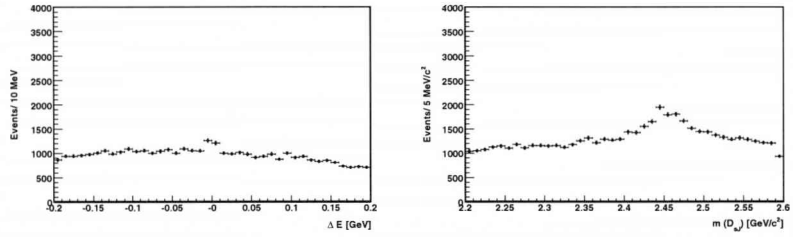

(c) $B \to D_s^+ D^{(*)} \gamma$

Figure 6.4: *ΔE and $m(D_{sJ})$ spectra for final states using generic Monte-Carlo*

6.2.2 Two-Body Background

Section 6.1 described the use of two-body decays as a validation of the analysis procedure. These modes are also considered as a potential peaking background

due to their close relation to the signal. The two body Monte-Carlo dataset was subject to the same procedure as in Section 5.3 and the ΔE and m(D_{sJ}) spectra are shown in Figure 6.5. No evidence for peaking background is seen in the D_{sJ} signal regions.

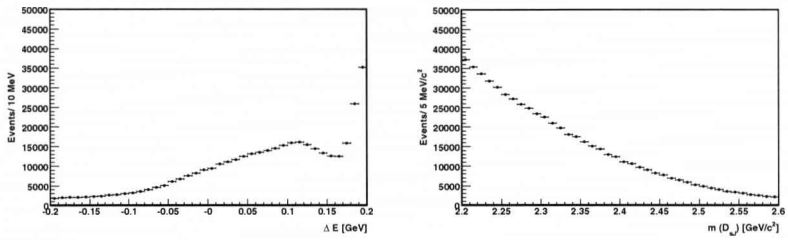

(a) $B \to D_s^+ D^{(*)} \pi^0$

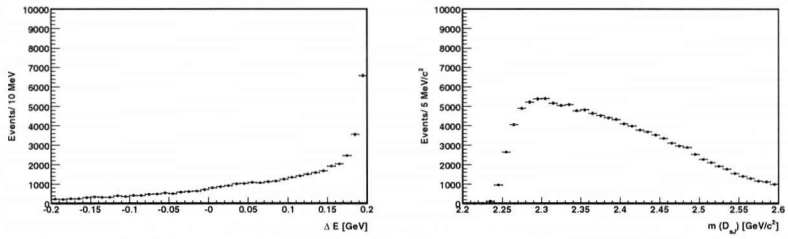

(b) $B \to D_s^{*+} D^{(*)} \pi^0$

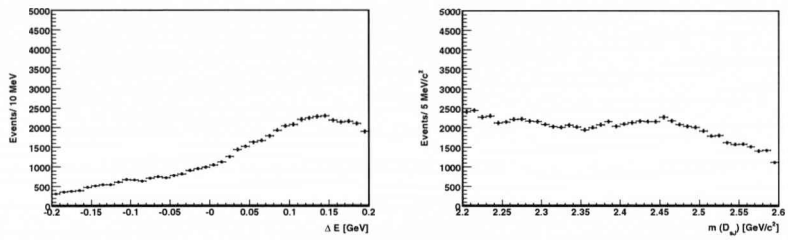

(c) $B \to D_s^+ D^{(*)} \gamma$

Figure 6.5: *ΔE and $m(D_{sJ})$ spectra for final states using two-body Monte-Carlo*

6.2.3 Efficiencies and Cross-Feed

The signal Monte-Carlo samples are used to determine the efficiencies of reconstructed events and the cross-feed of misreconstructed events. The cross-feed ε_{ij} is defined as the ratio of the number of events reconstructed as the final state j to the total number of simulated events in the Monte-Carlo sample corresponding to state i (N_{Reco}/N_{Gen}). Tables 6.4, 6.6 and 6.8 show the efficiencies ($i = j$) and Tables 6.5, 6.7 and 6.9 show the cross-feed ($i \neq j$) elements corresponding to the largest magnitudes. The main sources of cross-feed are identified to be:

D^{*+} reconstructed as D^{*0} :

- The π^+ from the $D^{*+} \to D^0\pi^+$ is not reconstructed and the D^0 is associated with a π^0 or γ from combinatorial background to misreconstruct a D^{*0}. This acts as a cross feed from the modes $B^0 \to D_{sJ}^+ D^{*-}$ to modes $B^+ \to D_{sJ}^+ D^{*0}$.

$B^0 \to D_{s0}^+ D^{*-}$ reconstructed as $B^+ \to D_{s1}^+ D^0$ [$D_{s1}^+ \to D_s^{*+}\pi^0$] :

- The π^+ from the D^{*-} is not reconstructed and a fake D_s^{*+} is reconstructed from the D_s^+ and a γ from combinatorial background.

$B^+ \to D_{s0}^+ D^{*0}$ [$D_{s0}^+ \to D_s^+\pi^0$] as $B^+ \to D_{s1}^+ D^0$ [$D_{s1}^+ \to D_s^{*+}\pi^0$] :

- The γ from the D^{*0} is not reconstructed and a fake D_s^{*+} is reconstructed from the D_s^+ and a γ from combinatorial background.

$B^+ \to D_{s1}^+ D^0$ $[D_{s1}^+ \to D_s^{*+}\pi^0]$ as $B^+ \to D_{s0}^+ D^{*0}$ $[D_{s0}^+ \to D_s^+\pi^0]$:

- The γ from the D_s^{*+} is not reconstructed and a fake D^{*0} is built from the D^0 and a π^0 or γ from combinatorial background.

B Mode Generated	Final State Reconstructed	Efficiency (%)
$D_{s0}^+ D^-$ $(\phi\pi \times K\pi\pi)$	$D_s^+ D^-\pi^0$ $(\phi\pi \times K\pi\pi)$	9.20 ± 1.34
$D_{s0}^+ D^-$ $(K^{*0}K \times K\pi\pi)$	$D_s^+ D^-\pi^0$ $(K^{*0}K \times K\pi\pi)$	1.81 ± 1.67
$D_{s0}^+ D^{*-}$ $(\phi\pi \times K\pi)$	$D_s^+ D^{*-}\pi^0$ $(\phi\pi \times K\pi)$	7.90 ± 2.31
$D_{s0}^+ D^{*-}$ $(\phi\pi \times K\pi\pi^0)$	$D_s^+ D^{*-}\pi^0$ $(\phi\pi \times K\pi\pi^0)$	2.31 ± 2.06
$D_{s0}^+ D^{*-}$ $(\phi\pi \times K3\pi)$	$D_s^+ D^{*-}\pi^0$ $(\phi\pi \times K3\pi)$	2.55 ± 2.38
$D_{s0}^+ D^{*-}$ $(K^{*0}K \times K\pi)$	$D_s^+ D^{*-}\pi^0$ $(K^{*0}K \times K\pi)$	4.76 ± 4.45
$D_{s0}^+ D^{*-}$ $(K^{*0}K \times K\pi\pi^0)$	$D_s^+ D^{*-}\pi^0$ $(K^{*0}K \times K\pi\pi^0)$	1.74 ± 1.72
$D_{s0}^+ D^{*-}$ $(K^{*0}K \times K3\pi)$	$D_s^+ D^{*-}\pi^0$ $(K^{*0}K \times K3\pi)$	1.90 ± 1.89
$D_{s0}^+ D^0$ $(\phi\pi \times K\pi)$	$D_s^+ D^0\pi^0$ $(\phi\pi \times K\pi)$	0.28 ± 0.02
$D_{s0}^+ D^0$ $(\phi\pi \times K\pi\pi^0)$	$D_s^+ D^0\pi^0$ $(\phi\pi \times K\pi\pi^0)$	0.04 ± 0.03
$D_{s0}^+ D^0$ $(\phi\pi \times K3\pi)$	$D_s^+ D^0\pi^0$ $(\phi\pi \times K3\pi)$	0.04 ± 0.04
$D_{s0}^+ D^0$ $(K^{*0}K \times K\pi)$	$D_s^+ D^0\pi^0$ $(K^{*0}K \times K\pi)$	0.25 ± 0.23
$D_{s0}^+ D^0$ $(K^{*0}K \times K\pi\pi^0)$	$D_s^+ D^0\pi^0$ $(K^{*0}K \times K\pi\pi^0)$	0.04 ± 0.04
$D_{s0}^+ D^0$ $(K^{*0}K \times K3\pi)$	$D_s^+ D^0\pi^0$ $(K^{*0}K \times K3\pi)$	0.05 ± 0.05
$D_{s0}^+ D^{*0}$ $(\phi\pi \times K\pi)$	$D_s^+ D^{*0}\pi^0$ $(\phi\pi \times K\pi)$	0.04 ± 0.01
$D_{s0}^+ D^{*0}$ $(\phi\pi \times K\pi\pi^0)$	$D_s^+ D^{*0}\pi^0$ $(\phi\pi \times K\pi\pi^0)$	0.00 ± 0.00
$D_{s0}^+ D^{*0}$ $(\phi\pi \times K3\pi)$	$D_s^+ D^{*0}\pi^0$ $(\phi\pi \times K3\pi)$	0.00 ± 0.00
$D_{s0}^+ D^{*0}$ $(K^{*0}K \times K\pi)$	$D_s^+ D^{*0}\pi^0$ $(K^{*0}K \times K\pi)$	0.05 ± 0.05
$D_{s0}^+ D^{*0}$ $(K^{*0}K \times K\pi\pi^0)$	$D_s^+ D^{*0}\pi^0$ $(K^{*0}K \times K\pi\pi^0)$	0.01 ± 0.01
$D_{s0}^+ D^{*0}$ $(K^{*0}K \times K3\pi)$	$D_s^+ D^{*0}\pi^0$ $(K^{*0}K \times K3\pi)$	0.01 ± 0.01

Table 6.4: *Efficiencies for reconstructed $D_s^+\pi^0$ final states*

B Mode Generated	Final State Reconstructed	Cross-Feed (%)
$D_{s0}^{+}D^{0}$ $(\phi\pi \times K\pi\pi^{0})$	$D_{s}^{+}D^{-}\pi^{0}$ $(\phi\pi \times K\pi\pi)$	0.13 ± 0.02
$D_{s0}^{+}D^{-}$ $(\phi\pi \times K\pi\pi)$	$D_{s}^{+}D^{0}\pi^{0}$ $(\phi\pi \times K\pi\pi^{0})$	0.01 ± 0.01
$D_{s0}^{+}D^{-}$ $(K^{*0}K \times K\pi\pi)$	$D_{s}^{+}D^{0}\pi^{0}$ $(K^{*0}K \times K\pi\pi^{0})$	0.02 ± 0.02
$D_{s0}^{+}D^{*-}$ $(\phi\pi \times K\pi)$	$D_{s}^{+}D^{*0}\pi^{0}$ $(\phi\pi \times K\pi)$	0.01 ± 0.00
$D_{s1}^{+}D^{0}$ $(\phi\pi \times K\pi)$		0.01 ± 0.00
$D_{s0}^{+}D^{*-}$ $(\phi\pi \times K\pi\pi^{0})$	$D_{s}^{+}D^{*0}\pi^{0}$ $(\phi\pi \times K\pi\pi^{0})$	0.00 ± 0.00
$D_{s1}^{+}D^{0}$ $(\phi\pi \times K\pi\pi^{0})$		0.00 ± 0.00
$D_{s0}^{+}D^{*-}$ $(\phi\pi \times K3\pi)$	$D_{s}^{+}D^{*0}\pi^{0}$ $(\phi\pi \times K3\pi)$	0.01 ± 0.01
$D_{s1}^{+}D^{0}$ $(\phi\pi \times K3\pi)$		0.00 ± 0.00
$D_{s0}^{+}D^{*-}$ $(K^{*0}K \times K\pi)$	$D_{s}^{+}D^{*0}\pi^{0}$ $(K^{*0}K \times K\pi)$	0.01 ± 0.01
$D_{s1}^{+}D^{0}$ $(K^{*0}K \times K\pi)$		0.00 ± 0.00
$D_{s0}^{+}D^{*-}$ $(K^{*0}K \times K\pi\pi^{0})$	$D_{s}^{+}D^{*0}\pi^{0}$ $(K^{*0}K \times K\pi\pi^{0})$	0.00 ± 0.00
$D_{s1}^{+}D^{0}$ $(K^{*0}K \times K\pi\pi^{0})$		0.00 ± 0.00
$D_{s0}^{+}D^{*-}$ $(K^{*0}K \times K3\pi)$	$D_{s}^{+}D^{*0}\pi^{0}$ $(K^{*0}K \times K3\pi)$	0.00 ± 0.00
$D_{s1}^{+}D^{0}$ $(K^{*0}K \times K3\pi)$		0.00 ± 0.00

Table 6.5: *Cross-feed matrix for reconstructed $D_{s}^{+}\pi^{0}$ final states*

B Mode Generated	Final State Reconstructed	Efficiency (%)
$D_{s1}^{+}D^{-}$ $(\phi\pi \times K\pi\pi)$	$D_s^{+}D^{-}\gamma$ $(\phi\pi \times K\pi\pi)$	4.86 ± 0.71
$D_{s1}^{+}D^{-}$ $(K^{*0}K \times K\pi\pi)$	$D_s^{+}D^{-}\gamma$ $(K^{*0}K \times K\pi\pi)$	3.71 ± 3.42
$D_{s1}^{+}D^{*-}$ $(\phi\pi \times K\pi)$	$D_s^{+}D^{*-}\gamma$ $(\phi\pi \times K\pi)$	4.33 ± 1.26
$D_{s1}^{+}D^{*-}$ $(\phi\pi \times K\pi\pi^0)$	$D_s^{+}D^{*-}\gamma$ $(\phi\pi \times K\pi\pi^0)$	2.13 ± 1.90
$D_{s1}^{+}D^{*-}$ $(\phi\pi \times K3\pi)$	$D_s^{+}D^{*-}\gamma$ $(\phi\pi \times K3\pi)$	1.69 ± 1.58
$D_{s1}^{+}D^{*-}$ $(K^{*0}K \times K\pi)$	$D_s^{+}D^{*-}\gamma$ $(K^{*0}K \times K\pi)$	2.79 ± 2.61
$D_{s1}^{+}D^{*-}$ $(K^{*0}K \times K\pi\pi^0)$	$D_s^{+}D^{*-}\gamma$ $(K^{*0}K \times K\pi\pi^0)$	1.64 ± 1.62
$D_{s1}^{+}D^{*-}$ $(K^{*0}K \times K3\pi)$	$D_s^{+}D^{*-}\gamma$ $(K^{*0}K \times K3\pi)$	1.28 ± 1.27
$D_{s1}^{+}D^{0}$ $(\phi\pi \times K\pi)$	$D_s^{+}D^{0}\gamma$ $(\phi\pi \times K\pi)$	0.20 ± 0.01
$D_{s1}^{+}D^{0}$ $(\phi\pi \times K\pi\pi^0)$	$D_s^{+}D^{0}\gamma$ $(\phi\pi \times K\pi\pi^0)$	0.04 ± 0.03
$D_{s1}^{+}D^{0}$ $(\phi\pi \times K3\pi)$	$D_s^{+}D^{0}\gamma$ $(\phi\pi \times K3\pi)$	0.02 ± 0.02
$D_{s1}^{+}D^{0}$ $(K^{*0}K \times K\pi)$	$D_s^{+}D^{0}\gamma$ $(K^{*0}K \times K\pi)$	0.16 ± 0.15
$D_{s1}^{+}D^{0}$ $(K^{*0}K \times K\pi\pi^0)$	$D_s^{+}D^{0}\gamma$ $(K^{*0}K \times K\pi\pi^0)$	0.03 ± 0.03
$D_{s1}^{+}D^{0}$ $(K^{*0}K \times K3\pi)$	$D_s^{+}D^{0}\gamma$ $(K^{*0}K \times K3\pi)$	0.03 ± 0.03
$D_{s1}^{+}D^{*0}$ $(\phi\pi \times K\pi)$	$D_s^{+}D^{*0}\gamma$ $(\phi\pi \times K\pi)$	0.05 ± 0.01
$D_{s1}^{+}D^{*0}$ $(\phi\pi \times K\pi\pi^0)$	$D_s^{+}D^{*0}\gamma$ $(\phi\pi \times K\pi\pi^0)$	0.00 ± 0.00
$D_{s1}^{+}D^{*0}$ $(\phi\pi \times K3\pi)$	$D_s^{+}D^{*0}\gamma$ $(\phi\pi \times K3\pi)$	0.01 ± 0.01
$D_{s1}^{+}D^{*0}$ $(K^{*0}K \times K\pi)$	$D_s^{+}D^{*0}\gamma$ $(K^{*0}K \times K\pi)$	0.05 ± 0.05
$D_{s1}^{+}D^{*0}$ $(K^{*0}K \times K\pi\pi^0)$	$D_s^{+}D^{*0}\gamma$ $(K^{*0}K \times K\pi\pi^0)$	0.00 ± 0.00
$D_{s1}^{+}D^{*0}$ $(K^{*0}K \times K3\pi)$	$D_s^{+}D^{*0}\gamma$ $(K^{*0}K \times K3\pi)$	0.01 ± 0.01

Table 6.6: *Efficiencies for reconstructed $D_s^{+}\gamma$ final states*

B Mode Generated	Final State Reconstructed	Cross-Feed (%)
$D_{s1}^{+}D^{0}$ $(\phi\pi \times K\pi\pi^{0})$	$D_{s}^{+}D^{-}\gamma$ $(\phi\pi \times K\pi\pi)$	0.04 ± 0.01
$D_{s1}^{+}D^{0}$ $(K^{*0}K \times K\pi\pi^{0})$	$D_{s}^{+}D^{-}\gamma$ $(K^{*0}K \times K\pi\pi)$	0.03 ± 0.03
$D_{s1}^{+}D^{-}$ $(\phi\pi \times K\pi\pi)$		0.01 ± 0.01
$D_{s1}^{+}D^{*-}$ $(\phi\pi \times K\pi\pi^{0})$	$D_{s}^{+}D^{0}\gamma$ $(\phi\pi \times K\pi\pi^{0})$	0.01 ± 0.01
$D_{s1}^{+}D^{*0}$ $(\phi\pi \times K\pi\pi^{0})$		0.01 ± 0.01
$D_{s1}^{+}D^{*-}$ $(\phi\pi \times K3\pi)$	$D_{s}^{+}D^{0}\gamma$ $(\phi\pi \times K3\pi)$	0.01 ± 0.01
$D_{s1}^{+}D^{*0}$ $(\phi\pi \times K3\pi)$		0.01 ± 0.01
$D_{s1}^{+}D^{-}$ $(K^{*0}K \times K\pi\pi)$		0.01 ± 0.01
$D_{s1}^{+}D^{*-}$ $(K^{*0}K \times K\pi\pi^{0})$	$D_{s}^{+}D^{0}\gamma$ $(K^{*0}K \times K\pi\pi^{0})$	0.01 ± 0.01
$D_{s1}^{+}D^{*0}$ $(K^{*0}K \times K\pi\pi^{0})$		0.01 ± 0.01
$D_{s1}^{+}D^{*-}$ $(\phi\pi \times K\pi)$	$D_{s}^{+}D^{*0}\gamma$ $(\phi\pi \times K\pi)$	0.01 ± 0.00
$D_{s1}^{+}D^{*-}$ $(\phi\pi \times K\pi\pi^{0})$	$D_{s}^{+}D^{*0}\gamma$ $(\phi\pi \times K\pi\pi^{0})$	0.00 ± 0.00
$D_{s1}^{+}D^{0}$ $(\phi\pi \times K\pi\pi^{0})$		0.00 ± 0.00
$D_{s1}^{+}D^{*-}$ $(\phi\pi \times K3\pi)$	$D_{s}^{+}D^{*0}\gamma$ $(\phi\pi \times K3\pi)$	0.00 ± 0.00
$D_{s1}^{+}D^{*-}$ $(K^{*0}K \times K\pi)$	$D_{s}^{+}D^{*0}\gamma$ $(K^{*0}K \times K\pi)$	0.01 ± 0.01
$D_{s1}^{+}D^{*-}$ $(K^{*0}K \times K\pi\pi^{0})$	$D_{s}^{+}D^{*0}\gamma$ $(K^{*0}K \times K\pi\pi^{0})$	0.00 ± 0.00
$D_{s1}^{+}D^{0}$ $(K^{*0}K \times K\pi\pi^{0})$		0.00 ± 0.00
$D_{s1}^{+}D^{*-}$ $(K^{*0}K \times K3\pi)$	$D_{s}^{+}D^{*0}\gamma$ $(K^{*0}K \times K3\pi)$	0.00 ± 0.00
$D_{s1}^{+}D^{0}$ $(K^{*0}K \times K3\pi)$		0.00 ± 0.00

Table 6.7: *Cross-feed matrix for reconstructed $D_s^+\gamma$ final states*

B Mode Generated	Final State Reconstructed	Efficiency (%)
$D_{s1}^{+}D^{-}$ $(\phi\pi \times K\pi\pi)$	$D_s^{*+}D^{-}\pi^0$ $(\phi\pi \times K\pi\pi)$	2.36 ± 1.89
$D_{s1}^{+}D^{-}$ $(K^{*0}K \times K\pi\pi)$	$D_s^{*+}D^{-}\pi^0$ $(K^{*0}K \times K\pi\pi)$	1.88 ± 1.85
$D_{s1}^{+}D^{*-}$ $(\phi\pi \times K\pi)$	$D_s^{*+}D^{*-}\pi^0$ $(\phi\pi \times K\pi)$	2.15 ± 1.79
$D_{s1}^{+}D^{*-}$ $(\phi\pi \times K\pi\pi^0)$	$D_s^{*+}D^{*-}\pi^0$ $(\phi\pi \times K\pi\pi^0)$	0.64 ± 0.62
$D_{s1}^{+}D^{*-}$ $(\phi\pi \times K3\pi)$	$D_s^{*+}D^{*-}\pi^0$ $(\phi\pi \times K3\pi)$	0.69 ± 0.68
$D_{s1}^{+}D^{*-}$ $(K^{*0}K \times K\pi)$	$D_s^{*+}D^{*-}\pi^0$ $(K^{*0}K \times K\pi)$	1.32 ± 1.30
$D_{s1}^{+}D^{*-}$ $(K^{*0}K \times K\pi\pi^0)$	$D_s^{*+}D^{*-}\pi^0$ $(K^{*0}K \times K\pi\pi^0)$	0.55 ± 0.55
$D_{s1}^{+}D^{*-}$ $(K^{*0}K \times K3\pi)$	$D_s^{*+}D^{*-}\pi^0$ $(K^{*0}K \times K3\pi)$	0.57 ± 0.57
$D_{s1}^{+}D^{0}$ $(\phi\pi \times K\pi)$	$D_s^{*+}D^{0}\pi^0$ $(\phi\pi \times K\pi)$	0.10 ± 0.08
$D_{s1}^{+}D^{0}$ $(\phi\pi \times K\pi\pi^0)$	$D_s^{*+}D^{0}\pi^0$ $(\phi\pi \times K\pi\pi^0)$	0.02 ± 0.02
$D_{s1}^{+}D^{0}$ $(\phi\pi \times K3\pi)$	$D_s^{*+}D^{0}\pi^0$ $(\phi\pi \times K3\pi)$	0.02 ± 0.02
$D_{s1}^{+}D^{0}$ $(K^{*0}K \times K\pi)$	$D_s^{*+}D^{0}\pi^0$ $(K^{*0}K \times K\pi)$	0.07 ± 0.07
$D_{s1}^{+}D^{0}$ $(K^{*0}K \times K\pi\pi^0)$	$D_s^{*+}D^{0}\pi^0$ $(K^{*0}K \times K\pi\pi^0)$	0.02 ± 0.02
$D_{s1}^{+}D^{0}$ $(K^{*0}K \times K3\pi)$	$D_s^{*+}D^{0}\pi^0$ $(K^{*0}K \times K3\pi)$	0.03 ± 0.03
$D_{s1}^{+}D^{*0}$ $(\phi\pi \times K\pi)$	$D_s^{*+}D^{*0}\pi^0$ $(\phi\pi \times K\pi)$	0.01 ± 0.01
$D_{s1}^{+}D^{*0}$ $(\phi\pi \times K\pi\pi^0)$	$D_s^{*+}D^{*0}\pi^0$ $(\phi\pi \times K\pi\pi^0)$	0.00 ± 0.00
$D_{s1}^{+}D^{*0}$ $(\phi\pi \times K3\pi)$	$D_s^{*+}D^{*0}\pi^0$ $(\phi\pi \times K3\pi)$	0.00 ± 0.00
$D_{s1}^{+}D^{*0}$ $(K^{*0}K \times K\pi)$	$D_s^{*+}D^{*0}\pi^0$ $(K^{*0}K \times K\pi)$	0.02 ± 0.02
$D_{s1}^{+}D^{*0}$ $(K^{*0}K \times K\pi\pi^0)$	$D_s^{*+}D^{*0}\pi^0$ $(K^{*0}K \times K\pi\pi^0)$	0.00 ± 0.00
$D_{s1}^{+}D^{*0}$ $(K^{*0}K \times K3\pi)$	$D_s^{*+}D^{*0}\pi^0$ $(K^{*0}K \times K3\pi)$	0.01 ± 0.01

Table 6.8: *Efficiencies for reconstructed $D_s^{*+}\pi^0$ final states*

B Mode Generated	Final State Reconstructed	Cross-Feed (%)
$D_{s1}^{+}D^{0}$ $(\phi\pi \times K\pi\pi^{0})$	$D_{s}^{*+}D^{-}\pi^{0}$ $(\phi\pi \times K\pi\pi)$	0.04 ± 0.03
$D_{s0}^{+}D^{*-}$ $(\phi\pi \times K\pi)$	$D_{s}^{*+}D^{0}\pi^{0}$ $(\phi\pi \times K\pi)$	0.01 ± 0.01
$D_{s0}^{+}D^{*0}$ $(\phi\pi \times K\pi)$		0.01 ± 0.01
$D_{s0}^{+}D^{*-}$ $(\phi\pi \times K\pi\pi^{0})$	$D_{s}^{*+}D^{0}\pi^{0}$ $(\phi\pi \times K\pi\pi^{0})$	0.01 ± 0.01
$D_{s0}^{+}D^{*0}$ $(\phi\pi \times K\pi\pi^{0})$		0.01 ± 0.01
$D_{s0}^{+}D^{*-}$ $(\phi\pi \times K3\pi)$	$D_{s}^{*+}D^{0}\pi^{0}$ $(\phi\pi \times K3\pi)$	0.01 ± 0.01
$D_{s0}^{+}D^{*0}$ $(\phi\pi \times K3\pi)$		0.00 ± 0.00
$D_{s0}^{+}D^{*-}$ $(K^{*0}K \times K\pi)$	$D_{s}^{*+}D^{0}\pi^{0}$ $(K^{*0}K \times K\pi)$	0.01 ± 0.01
$D_{s0}^{+}D^{*0}$ $(K^{*0}K \times K\pi)$		0.02 ± 0.02
$D_{s0}^{+}D^{*-}$ $(K^{*0}K \times K\pi\pi^{0})$	$D_{s}^{*+}D^{0}\pi^{0}$ $(K^{*0}K \times K\pi\pi^{0})$	0.01 ± 0.01
$D_{s0}^{+}D^{*0}$ $(K^{*0}K \times K\pi\pi^{0})$		0.01 ± 0.01
$D_{s0}^{+}D^{*-}$ $(K^{*0}K \times K3\pi)$	$D_{s}^{*+}D^{0}\pi^{0}$ $(K^{*0}K \times K3\pi)$	0.02 ± 0.02
$D_{s0}^{+}D^{*0}$ $(K^{*0}K \times K3\pi)$		0.01 ± 0.01
$D_{s1}^{+}D^{*-}$ $(\phi\pi \times K\pi)$	$D_{s}^{*+}D^{*0}\pi^{0}$ $(\phi\pi \times K\pi)$	0.01 ± 0.01
$D_{s1}^{+}D^{*-}$ $(\phi\pi \times K\pi\pi^{0})$	$D_{s}^{*+}D^{*0}\pi^{0}$ $(\phi\pi \times K\pi\pi^{0})$	0.00 ± 0.00
$D_{s1}^{+}D^{*-}$ $(\phi\pi \times K3\pi)$	$D_{s}^{*+}D^{*0}\pi^{0}$ $(\phi\pi \times K3\pi)$	0.00 ± 0.00
$D_{s1}^{+}D^{*-}$ $(K^{*0}K \times K\pi)$	$D_{s}^{*+}D^{*0}\pi^{0}$ $(K^{*0}K \times K\pi)$	0.01 ± 0.01
$D_{s1}^{+}D^{*-}$ $(K^{*0}K \times K\pi\pi^{0})$	$D_{s}^{*+}D^{*0}\pi^{0}$ $(K^{*0}K \times K\pi\pi^{0})$	0.00 ± 0.00
$D_{s1}^{+}D^{*-}$ $(K^{*0}K \times K3\pi)$	$D_{s}^{*+}D^{*0}\pi^{0}$ $(K^{*0}K \times K3\pi)$	0.00 ± 0.00

Table 6.9: *Cross-feed matrix for reconstructed $D_{s}^{*+}\pi^{0}$ final states*

There is found to be significant cross-feed present due to misreconstructed events, however corrections aren't required because this is accounted for in the branching fraction calculations.

6.3 Branching Fractions

Branching fractions are calculated for each of the 12 B decay modes listed below:

$D_{sJ}^{+}(2317) \to D_s^{+}\pi^0$ final states :

- $B^+ \to D_{sJ}^{+}(2317)\overline{D}^0$
- $B^+ \to D_{sJ}^{+}(2317)\overline{D}^{*0}$
- $B^0 \to D_{sJ}^{+}(2317)\overline{D}^{-}$
- $B^0 \to D_{sJ}^{+}(2317)\overline{D}^{*-}$

$D_{sJ}^{+}(2460) \to D_s^{+}\gamma$ final states :

- $B^+ \to D_{sJ}^{+}(2460)\overline{D}^0$
- $B^+ \to D_{sJ}^{+}(2460)\overline{D}^{*0}$
- $B^0 \to D_{sJ}^{+}(2460)\overline{D}^{-}$
- $B^0 \to D_{sJ}^{+}(2460)\overline{D}^{*-}$

$D_{sJ}^{+}(2460) \to D_s^{*+}\pi^0$ final states :

- $B^+ \to D_{sJ}^{+}(2460)\overline{D}^0$
- $B^+ \to D_{sJ}^{+}(2460)\overline{D}^{*0}$
- $B^0 \to D_{sJ}^{+}(2460)\overline{D}^{-}$

- $B^0 \to D_{sJ}^+(2460)\overline{D}^{*-}$

In order to calculate the branching fractions, it is necessary to first determine the event yields and to do this mass spectra are produced for each of the modes. Figures 6.6, 6.7 and 6.8 show the mass spectra for the $D_s^+\pi^0$, $D_s^+\gamma$ and $D_s^{*+}\pi^0$ final states passing the final selection criteria detailed in Chapter 5. These spectra are fitted with the sum of a Gaussian describing the signal and exponential describing the background. The mean and width of the Gaussian are kept fixed at 2318 MeV/c^2 and 8 MeV/c^2 for the $D_{sJ}(2317)^+$ and at 2460 MeV/c^2 and 12 MeV/c^2 for the $D_{sJ}^+(2460)$ due to the low statistics.

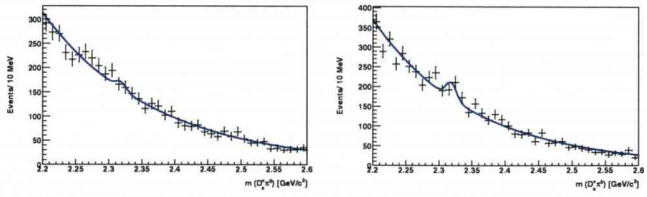

(a) $B \to D_s^+\pi^0 D^0$ (b) $B \to D_s^+\pi^0 D^-$

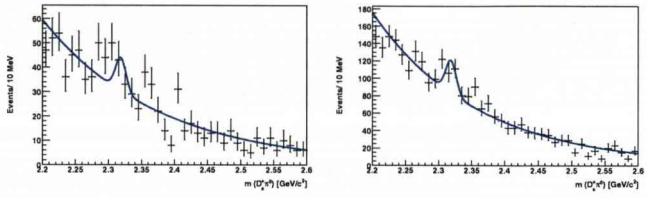

(c) $B \to D_s^+\pi^0 D^{*0}$ (d) $B \to D_s^+\pi^0 D^{*-}$

Figure 6.6: *$m(D_{sJ})$ spectra for $B \to D_s^+\pi^0\overline{D}$ modes*

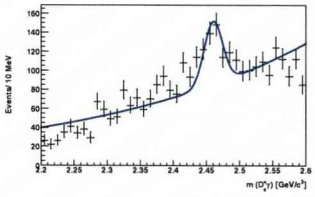

(a) $B \to D_s^+ \gamma D^0$

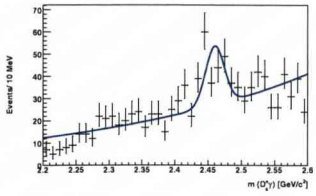

(b) $B \to D_s^+ \gamma D^-$

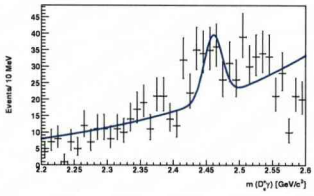

(c) $B \to D_s^+ \gamma D^{*0}$

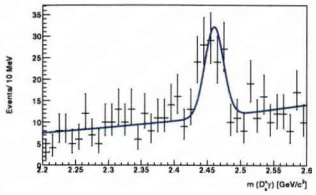

(d) $B \to D_s^+ \gamma D^{*-}$

Figure 6.7: *$m(D_{sJ})$ spectra for $B \to D_s^+ \gamma \overline{D}$ modes*

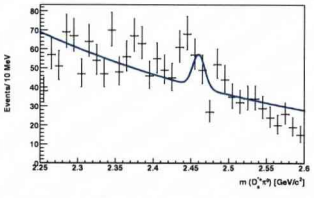

(a) $B \to D_s^{*+} \pi^0 D^0$

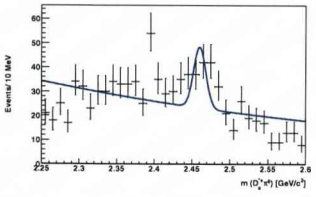

(b) $B \to D_s^{*+} \pi^0 D^-$

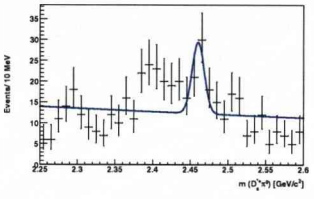

(c) $B \to D_s^{*+} \pi^0 D^{*0}$

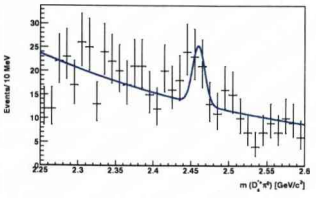

(d) $B \to D_s^{*+} \pi^0 D^{*-}$

Figure 6.8: *$m(D_{sJ})$ spectra for $B \to D_s^{*+} \pi^0 \overline{D}$ modes*

The number of events determined from the fitted D_{sJ} signal are shown in Table 6.10.

No.	Mode:	Number of Events	BR (10^{-3})
I	$B^+ \to D_{s0}^+ \overline{D}^0 (D_{s0}^+ \to D_s^+ \pi^0)$	$29.98 \pm 23.48 \pm 5.86$	$8.34 \pm 6.55 \pm 1.63^{-2.83}$
II	$B^0 \to D_{s0}^+ \overline{D}^- (D_{s0}^+ \to D_s^+ \pi^0)$	$82.27 \pm 25.46 \pm 16.07$	$0.93 \pm 0.31 \pm 0.18^{-0.20}$
III	$B^+ \to D_{s0}^+ \overline{D}^{*0} (D_{s0}^+ \to D_s^+ \pi^0)$	$27.53 \pm 11.84 \pm 5.38$	$50.38 \pm 22.04 \pm 9.84^{-22.4}$
IV	$B^0 \to D_{s0}^+ \overline{D}^{*-} (D_{s0}^+ \to D_s^+ \pi^0)$	$75.73 \pm 19.28 \pm 14.80$	$0.87 \pm 0.23 \pm 0.17^{-0.30}$
V	$B^+ \to D_{s0}^+ \overline{D}^0 (D_{s1}^+ \to D_s^+ \gamma)$	$232.80 \pm 28.53 \pm 45.49$	$91.53 \pm 12.88 \pm 17.88^{-30.85}$
VI	$B^0 \to D_{s0}^+ \overline{D}^- (D_{s1}^+ \to D_s^+ \gamma)$	$93.34 \pm 17.12 \pm 18.24$	$1.30 \pm 0.28 \pm 0.25^{-0.58}$
VII	$B^+ \to D_{s0}^+ \overline{D}^{*0} (D_{s1}^+ \to D_s^+ \gamma)$	$67.81 \pm 14.67 \pm 13.25$	$133.55 \pm 30.96 \pm 26.09^{-55.52}$
VIII	$B^0 \to D_{s0}^+ \overline{D}^{*-} (D_{s1}^+ \to D_s^+ \gamma)$	$73.10 \pm 12.72 \pm 14.28$	$1.14 \pm 0.21 \pm 0.22^{-0.44}$
IX	$B^+ \to D_{s0}^+ \overline{D}^0 (D_{s1}^+ \to D_s^{*+} \pi^0)$	$34.63 \pm 13.42 \pm 6.77$	$24.64 \pm 95.01 \pm 4.81^{-9.66}$
X	$B^0 \to D_{s0}^+ \overline{D}^- (D_{s1}^+ \to D_s^{*+} \pi^0)$	$50.32 \pm 12.18 \pm 9.83$	$1.5 \pm 0.40 \pm 0.29^{-0.94}$
XI	$B^+ \to D_{s0}^+ \overline{D}^{*0} (D_{s1}^+ \to D_s^{*+} \pi^0)$	$34.26 \pm 9.23 \pm 6.69$	$189.60 \pm 54.11 \pm 37.04^{-113.37}$
XII	$B^0 \to D_{s0}^+ \overline{D}^{*-} (D_{s1}^+ \to D_s^{*+} \pi^0)$	$24.54 \pm 8.77 \pm 4.79$	$1.05 \pm 0.38 \pm 0.21^{-0.42}$

Table 6.10: *Number of events and branching fractions for the 12 B decay modes. The errors shown are the statistical error, the systematic error due to the background fit and the systematic error due to the difference in width between data and Monte-Carlo*

The branching fractions are calculated in a similar fashion to the two-body branching fractions and are given by the following formulae:

$$BR(B \to D_{sJ}D^{(*)}) = \frac{N_{obs}}{N_{B\overline{B}} \times \sum_{jk} BR(D^{(*)} \to j)BR(D_s^{(*)} \to k) \times \varepsilon_{jk}} \tag{6.2}$$

where

$$BR(B \to D_{sJ}D^{(*)}) = \begin{cases} BR(B \to D_{s0}D^{(*)}) \times BR(D_{sJ} \to D_s^+\pi^0) \\ BR(B \to D_{s1}D^{(*)}) \times BR(D_{s1} \to D_s^+\gamma) \\ BR(B \to D_{s1}D^{(*)}) \times BR(D_{s1} \to D_s^{*+}\pi^0) \end{cases}$$

Where N_{obs} is the number of observed events of the decay mode, $N_{B\overline{B}}$ is the total number of $B\overline{B}$ events, $BR(D^{(*)} \to j)$ and $BR(D_s^{(*)} \to k)$ are the daughter branching fractions of the $D^{(*)}$ and $D_s^{(*)}$ and are summed over all decay products, j and k, and ε_{jk} are the efficiencies of the submodes as calculated in Section 6.2.3. The calculated branching fractions are shown in Table 6.10 along with the number of events for each of the modes. The errors shown in the table are the statistical error, the systematic error due to background fitting and the systematic error due to the variation in width of Monte-Carlo and Data. The calculated branching fractions from the previous analysis are shown in Table 6.11 [58].

No.	Mode:	Number of Events	BR (10^{-3})
I	$B^+ \to D^+_{s0}\overline{D}^0(D^+_{s0} \to D^+_s\pi^0)$	32.7 ± 10.8	1.04 ± 0.35
II	$B^0 \to D^+_{s0}\overline{D}^-(D^+_{s0} \to D^+_s\pi^0)$	34.7 ± 8.0	1.80 ± 0.42
III	$B^+ \to D^+_{s0}\overline{D}^{*0}(D^+_{s0} \to D^+_s\pi^0)$	17.6 ± 6.8	0.86 ± 0.56
IV	$B^0 \to D^+_{s0}\overline{D}^{*-}(D^+_{s0} \to D^+_s\pi^0)$	23.5 ± 6.1	1.50 ± 0.39
V	$B^+ \to D^+_{s0}\overline{D}^0(D^+_{s1} \to D^+_s\gamma)$	29.0 ± 6.8	2.73 ± 0.70
VI	$B^0 \to D^+_{s0}\overline{D}^-(D^+_{s1} \to D^+_s\gamma)$	17.4 ± 5.1	2.80 ± 0.83
VII	$B^+ \to D^+_{s0}\overline{D}^{*0}(D^+_{s1} \to D^+_s\gamma)$	30.5 ± 6.4	7.59 ± 1.73
VIII	$B^0 \to D^+_{s0}\overline{D}^{*-}(D^+_{s1} \to D^+_s\gamma)$	26.5 ± 5.7	5.50 ± 1.18
IX	$B^+ \to D^+_{s0}\overline{D}^0(D^+_{s1} \to D^{*+}_s\pi^0)$	31.9 ± 9.0	0.61 ± 0.18
X	$B^0 \to D^+_{s0}\overline{D}^-(D^+_{s1} \to D^{*+}_s\pi^0)$	24.8 ± 6.5	0.76 ± 0.20
XI	$B^+ \to D^+_{s0}\overline{D}^{*0}(D^+_{s1} \to D^{*+}_s\pi^0)$	34.6 ± 7.6	1.37 ± 0.37
XII	$B^0 \to D^+_{s0}\overline{D}^{*-}(D^+_{s1} \to D^{*+}_s\pi^0)$	53.0 ± 7.8	2.25 ± 0.33

Table 6.11: *Number of events and branching fractions from the previous D_{sJ} analysis*

From the measured branching fractions for $B \to D^+_{sJ}(2460)\overline{D}^*$ in the $D^+_s\gamma$ and $D^{*+}_s\pi^0$ final states a calculation of $\mathcal{B}(D^+_{sJ}(2460) \to D_s\gamma)/\mathcal{B}(D^+_{sJ}(2460) \to D^*_s\pi^0)$ is made:

$$\frac{\mathcal{B}(D^+_{sJ}(2460) \to D_s\gamma)}{\mathcal{B}(D^+_{sJ}(2460) \to D^*_s\pi^0)} = 1.049 \pm 0.551 \tag{6.3}$$

6.4 $\mathbf{D_{sJ}}$ Helicity Analysis

In order to obtain information about the quantum numbers of the D_{sJ} particles, specifically their spin J, an investigation of the helicity angles is undertaken. The helicity angle, θ_h is defined as the angle between the D_{sJ} momentum in the B meson rest frame and the D_s momentum in the D_{sJ} rest frame. The helicity distribution can provide information on the D_{sJ} spin because the decay $B \to D_{sJ}D$ is a $0^- \to 0^- J^P$ transition and therefore the resulting D_{sJ} is polarised.

6.4.1 $\mathbf{D^+_{sJ}(2317)}$

The $\mathrm{D^+_{sJ}}(2317)$ helicity analysis is performed looking at the following processes:

$$B^+ \to D^0 D^+_{sJ}(2317) \qquad \text{where} \quad D^+_{sJ}(2317) \to D_s\pi^0$$

$$B^+ \to D^{*0} D^+_{sJ}(2317) \qquad \text{where} \quad D^+_{sJ}(2317) \to D_s\pi^0$$

$$B^0 \to D^- D^+_{sJ}(2317) \qquad \text{where} \quad D^+_{sJ}(2317) \to D_s\pi^0$$

$$B^0 \to D^{*-} D^+_{sJ}(2317) \qquad \text{where} \quad D^+_{sJ}(2317) \to D_s\pi^0$$

The m($D_s\pi^0$) signal for those final states in data is shown in Figure 6.9 and a Gaussian fit returns the following results:

$$m(D_{sJ}) = 2308.2 \pm 5.26 \text{ MeV/c}^2$$
$$\sigma_m = 21.72 \pm 11.56 \text{ MeV/c}^2 \tag{6.4}$$

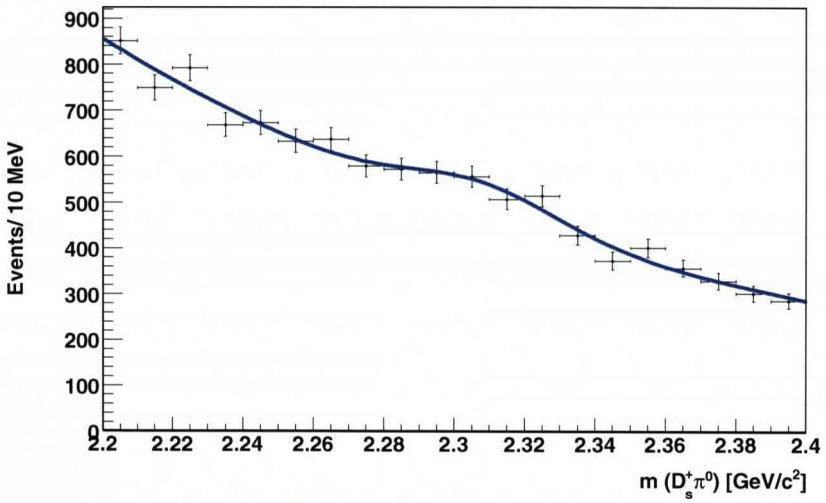

Figure 6.9: *$m(D_s\pi^0)$ spectra for data*

Fits to the m($D_s\pi^0$) distribution for data are then performed for five different $cos(\theta_h)$ regions in order to extract the angular information. The $cos(\theta_h)$ regions are as follows:

- $-1.0 < cos(\theta_h) < -0.6$
- $-0.6 < cos(\theta_h) < -0.2$
- $-0.2 < cos(\theta_h) < 0.2$
- $0.2 < cos(\theta_h) < 0.6$
- $0.6 < cos(\theta_h) < 1.0$

Plots of the m($D_s\pi^0$) distributions are shown in Figure 6.10. The distributions are fitted with a Gaussian with fixed mean and fixed width, given by Equation 6.4. The number of signal events in the peak from the fits are shown in Table 6.12.

$cos(\theta_h)$	N_{signal}
$-1.0 < cos(\theta_h) < -0.6$	$0.11 \pm 5.27 \pm 0.02$
$-0.6 < cos(\theta_h) < -0.2$	$11.47 \pm 6.87 \pm 2.24$
$-0.2 < cos(\theta_h) < 0.2$	$24.35 \pm 11.09 \pm 4.76$
$0.2 < cos(\theta_h) < 0.6$	$21.01 \pm 15.22 \pm 4.11$
$0.6 < cos(\theta_h) < 1.0$	$21.27 \pm 20.00 \pm 4.16$

Table 6.12: *Number of Signal events in the peak of m($D_s\pi^0$) distributions for different helicities. The errors shown are the statistical error and the systematic error due to the background fit*

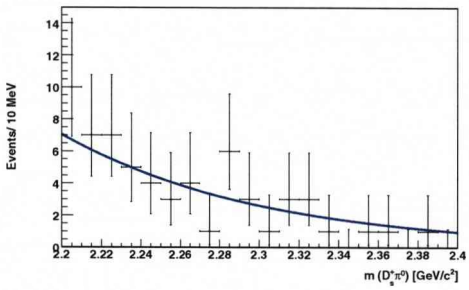

(a) $-1.0 < cos(\theta_h) < -0.6$

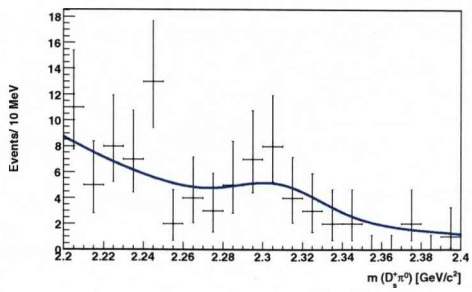

(b) $-0.6 < cos(\theta_h) < -0.2$

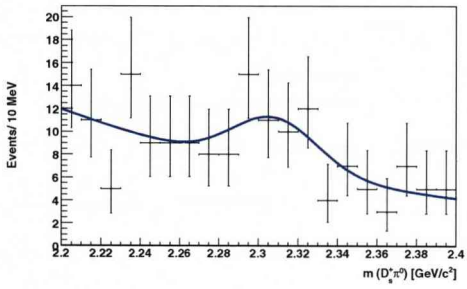

(c) $-0.2 < cos(\theta_h) < 0.2$

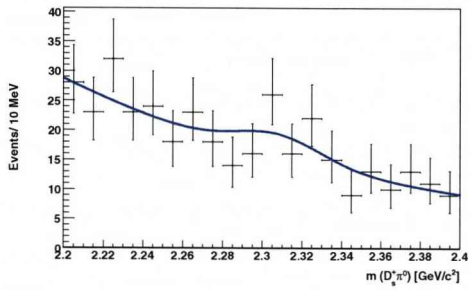

(d) $0.2 < cos(\theta_h) < 0.6$

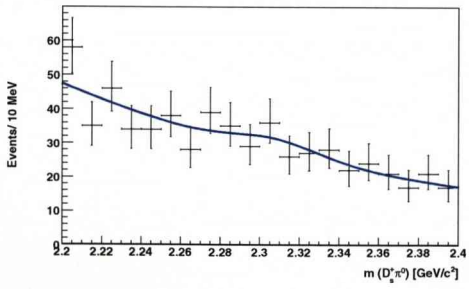

(e) $0.6 < cos(\theta_h) < 1.0$

Figure 6.10: *$m(D_s\pi^0)$ distributions for different helicities*

Using the results from the m($D_s\pi^0$) fits, helicity distributions are produced and are shown in Figure 6.11. The helicity distributions are fitted with the analytical expectations for the $J = 0$ spin hypothesis (a) and for the $J = 1$ spin hypothesis (b). The χ^2 obtained from the fits are shown in table 6.13. There is found to be good agreement for both the $J = 0$ and $J = 1$ spin hypotheses.

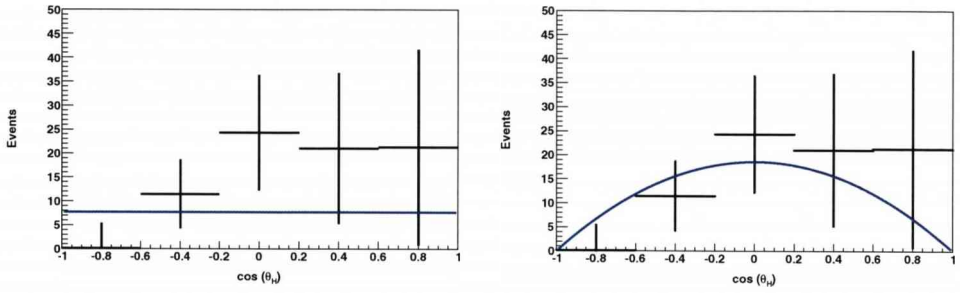

(a) $J = 0$ *spin hypothesis* **(b)** $J = 1$ *spin hypothesis*

Figure 6.11: *Helicity distributions for* $D_{sJ}(2317)$ *with* $D_s\pi^0$ *final state in data*

Spin Hypothesis	$\chi^2/n.d.f$
$J = 0$	5.40/4
$J = 1$	1.78/4

Table 6.13: χ^2 *results obtained from fitting the* $D_s\pi^0$ *helicity distributions with the spin hypotheses in data*

Figure 6.12 shows the helicity distributions for the $D_s\pi^0$ final states using signal Monte-Carlo, including both the $J = 0$ spin hypothesis (a) and the $J = 1$ spin

hypothesis (b). The χ^2 obtained from the fits are shown in table 6.14. In the Monte-Carlo generation the $D_s\pi^0$ final state is assumed to have spin $J = 0$ and this suggests that the analysis is not sensitive to the helicity of the $D_{sJ}(2317)$.

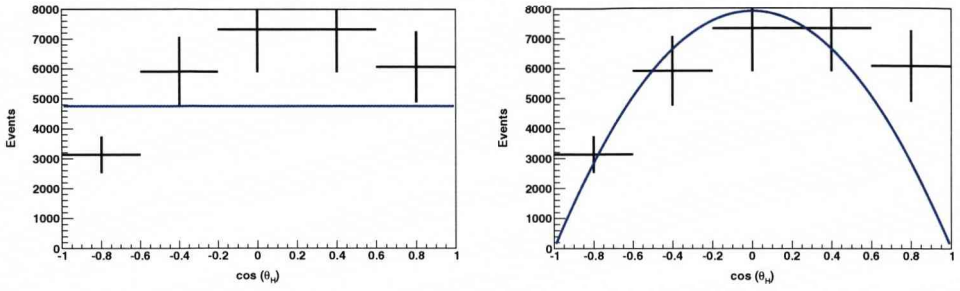

(a) $J = 0$ *spin hypothesis* **(b)** $J = 1$ *spin hypothesis*

Figure 6.12: *Helicity distributions for* $D_{sJ}(2317)$ *with* $D_s\pi^0$ *final state using signal Monte-Carlo*

Spin Hypothesis	$\chi^2/n.d.f$
$J = 0$	15.60/4
$J = 1$	1.81/4

Table 6.14: χ^2 *results obtained from fitting the* $D_s\pi^0$ *helicity distributions, produced by signal Monte-Carlo, with the spin hypotheses*

6.4.2 $\mathbf{D_{sJ}^+(2460)}$

The $D_{sJ}^+(2460)$ helicity analysis is performed in two stages, firstly looking at the $D_{s1}^+ \to D_s^+\gamma$ final states and then looking at the $D_{s1}^+ \to D_s^{*+}\pi^0$ final states. A

$D_{sJ}(2460)$ spin $J = 0$ is excluded by parity and angular momentum conservation so the spin $J = 1$ and spin $J = 2$ hypotheses are tested for the $D_{sJ}(2460)$.

$\mathbf{D^+_{sJ}(2460) \to D^+_s\gamma}$

The analysis looks at the following processes:

$$B^+ \to D^0 D^+_{sJ}(2460) \qquad \text{where} \quad D^+_{sJ}(2460) \to D_s\gamma$$

$$B^+ \to D^{*0} D^+_{sJ}(2460) \qquad \text{where} \quad D^+_{sJ}(2460) \to D_s\gamma$$

$$B^0 \to D^- D^+_{sJ}(2460) \qquad \text{where} \quad D^+_{sJ}(2460) \to D_s\gamma$$

$$B^0 \to D^{*-} D^+_{sJ}(2460) \qquad \text{where} \quad D^+_{sJ}(2460) \to D_s\gamma$$

The m($D_s\gamma$) signal for those final states in data is shown in Figure 6.13 and a Gaussian plus polynomial fit returns the following results:

$$m(D_{sJ}) = 2459.1 \pm 3.34 \text{ MeV/c}^2$$

$$\sigma_m = 25.87 \pm 6.42 \text{ MeV/c}^2 \tag{6.5}$$

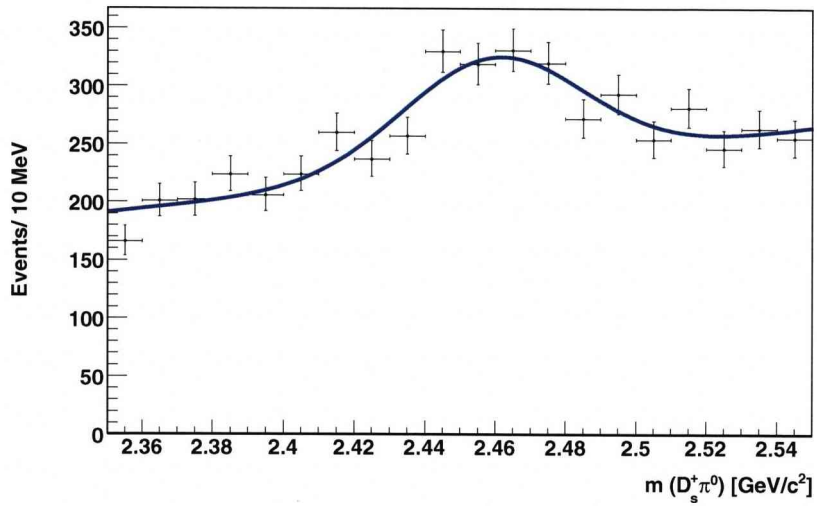

Figure 6.13: *$m(D_s\gamma)$ spectra for data*

Fits to the m$(D_s\gamma)$ distribution for data are then performed for five different $cos(\theta_h)$ regions in order to extract the angular information. The $cos(\theta_h)$ regions are the same as those defined previously. Plots of the m$(D_s\gamma)$ distributions are shown in Figure 6.14. The distributions are fitted with a Gaussian with fixed mean and fixed width, given by Equation 6.5. The number of signal events in the peak from the fits are shown in Table 6.15.

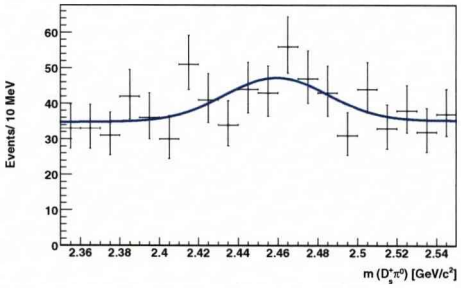

(a) $-1.0 < cos(\theta_h) < -0.6$

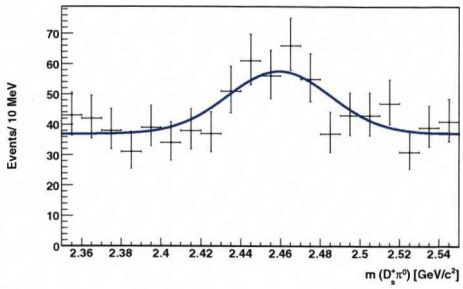

(b) $-0.6 < cos(\theta_h) < -0.2$

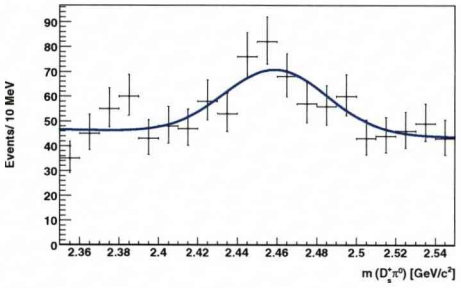

(c) $-0.2 < cos(\theta_h) < 0.2$

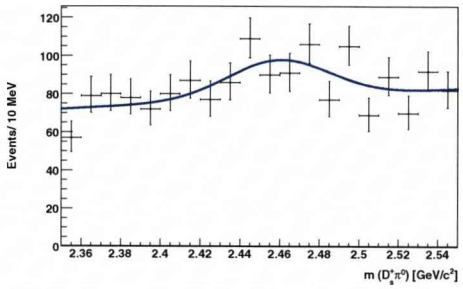

(d) $0.2 < cos(\theta_h) < 0.6$

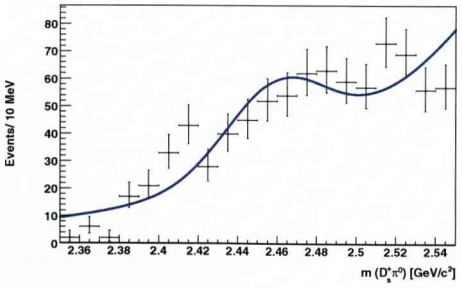

(e) $0.6 < cos(\theta_h) < 1.0$

Figure 6.14: *$m(D_s\gamma)$ distributions for different helicities*

$cos(\theta_h)$	N_{signal}
$-1.0 < cos(\theta_h) < -0.6$	$79.28 \pm 27.10 \pm 15.49$
$-0.6 < cos(\theta_h) < -0.2$	$133.00 \pm 28.58 \pm 25.99$
$-0.2 < cos(\theta_h) < 0.2$	$167.36 \pm 31.90 \pm 32.70$
$0.2 < cos(\theta_h) < 0.6$	$129.89 \pm 39.29 \pm 25.38$
$0.6 < cos(\theta_h) < 1.0$	$193.19 \pm 30.68 \pm 37.75$

Table 6.15: *Number of Signal events in the peak of $m(D_s\gamma)$ distributions for different helicities. The errors shown are the statistical error and the systematic error due to the background fit*

Using the results from the m($D_s\gamma$) fits, helicity distributions are produced and are shown in Figure 6.15. The helicity distributions are fitted with the analytical expectations for the $J = 1$ spin hypothesis (a) and for the $J = 2$ spin hypothesis (b). The χ^2 obtained from the fits are shown in table 6.16. There is found to be good agreement for the $J = 1$ spin hypothesis whilst the $J = 2$ spin hypotheses is excluded.

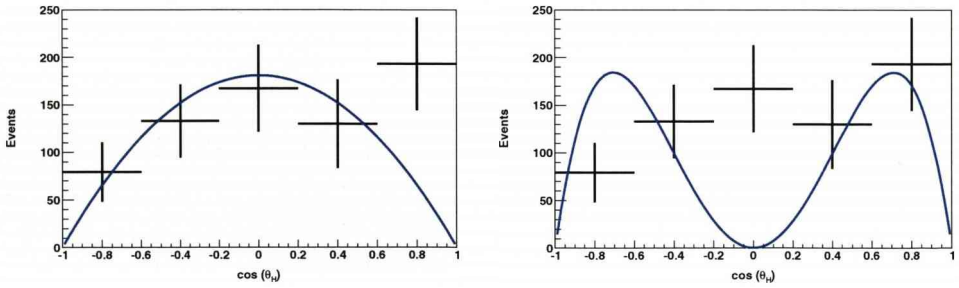

(a) $J = 1$ *spin hypothesis* **(b)** $J = 2$ *spin hypothesis*

Figure 6.15: *Helicity distributions for $D_{sJ}(2460)$ with $D_s\gamma$ final state*

Spin Hypothesis	$\chi^2/n.d.f$
$J = 1$	3.32/4
$J = 2$	15.30/4

Table 6.16: χ^2 *results obtained from fitting the* $D_s\gamma$ *helicity distributions with the spin hypotheses*

Figure 6.16 shows the helicity distributions for the $D_s\gamma$ final states using signal Monte-Carlo, including both the $J = 1$ spin hypothesis (a) and the $J = 2$ spin hypothesis (b). The χ^2 obtained from the fits are shown in table 6.17. In the signal Monte-Carlo generation the $D_s\gamma$ final state is assumed to have spin $J = 1$ and this suggests that the analysis is sensitive to the helicity of the $D_{sJ}(2460)$.

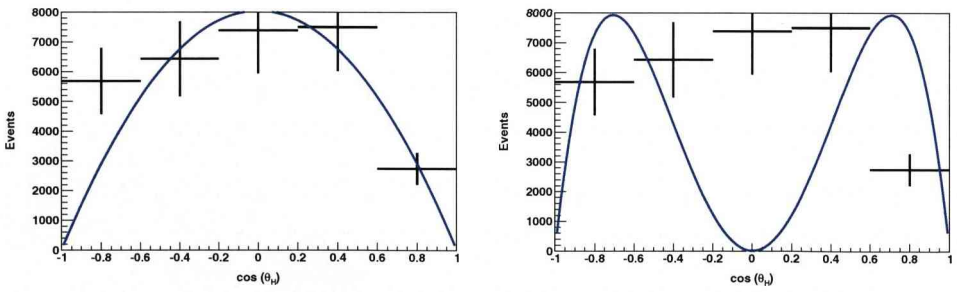

(a) $J = 1$ *spin hypothesis* **(b)** $J = 2$ *spin hypothesis*

Figure 6.16: *Helicity distributions for* $D_{sJ}(2460)$ *with* $D_s\gamma$ *final state using signal Monte-Carlo*

Spin Hypothesis	$\chi^2/n.d.f$
$J = 1$	1.37/4
$J = 2$	29.96/4

Table 6.17: χ^2 *results obtained from fitting the* $D_s\gamma$ *helicity distributions, produced by signal Monte-Carlo, with the spin hypotheses*

$\mathbf{D_{sJ}^+(2460) \to D_s^{*+}\pi^0}$

The analysis looks at the following processes:

$$B^+ \to D^0 D_{sJ}^+(2460) \quad \text{where} \quad D_{sJ}^+(2460) \to D_s^*\pi^0$$

$$B^+ \to D^{*0} D_{sJ}^+(2460) \quad \text{where} \quad D_{sJ}^+(2460) \to D_s^*\pi^0$$

$$B^0 \to D^- D_{sJ}^+(2460) \quad \text{where} \quad D_{sJ}^+(2460) \to D_s^*\pi^0$$

$$B^0 \to D^{*-} D_{sJ}^+(2460) \quad \text{where} \quad D_{sJ}^+(2460) \to D_s^*\pi^0$$

The m($D_s\pi^0$) signal for those final states in data is shown in Figure 6.17 and a Gaussian fit returns the following results:

$$m(D_{sJ}) = 2448.5 \pm 4.34 \text{ MeV/c}^2$$

$$\sigma_m = 33.15 \pm 8.26 \text{ MeV/c}^2 \tag{6.6}$$

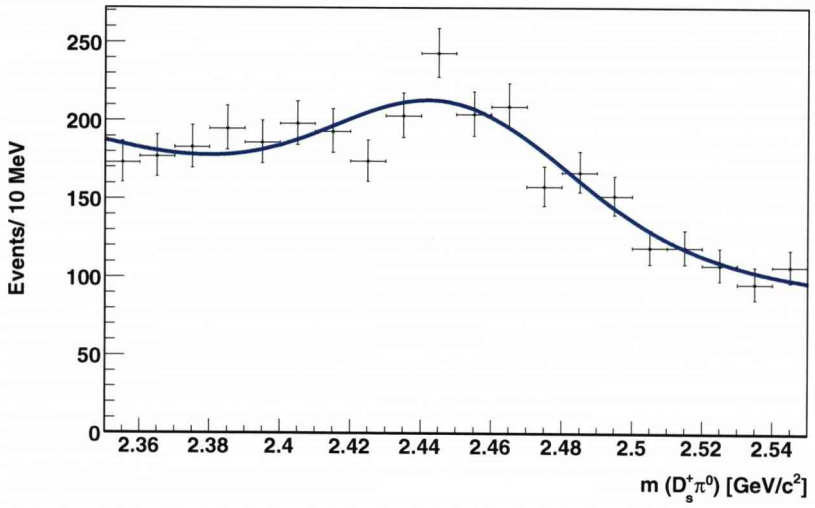

Figure 6.17: $m(D_s^*\pi^0)$ *spectra for data*

Fits to the m$(D_s^*\pi^0)$ distribution for data are then performed for five different $cos(\theta_h)$ regions in order to extract the angular information. The $cos(\theta_h)$ regions are the same as those defined previously. Plots of the m$(D_s^*\pi^0)$ distributions are shown in Figure 6.18. The distributions are fitted with a Gaussian with fixed mean and fixed width, given by Equation 6.6. The number of signal events in the peak from the fits are shown in Table 6.18.

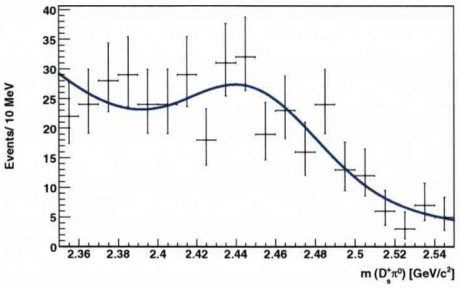

(a) $-1.0 < cos(\theta_h) < -0.6$

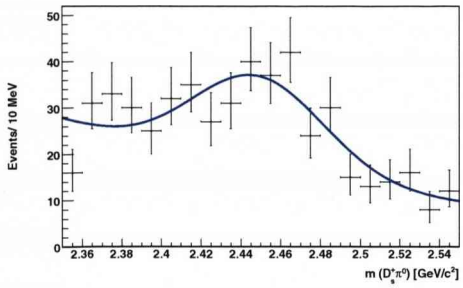

(b) $-0.6 < cos(\theta_h) < -0.2$

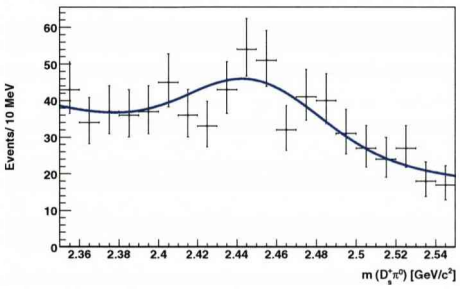

(c) $-0.2 < cos(\theta_h) < 0.2$

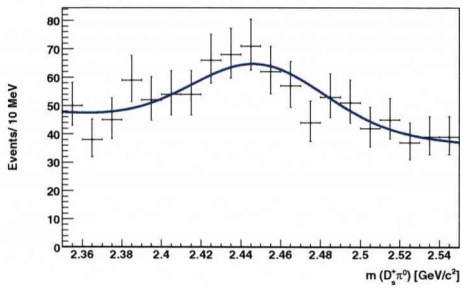

(d) $0.2 < cos(\theta_h) < 0.6$

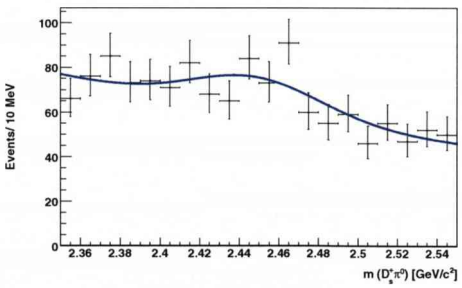

(e) $0.6 < cos(\theta_h) < 1.0$

Figure 6.18: *$m(D_s^*\pi^0)$ distributions for different helicities*

$cos(\theta_h)$	N_{signal}
$-1.0 < cos(\theta_h) < -0.6$	$127.83 \pm 24.85 \pm 24.98$
$-0.6 < cos(\theta_h) < -0.2$	$169.39 \pm 27.89 \pm 33.10$
$-0.2 < cos(\theta_h) < 0.2$	$151.86 \pm 32.54 \pm 29.67$
$0.2 < cos(\theta_h) < 0.6$	$187.87 \pm 39.08 \pm 36.71$
$0.6 < cos(\theta_h) < 1.0$	$134.27 \pm 43.19 \pm 26.23$

Table 6.18: *Number of Signal events in the peak of $m(D_s^*\pi^0)$ distributions for different helicities. The errors shown are the statistical error and the systematic error due to the background fit*

Using the results from the $m(D_s^*\pi^0)$ fits, helicity distributions are produced and are shown in Figure 6.19. The helicity distributions are fitted with the analytical expectations for the $J = 1$ spin hypothesis (a) and for the $J = 2$ spin hypothesis (b). The χ^2 obtained from the fits are shown in table 6.19. There is found to be good agreement for the $J = 1$ spin hypothesis and the $J = 2$ spin hypotheses is excluded.

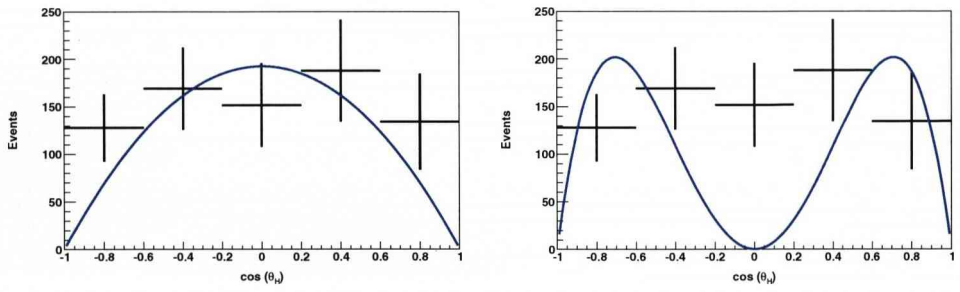

(a) $J = 1$ *spin hypothesis* **(b)** $J = 2$ *spin hypothesis*

Figure 6.19: *Helicity distributions for $D_{sJ}(2460)$ with $D_s^*\pi^0$ final state*

Spin Hypothesis	$\chi^2/n.d.f$
$J = 1$	2.40/4
$J = 2$	13.74/4

Table 6.19: χ^2 *results obtained from fitting the* $D_s^*\pi^0$ *helicity distributions with the spin hypotheses*

Figure 6.20 shows the helicity distributions for the $D_s^*\pi^0$ final states using signal Monte-Carlo, including both the $J = 1$ spin hypothesis (a) and the $J = 2$ spin hypothesis (b). The χ^2 obtained from the fits are shown in table 6.20. In the signal Monte-Carlo generation the $D_s^*\pi^0$ final state is assumed to have spin $J = 1$ and this suggests that the analysis is sensitive to the helicity of the $D_{sJ}(2460)$.

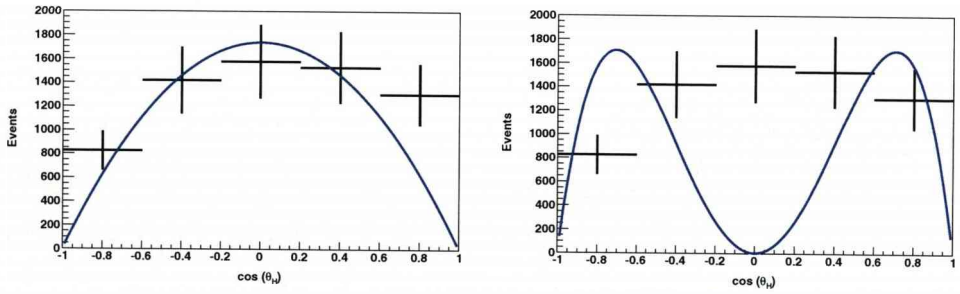

(a) $J = 1$ *spin hypothesis* **(b)** $J = 2$ *spin hypothesis*

Figure 6.20: *Helicity distributions for* $D_{sJ}(2460)$ *with* $D_s^*\pi^0$ *final state using Monte-Carlo*

Spin Hypothesis	$\chi^2/n.d.f$
$J = 1$	1.64/4
$J = 2$	28.20/4

Table 6.20: χ^2 *results obtained from fitting the* $D_s^*\pi^0$ *helicity distributions, produced by signal Monte-Carlo, with the spin hypotheses*

Chapter 7

Conclusions

The analysis presented in this thesis describes the study of $B \to D_{sJ}^{+} D^{(*)}$ decays using the *BABAR* experiment with the aim of studying the physical properties of the $D_{sJ}^{+}(2317)$ and $D_{sJ}^{+}(2460)$ mesons. The data produced during Runs 1-5, corresponding to 382.9 million $B\overline{B}$ pairs, was used to analyse the spin of the D_{sJ}^{+} particles and to calculate the branching fractions of the corresponding B decays.

Mass distributions of the $D_{sJ}^{+}(2317)$ and $D_{sJ}^{+}(2460)$ showed visible signals in both Monte-Carlo and data. A study of the two-body decays $B \to D_{s}^{(*)} D^{(*)}$ was undertaken to act as a cross check to the analysis procedure due to the similarity of final states. The same framework was used in this study so that it could act as a verification of the results produced by the $B \to D_{sJ}^{+} D^{(*)}$ analysis. Branching

fractions calculated for this two-body analysis are shown in Table 6.3 and compared graphically to PDG values in Figure 6.3. Most of the decay modes, aside from those with higher backgrounds, had branching fractions which fell within 3σ of the PDG values. This suggests that the analysis procedure is valid, although there are high backgrounds in some modes.

The branching fractions of the decays $B \to D_{sJ}^{+} D^{(*)}$ are calculated and shown in Table 6.10. When compared to previous branching fraction calculations performed by *BABAR* the branching fractions for the modes containing D^{-} and D^{*-} final states were found to be similar. The branching fractions for the modes containing D^{-} and D^{*-} were found to be larger and the reason for this is due to poor background separation for those modes.

A helicity analysis was performed on all three final states $D_s^{+}\pi^0$, $D_s^{+}\gamma$ and $D_s^{*+}\pi^0$ and distributions of the helicity angles were compared to those produced by different spin hypotheses. The $D_s^{+}\pi^0$ final state was compared to the $J = 0$ and $J = 1$ spin hypotheses and both were found to be consistent. The $D_s^{+}\gamma$ final state was compared to the $J = 1$ and $J = 2$ spin hypotheses and the $J = 1$ spin hypothesis was found to be consistent with the results, whilst the $J = 2$ hypothesis was excluded. The $D_s^{*+}\pi^0$ final state was also compared to the $J = 1$ and $J = 2$ spin hypotheses and the $J = 1$ spin hypothesis was again found to be consistent with the results with the $J = 2$ spin hypothesis being excluded.

Bibliography

[1] A. D. Sakharov, Violation of CP invariance, C asymmetry and baryon asymmetry of the universe. *Pisma Zh. Eksp. Teor. Fiz.* 5:32-35 (1967)

[2] S. L. Glashow, Partial symmetries of weak interactions. *Nuc. Phys.* 22:579-588 (1961)

[3] S. Weinberg, A model of leptons. *Phys. Rev. Lett.* 19:1264-1266 (1967)

[4] A. Salam, Weak an electromagnetic interactions. Svartholm: Elementary Particle Theory, Proceedings of Nobel Symposium, Stockholm. (1968)

[5] T.D. Lee and C.N Yang, Question of parity conservation in weak interactions. *Phys. Rev.* 104:254-258 (1956)

[6] C.S. Wu *et al*, Experimental test of parity conservation in β decays. *Phys. Rev.* 105:1413-1414 (1957)

[7] B.L. Ioffe *et al*, *Sov. Phys. JETP.* 5:237 (1957)

[8] J.H. Christenson *et al*, Evidence for the 2π decay of the K_2^0 meson. *Phys. Rev. Lett.* 13:138-140 (1964)

[9] N. Cabibbo, Unitarity symmetry and leptonic decays. *Phys. Rev. Lett.* 10:531-532 (1963)

[10] K. Hagiwara *et al*, Review of Particle Physics. *Phys. Rev.* D66:010001 (2002)

[11] M. Kobayashi and T. Maskawa, CP violation in the renormalisable theory of weak interaction. *Prog. Theor. Phys.* 49:652-657 (1973)

[12] L. M. Lederman, The Discovery of the upsilon, bottom quark and B mesons. Lecture given at 3rd International symposium on the History of Particle Physics: The rise of the standard model, Stanford, CA. 24 -27 June (1992)

[13] M. L. Perl, Review of heavy lepton production in e^+e^- annihilation. Invited talk presented at International Symposium on Lepton and Photon Interactions at High Energies, Hamburg. 25 -31 August (1977)

[14] L. Wolfenstein, Parameterisation of the Kobayashi-Maskawa matrix. *Phys. Rev. Lett.* 51:1945 (1983)

[15] C. Jarlskog, Commutator of the quark mass matrices in the standard electroweak model and a measure of maximal CP violation. *Phys. Rev. Lett.* 55:1039 (1985)

[16] S. Eidelman *et al*, Review of particle physics. *Phys. Lett.* B592:1 (2004)

[17] V. Fanti *et al*, A new measurement of direct CP violation in two pion decays of the neutral kaon. *Phys. Lett.* B465:335-348 (1999)

[18] A. Alavi-Harati *et al*, Observation of direct CP violation in $K_{S,L} \to \pi\pi$ decays. *Phys. Rev. Lett.* 83:22 (1999)

[19] B. Aubert *et al*, Observation of direct CP violation in $B^0 \to c\bar{c}K^{*0}$ decays *Phys. Rev. Lett.* 93:131801 (2004)

[20] B. Aubert *et al*, Observation of a narrow meson state decaying to $D_s^+\pi^0$ at a mass of 2.32 GeV/c^2. *Phys. Rev. Lett.* 90:242001 (2003)

[21] D. Besson *et al*, Observation of a narrow resonance of mass 2.32 GeV/c^2 decaying to D_s^{*+} and confirmation of the $D_{sJ}(2317)$ state. *Phys. Rev.* D68:032002 (2003)

[22] K. Abe *et al*, Measurement of the D_{sJ} resonance properties. *Phys. Rev. Lett.* 92:012002 (2004)

[23] B. Aubert *et al*, Observation of a narrow meson state decaying to $D_s^+\pi^0\gamma$ at a mass of 2.458 GeV/c^2. *Phys. Rev.* D69:031101 (2004)

[24] N. Isgur and M. B. Wise, Spectroscopy with heavy quark symmetry. *Phys. Rev. Lett.* 66:1130 (1991)

[25] S. Godfrey and R. Kokoski, The properties of p wave mesons with one heavy quark. *Phys. Rev.* D43:1679 (1991)

[26] S. Godfrey and N. Isgur, Mesons in relativized quark model with chromodynamics. *Phys. Rev.* D32:189 (1985)

[27] R. N. Cahn and J. D. Jackson, Split orbit and tensor forces in heavy-quark light-quark mesons: Implications of the new D_s state at 2.32 GeV. *Phys. Rev.* D68:037502 (2003)

[28] T. Barnes, F. E. Close and H. J. Lipkin, Implications of a DK molecule at 2.32 GeV. *Phys. Rev.* D68:054006 (2003)

[29] E. van Beveren and G. Rupp, Observed $D_s(2317)$ and tentative D(2100-2300) as the charmed cousins of the light scalar nonet. *Phys. Rev. Lett.* 91:012003 (2003)

[30] H. Y. Cheng and W. S. Hou, B decays as spectroscope for charmed four-quark states. *Phys. Lett.* B566:193 (2003)

[31] K. Terasaki, *BABAR* resonance as a new window for hadron physics. *Phys. Rev.* D68:011501 (2003)

[32] H. J. Lipkin, New predictions for multiquark hadron masses. *Phys. Lett.* B580:50 (2004)

[33] W. A. Bardeen, E. J. Eichten and C. T. Hill, Chiral multiplets of heavy-light mesons. *Phys. Rev.* D68:054024 (2003)

[34] M. A. Nowak, M. Rho and I. Zahed, Chiral effective action with heavy quark symmetry. *Phys. Rev.* D48:4370 (1993)

[35] E. E. Kolomeitsev and M. F. M. Lutz, On heavy-light meson resonances and chiral symmetry. *Phys. lett.* B582:39 (2004)

[36] A. P. Szczepaniak, Description of the $D_s^*(2320)$ resonance as a $D\pi$ atom. *Phys. lett.* B567:23 (2003)

[37] A. A. Arkhipov, Charmed and Charmed-strange mesons in Kaluza-Klein picture. *arXiv:hep-ph/0306237* (2003)

[38] T. E. Browder, S. Pakvasa and A. A. Petrov, Comment on the new $D_s^{(*)+}\pi^0$ resonance. *Phys. Lett.* B578:363 (2004)

[39] T. D. Cohen, B. A. Gelman and S. Nussinov, New near-threshold mesons. *Phys. Lett.* B578:359 (2004)

[40] W. A. Bardeen and C. T. Hill, Chiral dynamics and heavy quark symmetry in a solvable toy field theoretic model. *Phys. Rev.* D49:409 (1994)

[41] Y. B. Dai, C. S. Huang, C. Liu and S. L. Zhu, Understanding the $D_{sJ}(2317)$ and $D_{sJ}(2460)$ with sum rules in HQET. *Phys. Rev.* D68:114011 (2003)

[42] A. Deandrea, G. Nardulli and A. D. Polosa, On the mass of the $D_s(0^+, 1^+$ system. *Phys. Rev.* D68:097501 (2003)

[43] A. Dougall, R. D. Kenway, C. M. Maynard and C. McNeile, The spectrum of D_s mesons from lattice QCD. *Phys. Lett.* B569:41 (2003)

[44] M. Sadzikowski, The masses of the $D^*_{sJ}(2317)$ and $D^*_{sJ}(2463)$ in the MIT bag model. *Phys. Lett.* B579:39 (2004)

[45] W.Kozanecki, The PEP-II B-Factory: Status and prospects. *Nucl. Instrum. Meth.* A446:59-64 (2000)

[46] B. Aubert *et al*, The *BABAR* Detector. *Nucl. Instrum. Meth.* A479:1-116 (2002)

[47] A. Snyder, Effect of vertex cuts on CP reach. *SLAC BABAR Note.* 177 (1994)

[48] A. Ceseracciu *et al*, The new *BABAR* data reconstruction system. *arXiv:cs/0306008v3* (2003)

[49] P. Billoir, Track fitting with multiple scattering: A new method. *Nucl. Instrum. Meth.* A225:352 (1984)

[50] F. James and M. Roos, 'Minuit' a system for function minimisation and analysis of the parameter errors and correlations. *Comput. Phys. Commun.* 10:343-367 (1975)

[51] D. Kirkby and W. Verdenke, RooFit Users Manual. *http://roofit.sourceforge.net/docs/index.html*

[52] ROOT, an object orientated data analysis framework. *http://root.cern.ch*

[53] A. Drescher *et al*, The Argus Electron-Photon Calorimeter III. Electron-Hadron Separation. *Nucl. Instrum. Meth.* A237:464 (1985)

[54] C. Amsler *et al*, Particle Data Group. *Phys. Lett.* B667:1 (2008)

[55] W. B. Dunwoodie, Simple observations on $B\overline{B}$ kinematics. *http://www.slac.stanford.edu/ wmd/bbkinematics/kinematics.note.gz*

[56] W. T. Ford, Choice of kinematic variables in B meson reconstruction - take 3. *BABAR Analysis Document # 53*

[57] Chih-hsiang Cheng, Dalitz distribution function for $D^0 \to K\pi\pi^0$. *http://www.slac.stanford.edu/ chcheng/talk/kpipi0DalitzFunc/*

[58] B. Aubert *et al*, Study of $B \to D_{sJ}^{(*)+}\overline{D}^{(*)}$ Decays Particle Data Group. *Phys.Rev. Lett.* 93:181801 (2004)